The Thesis Committee for Jung Kyu Kim
Certifies that this is the approved version of the following thesis:

Multicomponent seismic image matching and comparison - Fasken Ranch, Andrews County, Texas

APPROVED BY
SUPERVISING COMMITTEE:

Supervisor:

Bob Hardage

Kyle Spikes

Sergey Fomel

Multicomponent seismic image matching and comparison - Fasken Ranch, Andrews County, Texas

by

Jung Kyu Kim, B.S.

Thesis

Presented to the Faculty of the Graduate School of

The University of Texas at Austin

in Partial Fulfillment

of the Requirements

for the Degree of

Master of Science in Geological Sciences

The University of Texas at Austin

May 2015

Dedication

I dedicate this to my family, Hye Won Ahn and Jason Kim, my parents, my friends, and the scientific society.

Acknowledgements

First of all, I am greatly indebted to my advisor Dr. Bob A. Hardage for his guidance and support during my graduate studies. When I joined his research group, I had no geophysical background. He answered all my questions, sometimes foolish questions, with patience and it seemed to me that his only purpose is to make me understand geosciences. His dedication to my education and research as his student has made this work possible, and he has guided me along the path with benevolentness like a father. I would like to acknowledge the guidance I received from my committee members: Dr. Kyle Spikes and Dr. Sergey Fomel. They gave great lectures on seismology, rock physics, and mathematical methods in geophysics, and I learned most of my geophysical knowledge from their lectures and their feedback to my questions. As an industry partner, Fasken Oil and Ranch generously provided the 3C3D seismic data and well data. FairfieldNodal processed the digital 3C3D seismic data. Landmark Graphics Corporation provided software for the 3C3D seismic interpretation via the Landmark University Grant Program. Some of the illustrations were prepared by Bureau of Economic Geology - UT at Austin graphics department.

Furthermore, I would like to express my gratitude to Michael V. DeAngelo who has been my mentor since I entered the school. He is the first person I met in this school and, from that day on, he has kindly supported me with his great experience and practical knowledge. I am really thankful for all discussions with him and suggestions that improved my understanding of geophysics. I am also very thankful to fellow students: Menal Gupta, Ahmet Serkan Kabakci, Fatma Kübra Arisoy, and Saygin Ileri in the

Exploration Geophysics Laboratory. It was a really great time to have studied with them at The University of Texas at Austin.

Lastly, I would like to thank VP Ik Hyun Park, Dr. Jonggeun Choe, and Dr. Munseok Baek for their recommendations and invisible support from my home country.

Abstract

Multicomponent seismic image matching and comparison - Fasken Ranch, Andrews County, Texas

Jung Kyu Kim, M.S. Geo. Sci

The University of Texas at Austin, 2015

Supervisor: Bob Hardage

P-wave and S-wave multicomponent seismic data respond to lithology and fluid variations differently, providing interpreters with tools that supply additional information about subsurface geology. To interpret multicomponent data correctly, it is essential to identify and interpret corresponding seismic events in each seismic data set until they are correctly correlated and considered depth-registered. This study will focus on methods for analyzing P-P, SV-P, and P-SV seismic data integrated with well data to develop a better understanding of the subsurface geology within the study area. My work considers if and how multicomponent data can be matched with reflection patterns and when they cannot, how synthetic seismograms can be used to constrain depth-registration, and illustrates applications of 3C3D P-P, SV-P, P-SV seismic data located on the western shelf of the Midland Basin in Andrews County, Texas.

An important point about this study is that it utilizes SV-P data generated by a vertical vibrator source and recorded with vertical geophones. This new concept allows shear wave information to be extracted from seismic surveys that have been recorded

without the use of 3-component geophones or horizontal vibrators. Accordingly, this study will serve as one of the first case studies for determining the validity of these unique converted-mode seismic data.

Table of Contents

List of Tables

List of Figures

Chapter 1: Introduction

1.1 Motivation and Objectives

Oil and gas production has significantly increased over the past decade partly due to advancements in seismic technologies, horizontal drilling, and hydro-fracking. Seismic images are so common in the oil and gas industry that many people working in unrelated positions, like financial departments, frequently encounter seismic data displays even though they do not have a basic background in geosciences. The majority of seismic data are derived from down-going and up-going P-waves (P-P). However, there are additional seismic modes that can be utilized with multicomponent seismic data (Hardage et al., 2011). These additional wave modes can be separated into down-going and up-going S-waves (SV-SV), down-going P-waves and up-going SV-waves (P-SV), and down-going SV-waves and up-going P-waves (SV-P). SV-P imaging technologies from reflection signals acquired using vertical vibrators and vertical geophones are being developed by the Exploration Geophysics Laboratory at The University of Texas at Austin (Hardage et al., 2014). Definitely, P-P images are more common than other multicomponent seismic images because of higher levels of difficulty related to seismic data processing and increased cost of equipment required to acquire multicomponent seismic data in the field. In particular, using horizontal vibrators as direct-S sources and deploying multicomponent (3C) geophones increase data acquisition cost. If multicomponent seismic data can be produced without horizontal vibrators and three-component (3C) geophones, and if the data have proper quality, the use of multicomponent seismic data can be significantly increased. Adding only a small additional amount of expense for SV-

P data processing will make it possible to utilize SV-P images and S-wave attributes recorded by only vertical geophones. The oil and gas industry could witness decades of amazing progress in reservoir characterization and hydrocarbon production by extracting SV-P images from legacy P-P data.

One big challenge of using multicomponent seismic data is depth registration of P and S images. To compare multicomponent seismic images and use them simultaneously, it is essential that all images be matched in depth. There are several commercial software applications that provide modules to generate P-P synthetic seismograms from well logs which can be used for depth registration, However, P-SV synthetic, SV-P, and SV-SV synthetic seismograms can be created in few commercial software applications.

In this thesis, synthetic seismograms of P-P, SV-P, and P-SV reflectivities are created and compared with real seismograms for depth registration purposes. Emphasis is on applying P-P image depth registration methods using well logs to construct SV-P, P-SV, and SV-SV synthetic data. A convolution model is used to create synthetic seismograms and several concepts that are required to apply conventional P-P synthetic seismogram depth registration methods to SV-P, P-SV, and SV-SV synthetic seismogram depth registrations are reviewed and considered theoretically. Also, multicomponent seismic images are compared to show whether SV-P data created by a vertical vibrator source and recorded by a vertical receiver are viable and how these SV-P seismic data can be used with P-P data, not only from a theoretical point of view, but also in application to actual reservoir characterization.

1.2 STRUCTURE OF THIS THESIS

First of all, geologic and stratigraphic backgrounds corresponding to seismic data acquired across the Fasken Ranch in Andrews County, Texas will be presented. Also, a brief description of seismic data used for analysis, including a general description of the new SV-P data-acquisition technique and calibration well data, will be described.

Next, fundamental principles related to reflection coefficient calculation, convolution model concepts, reflection geometries, and wavelet extraction procedures used for conventional P-P image depth registration are discussed and several related theories required to expand this method to SV-P, P-SV, and SV-SV depth registration will be presented. In addition, the concept of the stratalslicing technique, together with seismic attributes which are useful for multicomponent image comparison, will be reviewed. Then, P-P, SV-P, and P-SV images will be matched, and the effect of incident angle and phase spectrum assumptions on depth registration will be considered.

For the purpose of showing the reliability of SV-P imaging and the applicability of multicomponent seismic image matching, P-P, SV-P, and P-SV images are compared in the geologic time domain using stratal slices. RMS amplitude and semblance maps will be shown to support these comparisons.

Finally, similarities and differences of multicomponent seismic images, including how and why multicomponent seismic data are valuable, are discussed.

Chapter 2: Study Area and Data

2.1 GEOLOGY REVIEW

The Fasken seismic survey area is located in Andrews County, Texas (Figure 2.1-1). Hamlin and Baumgardner (2012) analyzed huge amounts from well data of the Midland Basin and constructed detailed geologic information describing Wolfberry unconventional reservoirs. Their well locations and cross sections are shown in Figure 2.1-1, and one of their cross sections (C-C') passes through the Fasken Ranch area. Figure 2.1-2 shows lithofacies distributions along Wolfberry cross section C-C'. According to their well-based study and the location of the Fasken Ranch area, the upper part of the Wolfberry interval is mostly carbonate, calcareous mudrock, and siliciclastic rock. Significant changes in stratigraphy and lithofacies occur beneath the Fasken Ranch area.

Figure 2.1-3 shows key stratigraphic units of the Midland Basin. Characteristics of the upper Leonardian units (Spraberry - Dean) of the Wolfberry are low permeability and deep-water turbidite deposits. Lower Pennsylvanian units are derived from highlands uplifted during the late Paleozoic collision of the ancestral North America plate with South America and Africa (Ball, 1995). The Early Ordovician (Ellenburger) unit of this region was a shallow-water shelf with deep water conditions to the south. Shallow-water carbonates were deposited on the shelf, and deep-water shales and carbonates were deposited on the slope and in the basin (Kerans, 1990). There are three major diagenetic processes in the Ellenburger carbonates: (1) dolomitization, (2) karsting, and (3) tectonic fracturing associated with karsting (Loucks, 2006).

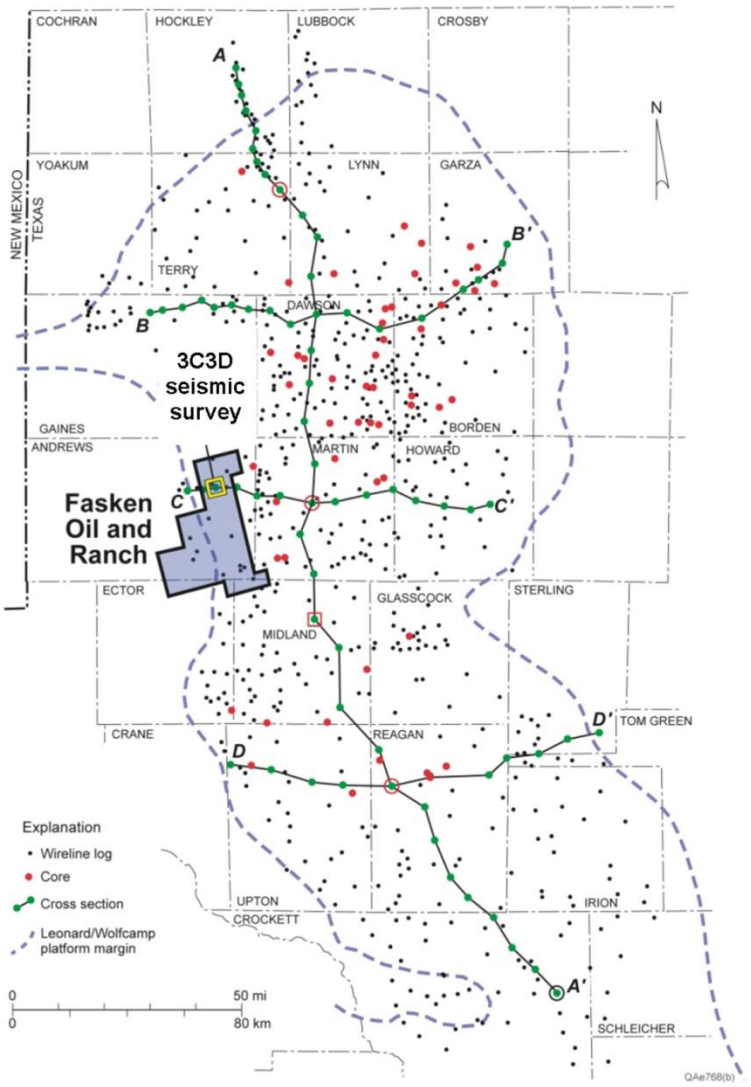

Figure 2.1-1: Well locations and cross sections used by Hamlin and Baumgardner (2012). Cross section CC' passes through the Fasken seismic survey area.

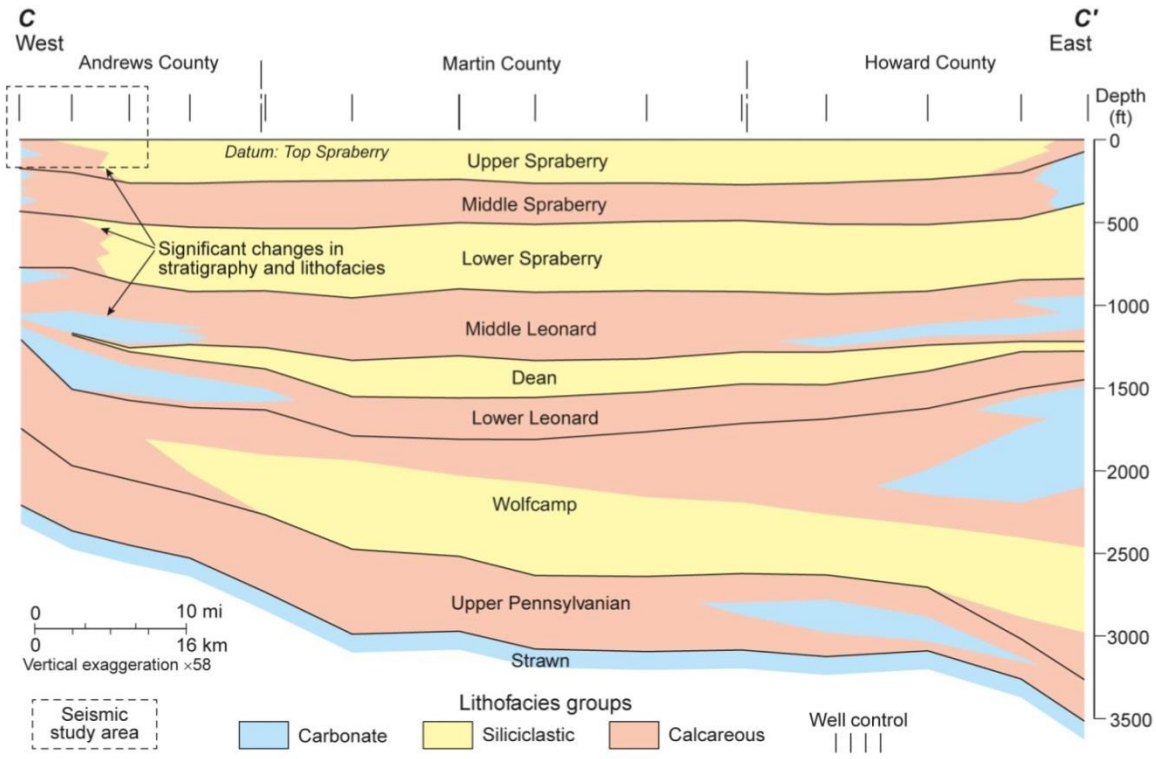

Figure 2.1-2: Cross section CC' of Figure 2.1-1. Fasken 3C3D seismic area is drawn as a dashed box at top of figure. This cross section corresponds to the upper half of Fasken seismic data (Modified from Hamlin and Baumgardner, 2012).

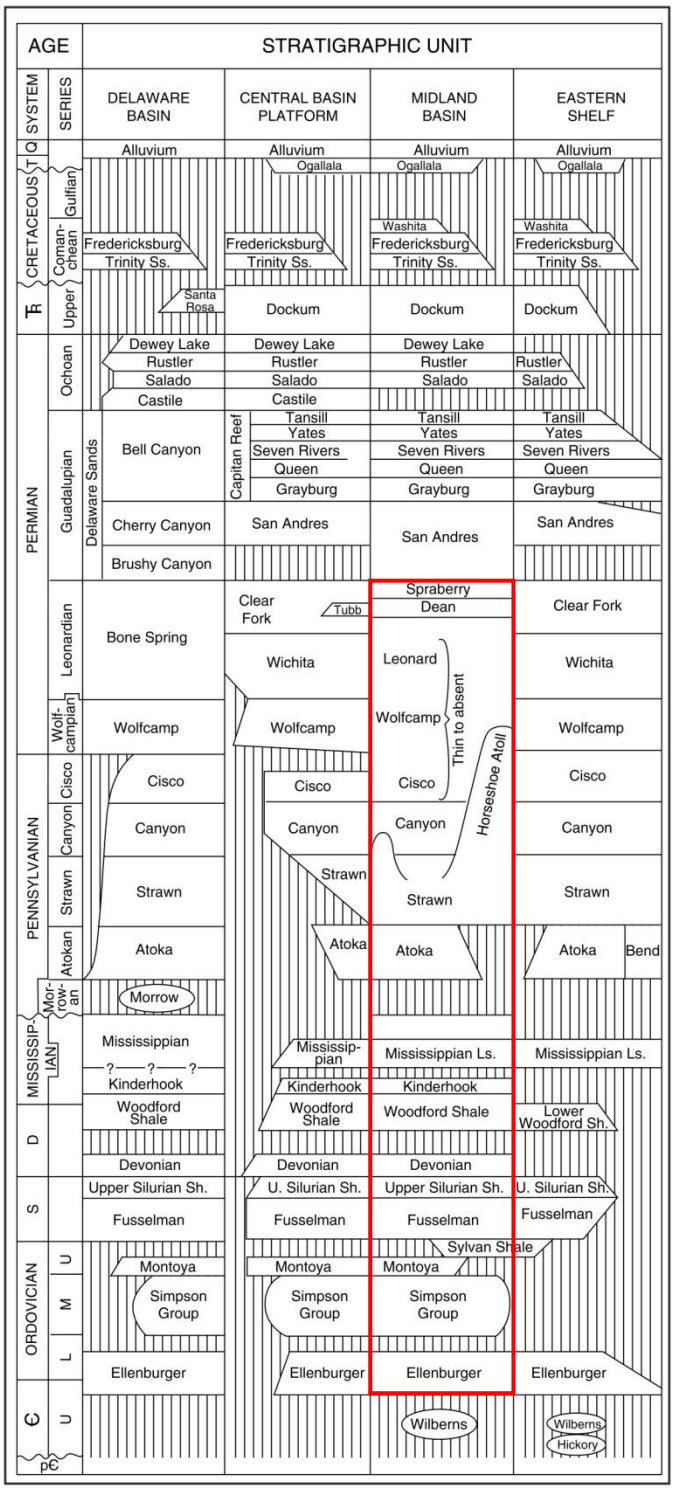

Figure 2.1-3: Stratigraphic column of Permian Basin (Ball, 1995). Area of interest is highlighted with a red box.

2.2 DATA DESCRIPTION

2.2.1 SEISMIC DATA

A 3D multicomponent (3C3D) seismic data survey acquired across the Fasken Ranch was used in this thesis. Three inline vibrators were used at each source station. Each receiver station included a single 3C geophone in addition to a separate 110-ft group array of 12 vertical 1C geophones. This allows subsequent images to be compared from the vertical component of the 3C geophones, all components of the 3C geophones, or by the array of 12 vertical geophones to determine the effects, if any, from the two different sets of receiver hardware. The P-P, SV-P, and P-SV images used in this thesis are, respectively, from an array of 12 vertical geophones, vertical component of 3C geophones, and horizontal components of 3C geophones. Figure 2.2.1-1 and Figure 2.2.1-2 show the stacking fold behavior of the data and the distinction in the distribution of reflection points within stacking bins, respectively. Low-fold data occur at the edges of the seismic acquisition area. Data quality of those areas is poor, and the data should be used with caution at the edges of each image space. The SV-P data used in this investigation are, to our knowledge, the only 3D SV-P data ever constructed, and certainly are the only SV-P data ever constructed from data generated by vertical vibrator sources.

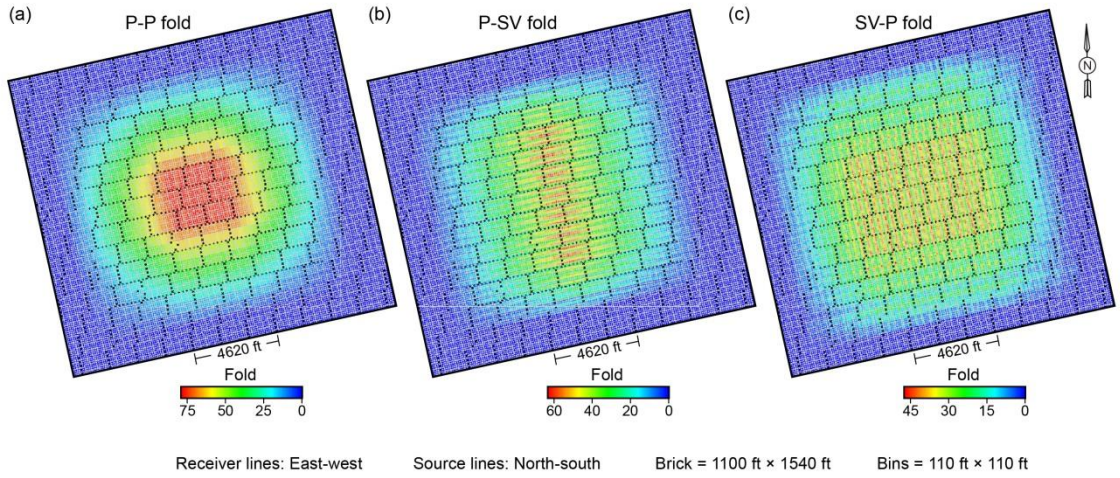

Figure 2.2.1-1: Fold maps associated with (a) P-P image space, (b) P-SV image space, and (c) SV-P image space.

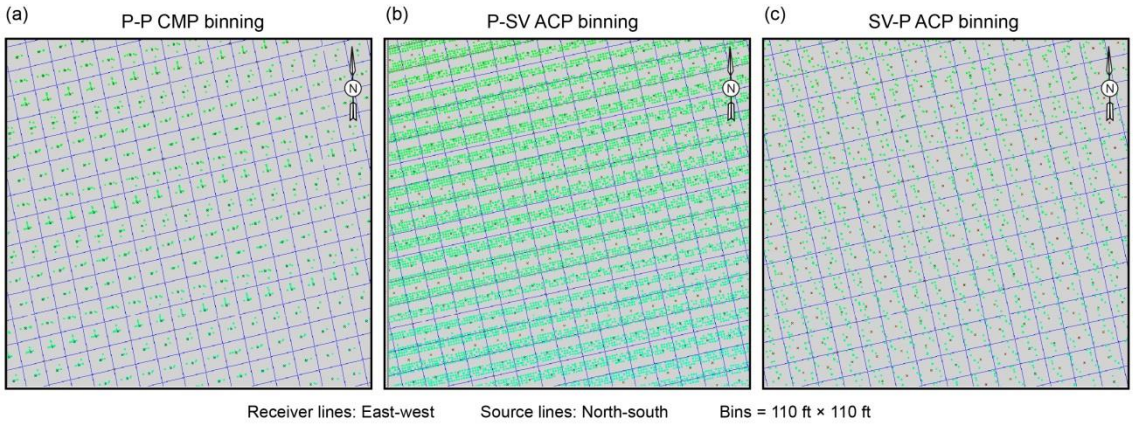

Figure 2.2.1-2: Distribution of reflection points in stacking bins for (a) P-P image , (b) P-SV image , and (c) SV-P image .

2.2.2 WELL DATA

Well data used for this thesis are primarily from well FEE AL 910, which was considered the calibration well due to its substantial digital well-log recording suite. Well AU-1 furnished information for deeper horizons, including the Ellenburger Formation. Locations of these wells are shown in Figure 2.2.2-1. Log data included dipole sonic logs, density logs, and differential caliper log which were vital in creating synthetic seismograms. Stratigraphic top information was provided by the operator of the FEE AL 910 and AU-1 wells. The final drilling depth of the FEE AL 910 well does not reach the Ellenburger unit. The time-to-depth relation of well FEE AL 910 was assumed to be similar to the nearby AU-1 well and was subsequently applied to determine an estimated location within the seismic volumes for the Ellenburger unit. The differential caliper log (DCAL), which defines the distance between the tool sensor and the wall of the borehole, is an indicator of borehole washout conditions and is used to indicate the quality and reliability of the well log data.

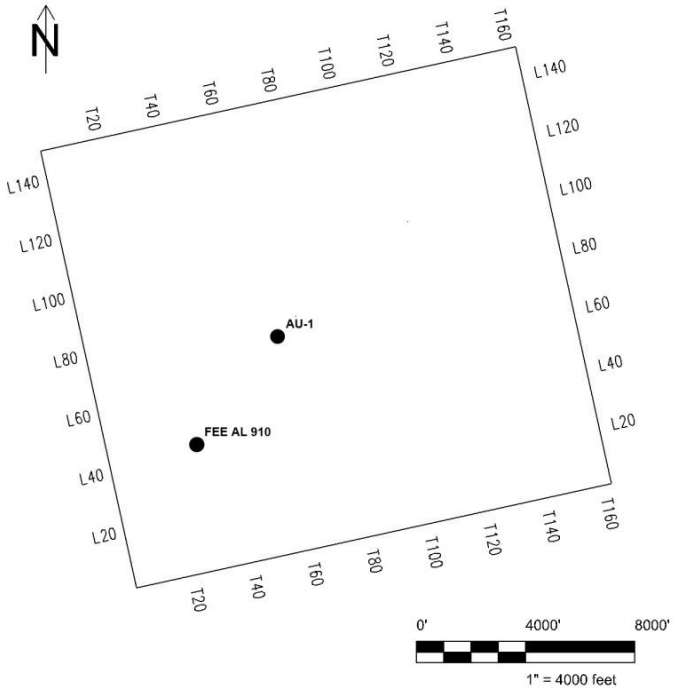

Figure 2.2.2-1: Well locations with seismic survey base map. Vp, Vs, density, and formation tops were used from the FEE AL 910 well. For well AU-1, only formation depth information is available.

Table 2.2.2-1 shows depth information of interpreted stratigraphic well picks provided by the operator. Information from Table 2.2.2-1 is used for seismic-to-well correlation and horizons corresponding to the well picks are selected and checked if they pass the depths of the Yoakum and the Wolfcamp at the location of AU-1 to test the accuracy of horizon picking and decide the two way traveltime of the Ellenburger in multicomponent seismic images.

Formation	Depth (ft)	
	FEE AL 910	AU-1
Yoakum	4,710.00	4,743.78
San Andres	5,721.00	
Basal San Andres	7,242.00	
1st Spraberry	8,415.00	
2nd Spraberry	8,850.00	
Wolfcamp	9,720.00	9,714.87
Basal Wolfcamp	10,461.00	
Strawn	10,861.00	10,901.75
Atoka	11,074.00	11,065.41
Ellenburger		13,940.00

Table 2.2.2-1: Depth measurements of formation tops from FEE AL 910 and AU-1 wells.

Figure 2.2.2-2 shows Vp, Vs, and density information recorded in calibration well FEE AL 910. Measured values are within reasonable ranges; however, some log patterns imply there are intervals within which data quality is not reliable. In the following chapter, the quality of well log data is verified in terms of velocity ratio.

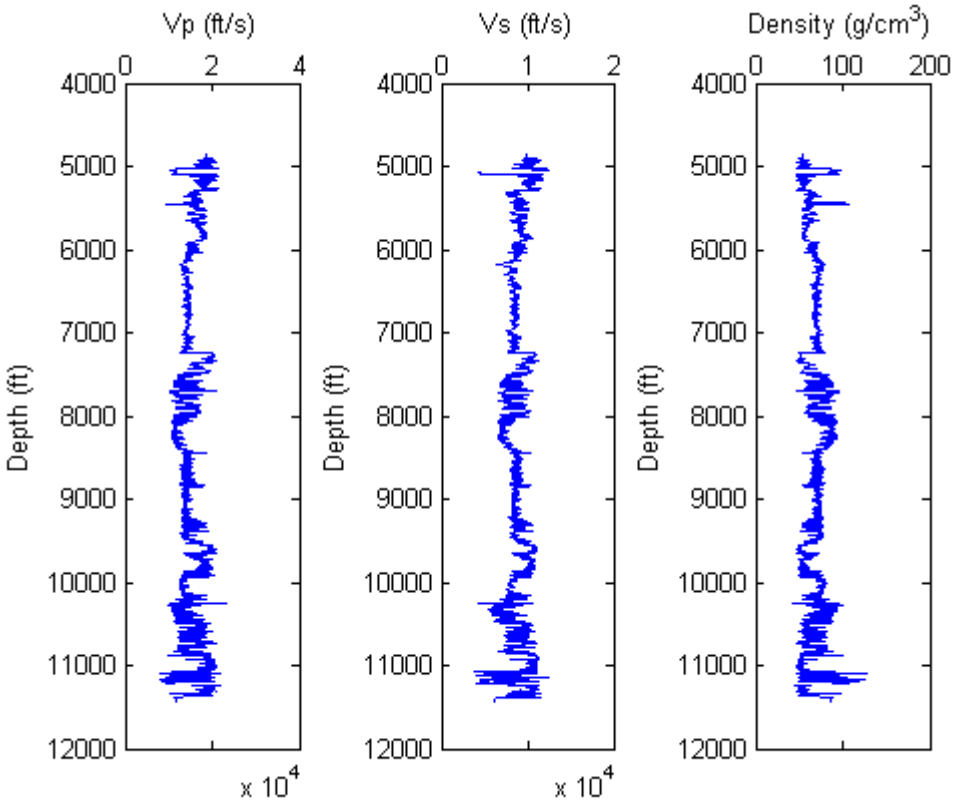

Figure 2.2.2-2: Well log data from well FEE AL 910 in the Fasken seismic area. From the left are P-wave velocity, S-wave velocity, and density versus depth.

Chapter 3: Geophysical Review

3.1 Relationship Among Vp, Vs, and Imaging Time

Seismic imaging time is closely related to the normal moveout (NMO) corrected traveltime that corresponds to traveltime at zero incident angle. Table 3.3-1 shows theoretical traveltimes of down-going and up-going wave at zero incident angle.

Image Type	Downward time	Upward time	Imaging time
P-P image	$\sum_{i=1}^{n} z_i \, \Delta t_{Pi}$	$\sum_{i=1}^{n} z_i \, \Delta t_{Pi}$	$2\sum_{i=1}^{n} z_i \, \Delta t_{Pi}$
P-SV image	$\sum_{i=1}^{n} z_i \, \Delta t_{Pi}$	$\sum_{i=1}^{n} z_i \, \Delta t_{Si}$	$\sum_{i=1}^{n} z_i \, (\Delta t_{Pi} + \Delta t_{Si})$
SV-P image	$\sum_{i=1}^{n} z_i \, \Delta t_{Si}$	$\sum_{i=1}^{n} z_i \, \Delta t_{Pi}$	$\sum_{i=1}^{n} z_i \, (\Delta t_{Pi} + \Delta t_{Si})$
SV-SV image	$\sum_{i=1}^{n} z_i \, \Delta t_{Si}$	$\sum_{i=1}^{n} z_i \, \Delta t_{Si}$	$2\sum_{i=1}^{n} z_i \, \Delta t_{Si}$

Table 3.1-1: Relationship between imaging time and slowness. Z_i is depth of i-th layer, Δt_{pi} is P wave slowness of i-th layer, and Δt_{si} is S wave slowness of i-th layer (Modified from Hardage et al., 2011).

Assuming a constant Vp/Vs velocity ratio within chosen time intervals of a seismogram, a rough relationship among P-P, P-SV, SV-P, and SV-SV image times can be derived (Equations 3.1-a, 3.1-b, and 3.1-c). Once a certain interval is chosen in one image space, matching intervals in other image spaces can be defined using these

equations and reasonable ranges of the Vp/Vs velocity ratio. Table 3.1-2 shows typical velocity ratios of various rock types. Velocity ratio values can also be used to test the accuracy of picked horizons.

$$\frac{S\text{–}S\ image\ time}{P\text{–}P\ image\ time} = \frac{2z\,\Delta t_s}{2z\,\Delta t_p} = \frac{\Delta t_s}{\Delta t_p} = \frac{V_p}{V_s} = R \qquad (3.1\text{-}a)$$

$$\frac{P\text{–}SV/SV\text{–}P\ image\ time}{P\text{–}P\ image\ time} = \frac{z\,(\Delta t_p + \Delta t_s)}{2z\,\Delta t_p} = \frac{1}{2}\left(1 + \frac{\Delta t_s}{\Delta t_p}\right) = \frac{1}{2}(1 + R) \qquad (3.1\text{-}b)$$

$$\frac{P\text{–}SV/SV\text{–}P\ image\ time}{S\text{–}S\ image\ time} = \frac{z\,(\Delta t_p + \Delta t_s)}{2z\,\Delta t_s} = \frac{1}{2}\left(1 + \frac{\Delta t_p}{\Delta t_s}\right) = \frac{1}{2}\left(1 + \frac{1}{R}\right) \qquad (3.1\text{-}c)$$

Rock Type	Velocity Ratio $R = \frac{V_p}{V_s}$
Sandstone	1.59~1.76
Dolomite	1.78~1.84
Limestone	1.84~1.99
Shale	1.70~3.00

Table 3.1-2: Range of velocity ratio (Domenico, 1984)

There are many examples in which relationships between the Vp/Vs velocity ratio and multicomponent seismic image matching are shown. From velocity ratio and matching horizons, Tatham et al. (1991) estimated producing layer thickness and Pardus et al. (1990) predicted lithology and velocity changes for small time intervals. Also, Fomel et al. (2003) and Fomel et al. (2005) pointed out that velocity ratios can be

estimated with high resolution with an automatic data registration algorithm applied to P-P and P-SV image.

Velocity ratios can be used to check the quality of well log data. If sonic log measurements are reasonable, the velocity ratio should be within ranges shown in Table 3.1-2. In the cross-plot of Vp versus Vs (Figure 3.1-1) from the well FEE AL 910, there are three linear trends between Vp and Vs. Two of these trends (① and ③) are not reliable considering the velocity ratio. Velocity ratio measurements are plotted against depth with the differential caliper log values in Figure 3.1-2. This cross plot behavior shows incorrect Vp/Vs values are associated with borehole washouts. For the Fasken seismic area, the velocity ratio is mostly between 1.5 and 2. In some deeper intervals, velocity ratios larger than 2 can be possible.

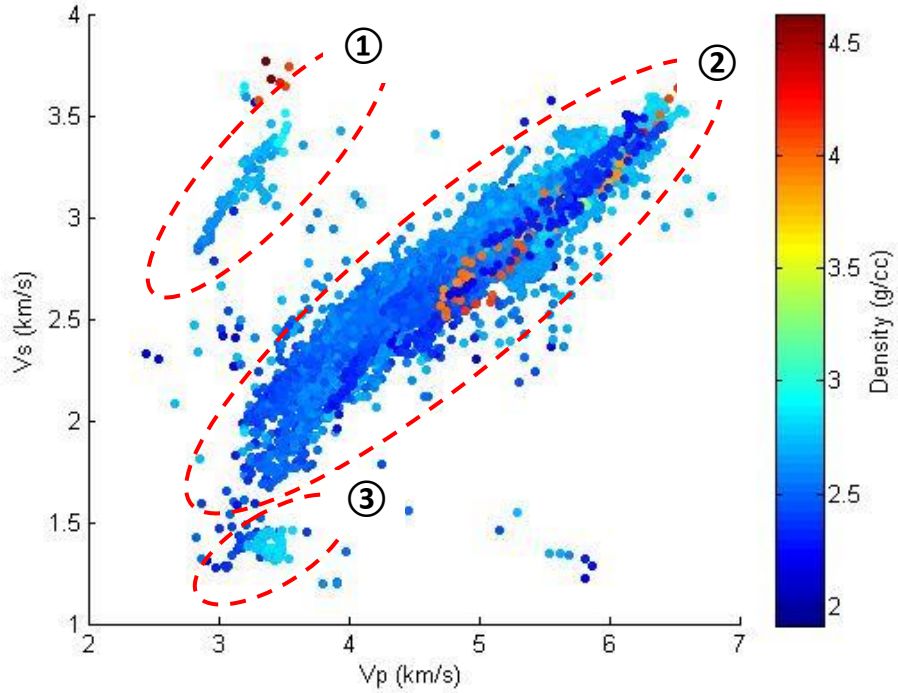

Figure 3.1-1: Vs versus Vp plot from calibration well FEE AL 910. Three distinct patterns exist across the Wolfberry section.

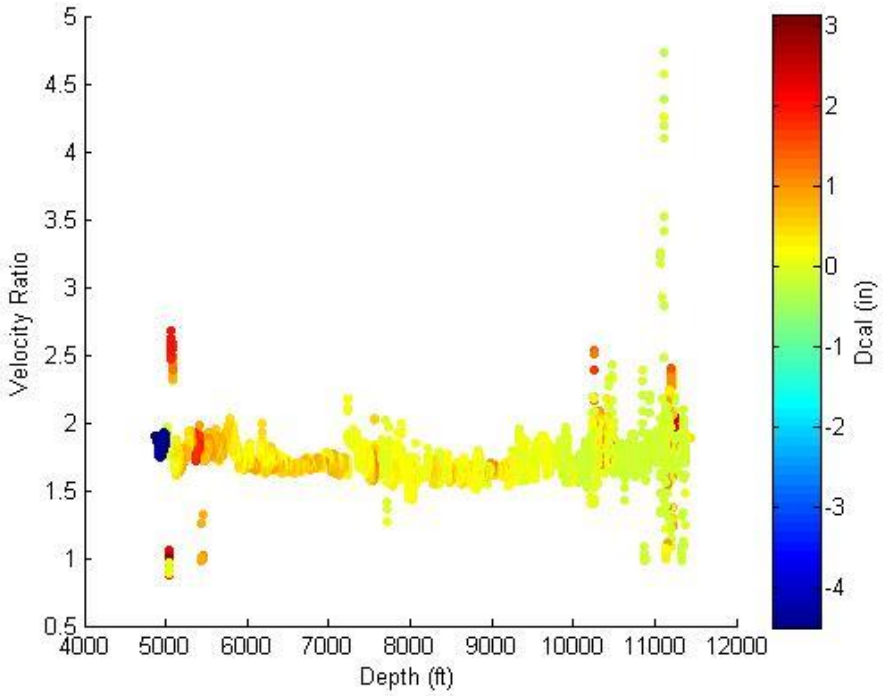

Figure 3.1-2: Velocity ratio versus depth plot at calibration well FEE AL 910. Dcal stands for differential caliper log measurements. Data that have velocity ratio smaller than 1.59 or larger than 3 are caused by bad data quality, such as a borehole washout or temporary malfunction of logging tools.

3.2 SEISMIC WAVE REFLECTION GEOMETRY

Seismic wave reflection geometries for plane waves in homogeneous media at a plane boundary are shown from Figure 3.2-1 to Figure 3.2-5. From Snell's law (Equation 3.2-a), reflection angles are calculated and denoted in these figures.

$$p = \frac{\sin i_1}{\alpha_1} = \frac{\sin j_1}{\beta_1} \qquad (3.2\text{-}a)$$

where, i_1 is the P-wave angle in media 1, j_1 is the S-wave angle in media 1, α_1 is the P-wave velocity in media 1, and β_1 is the S-wave velocity in media 1.

When a down-going P-wave is reflected at a boundary, the P-wave reflection angle is the same as the incident P-wave angle, and the reflection point is defined as a common midpoint (CMP). In this ideal case, seismic wave reflection geometry is symmetric in the vertical plane that passes through the CMP as shown in Figure 3.2-1. For a down-going S-wave and an up-going S-wave, the reflection geometry is the same as that for down-going P-waves and up-going P-waves (Figure 3.2-2).

Down-going S-waves and up-going P-waves, and also down-going P-waves and up-going S-waves, have a different reflection-geometry as shown Figure 3.2-3 and Figure 3.2-5. P-SV and SV-P reflection points are not at the CMP but at common conversion points (CCP). When the source and receiver location are fixed, the P-SV reflection point is at CCP_A and the SV-P reflection point is at CCP_B shown in Figure 3.2-3. Hardage et al. (2011) pointed out that reflection coefficients for the P-SV mode and SV-P mode are almost identical when the distance from source to receiver is the same. This physics is expressed by the reflectivity relationship in Equation 3.2-b taken from Aki and Richards (1990).

$$\grave{S}\acute{P} = \frac{\cos j}{\alpha}\frac{\beta}{\cos i}\,\grave{P}\acute{S} \qquad \textit{(3.2-b)}$$

in this equation, i is the P-wave angle, j is the S-wave angle, α is the P-wave velocity, and β is the S-wave velocity. $\grave{S}\acute{P}$ and $\grave{P}\acute{S}$ are reflection coefficients for SV-P and P-SV modes.

This geometry corresponds to the situation shown in Figure 3.2-4 where the source and receiver locations are shifted so that reflection points CCP_A and CCP_B of Figure 3.2-3 are located at the same coordinate.

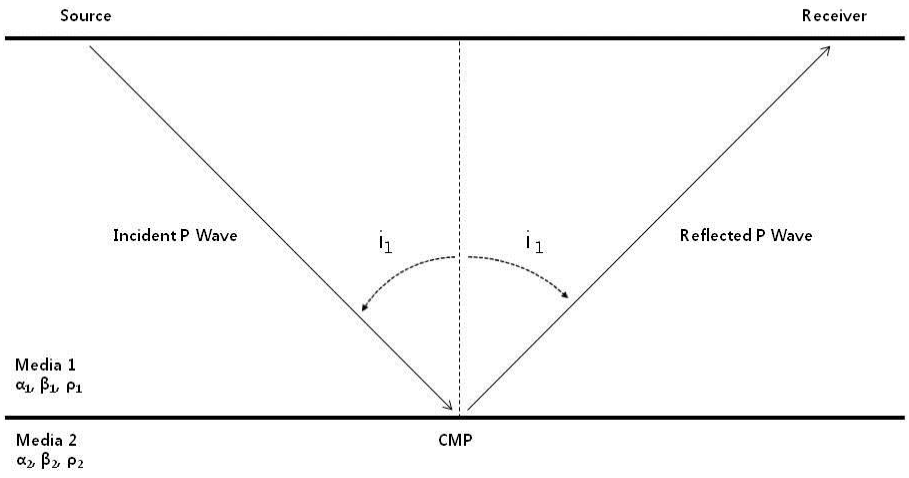

Figure 3.2-1: P-P reflection geometry. i_1 is P wave angle in media 1.

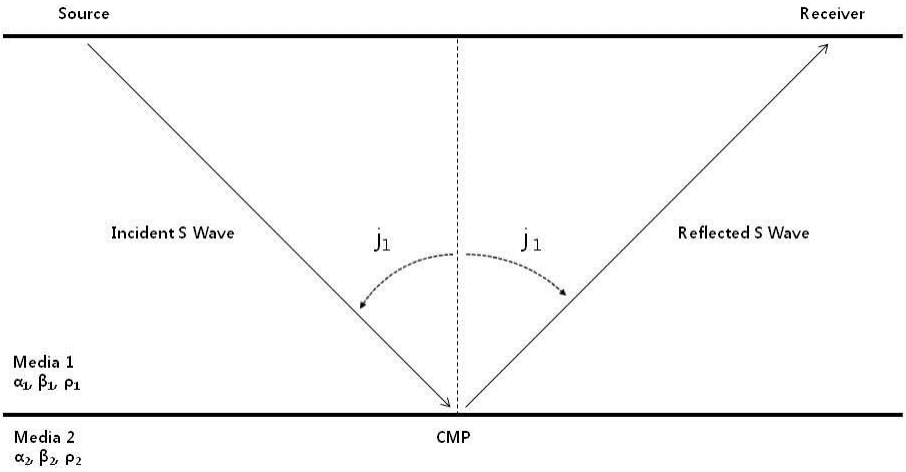

Figure 3.2-2: SV-SV reflection geometry. j_1 is S-wave angle in media 1.

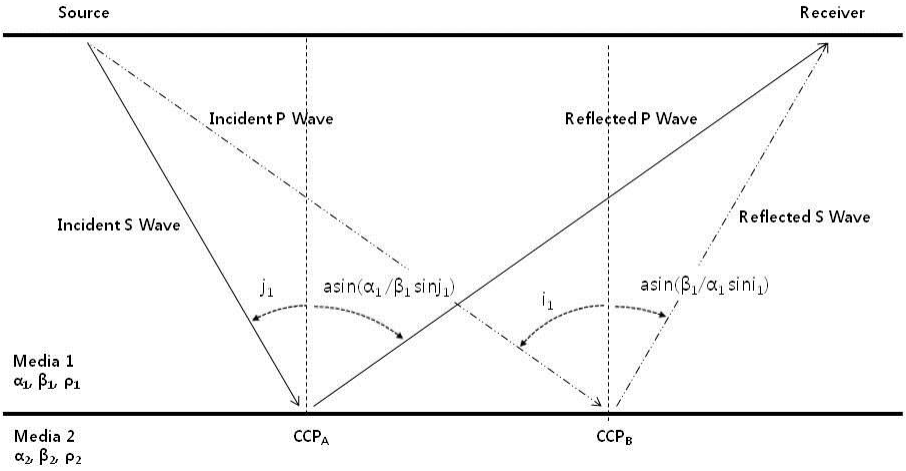

Figure 3.2-3: SV-P/P-SV reflection geometry with same source and receiver locations. i_1 and j_1 are incident P-wave and incident S-wave angle in media 1.

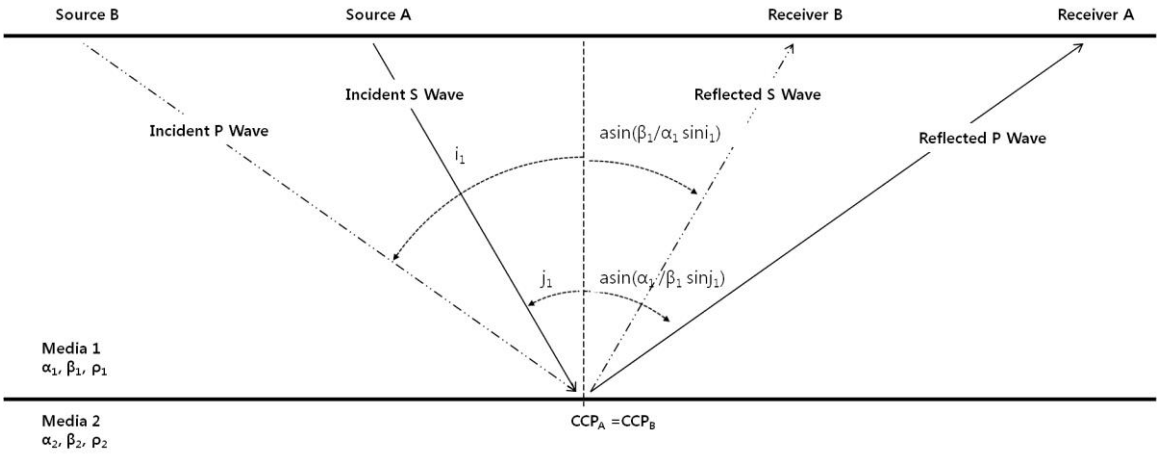

Figure 3.2-4: SV-P/P-SV reflection geometry with the same offset and CCP. i_1 and j_1 are incident P-wave and incident S-wave angle in media 1.

The reflection geometry when the incident angles of P-SV and SV-P modes are the same is shown in Figure 3.2-5. By Snell's Law, the receiver locations of both modes are not same, but P-SV reflectivity and SV-P reflectivity are mathematically the same for this geometry. This mathematical equality demonstrates equivalence of P-SV and SV-P images and shows how P-SV depth registration methods can be applied to SV-P depth registration. The equality of P-SV mode and SV-P mode reflectivities will be shown numerically in the following chapter.

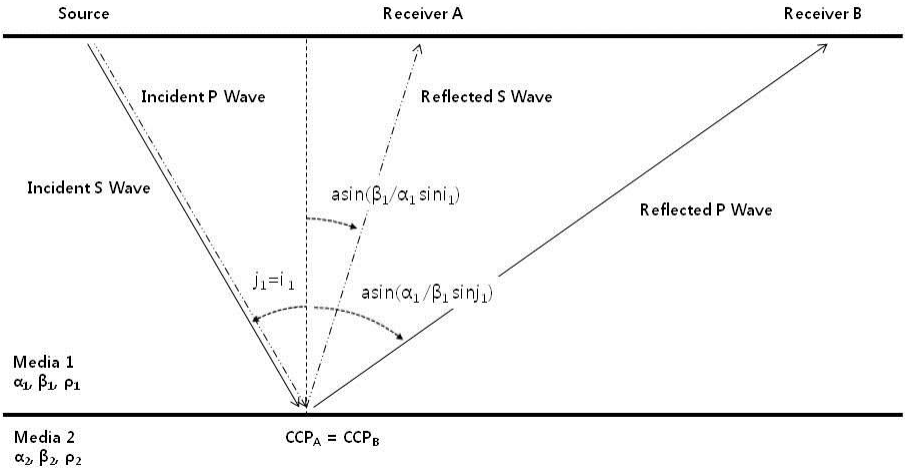

Figure 3.2-5: SV-P/P-SV reflection geometry with the same CCP. i_1 and j_1 are incident P-wave and incident S-wave angle in media 1.

3.3 REFLECTION COEFFICIENTS CALCULATION: ZOEPPRITZ EQUATION

For a specific incidence angle, reflection, conversion, and transmission coefficients can be calculated from the Zoeppritz equation. Equation 3.3-a is a simplified matrix form of the Zoeppritz equation (Aki and Richards, 2002).

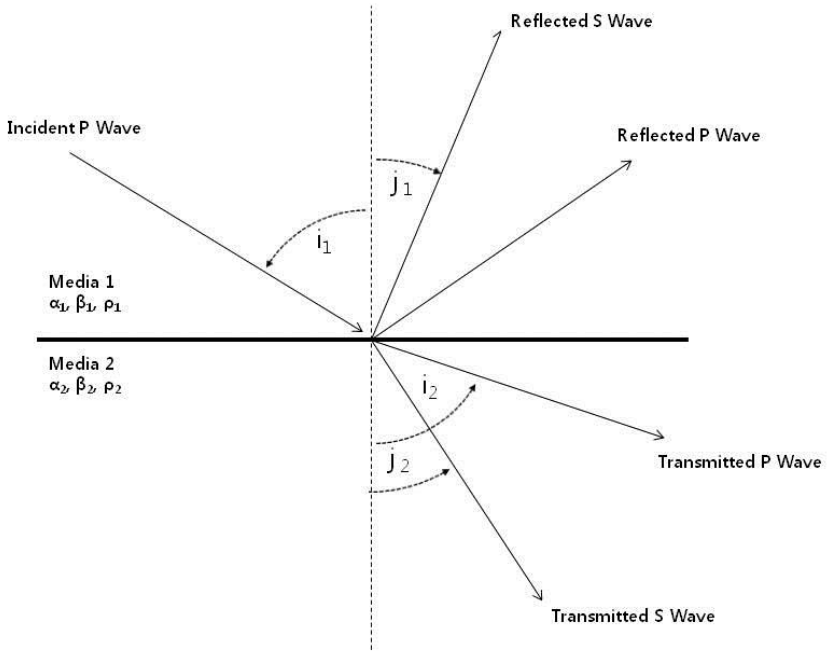

Figure 3.3-1: Reflection and transmission of incident P-wave at an interface. i_1 is the incident P-wave angle, i_2 is the transmitted P-wave angle, j_1 is the reflected S-wave angle, and j_2 is the transmitted P-wave angle.

$$\boldsymbol{Q} = \begin{pmatrix} \grave{P}\acute{P} & \grave{S}\acute{P} & \acute{P}\acute{P} & \acute{S}\acute{P} \\ \grave{P}\acute{S} & \grave{S}\acute{S} & \acute{P}\acute{S} & \acute{S}\acute{S} \\ \grave{P}\grave{P} & \grave{S}\grave{P} & \acute{P}\grave{P} & \acute{S}\grave{P} \\ \grave{P}\grave{S} & \grave{S}\grave{S} & \acute{P}\grave{S} & \acute{S}\grave{S} \end{pmatrix} = \boldsymbol{P^{-1}R} \qquad \textit{(3.3-a)}$$

In this equation, the first letter indicates the type of incident wave, and the second letter represents the type of derived wave. The acute accent (´) indicates an up-going wave while a down-going wave has a grave accent (`). The P and R matrices are defined as;

$$\boldsymbol{P} = \begin{pmatrix} -\alpha_1 p & -\cos j_1 & \alpha_2 p & \cos j_2 \\ \cos i_1 & -\beta_1 p & \cos i_2 & -\beta_2 p \\ 2\rho_1\beta_1^2 p \cos i_1 & \rho_1\beta_1(1-2\beta_1^2 p^2) & 2\rho_2\beta_2^2 p \cos i_2 & \rho_2\beta_2(1-2\beta_2^2 p^2) \\ -\rho_1\alpha_1(1-2\beta_1^2 p^2) & 2\rho_1\beta_1^2 p \cos j_1 & \rho_2\alpha_2(1-2\beta_2^2 p^2) & -2\rho_2\beta_2^2 p \cos j_2 \end{pmatrix} \qquad \textit{(3.3-b)}$$

and

$$\boldsymbol{R} = \begin{pmatrix} \alpha_1 p & \cos j_1 & -\alpha_2 p & -\cos j_2 \\ \cos i_1 & -\beta_1 p & \cos i_2 & -\beta_2 p \\ 2\rho_1\beta_1^2 p \cos i_1 & \rho_1\beta_1(1-2\beta_1^2 p^2) & 2\rho_2\beta_2^2 p \cos i_2 & \rho_2\beta_2(1-2\beta_2^2 p^2) \\ \rho_1\alpha_1(1-2\beta_1^2 p^2) & -2\rho_1\beta_1^2 p \cos j_1 & -\rho_2\alpha_2(1-2\beta_2^2 p^2) & 2\rho_2\beta_2^2 p \cos j_2 \end{pmatrix} \qquad \textit{(3.3-c)}$$

where, ρ_1 and ρ_2 are the densities of media 1 and 2, α_1 and α_2 are P-wave velocities of media 1 and 2, β_1 and β_2 are S-wave velocities of media 1 and 2, and p is the ray parameter.

For the special case that the incident angle is zero, by replacing ray parameter p and all the angles with zero, Equation 3.3-a is simplified to Equation 3.3-d. all the terms of Equation 3.3-a that are related to mode conversion become zero in Equation 3.3-d. In other words, there is no mode conversion when a wave is reflected or transmitted at zero incident angle. Thus, the conventional P-P depth registration method in which zero incident angle is assumed is not applicable for depth registration of P-SV and SV-P images. When P-wave velocities of $\grave{P}\acute{P}$ term in Equation 3.3-d are replaced with S-wave

velocities, it is identical to $\grave{S}\acute{S}$ term of Equation 3.3-d with opposite algebraic sign. This similarity between $\grave{P}\acute{P}$ and $\grave{S}\acute{S}$ reflectivity for zero incident angle provides clue about how S-S synthetic seismograms can be created using the same method with which P-P synthetic seismograms are created.

$$\boldsymbol{Q}=\begin{pmatrix}\grave{P}\acute{P} & \grave{S}\acute{P} & \acute{P}\acute{P} & \acute{S}\acute{P}\\ \grave{P}\acute{S} & \grave{S}\acute{S} & \acute{P}\acute{S} & \acute{S}\acute{S}\\ \grave{P}\grave{P} & \grave{S}\grave{P} & \acute{P}\grave{P} & \acute{S}\grave{P}\\ \grave{P}\grave{S} & \grave{S}\grave{S} & \acute{P}\grave{S} & \acute{S}\grave{S}\end{pmatrix}=\begin{pmatrix}\frac{\alpha_2\rho_2-\alpha_1\rho_1}{\alpha_2\rho_2+\alpha_1\rho_1} & 0 & \frac{2\alpha_2\rho_2}{\alpha_2\rho_2+\alpha_1\rho_1} & 0\\ 0 & -\frac{\beta_2\rho_2-\beta_1\rho_1}{\beta_2\rho_2+\beta_1\rho_1} & 0 & \frac{2\beta_2\rho_2}{\beta_2\rho_2+\beta_1\rho_1}\\ \frac{2\alpha_1\rho_1}{\alpha_2\rho_2+\alpha_1\rho_1} & 0 & -\frac{\alpha_2\rho_2-\alpha_1\rho_1}{\alpha_2\rho_2+\alpha_1\rho_1} & 0\\ 0 & \frac{2\beta_1\rho_1}{\beta_2\rho_2+\beta_1\rho_1} & 0 & \frac{\beta_2\rho_2-\beta_1\rho_1}{\beta_2\rho_2+\beta_1\rho_1}\end{pmatrix} \quad \textit{(3.3-d)}$$

where, ρ_1 and ρ_2 are the densities of media 1 and 2, α_1 and α_2 are P-wave velocities of media 1 and 2, β_1 and β_2 are S-wave velocities of media 1 and 2.

One common misuse of Equation 3.3-a is that the second, third, and fourth columns calculated for incident P-wave angles in media 1 are directly used respectively, for incident S-waves in media 1, incident P-waves in media 2, and incident S-waves in media 2. Because ray parameter values calculated for incident P-wave angles in media 1 are not applicable for other cases, ray parameters should be separately calculated for each case. Otherwise, incorrect results will be obtained. Figure 3.3-2 through Figure 3.3-5 show each component of the scatter matrix Q of Equation 3.3-a calculated for model parameters of class-1 gas sand shown in Table 3.3-1. As shown in Figure 3.3-2 through Figure 3.3-5, there are significant differences in the values produced for an incident P-wave in media 1 and the other cases.

Rock Property	Rock Model	
	Media 1 (Shale)	Media 2 (Sand)
Vp (km/s)	3.30	4.20
Vs (km/s)	1.70	2.70
Density (g/cm^3)	2.35	2.49
Poisson's ratio	0.319	0.148

Table 3.3-1: Model parameters for Class 1 gas sand (Rüger, 2002).

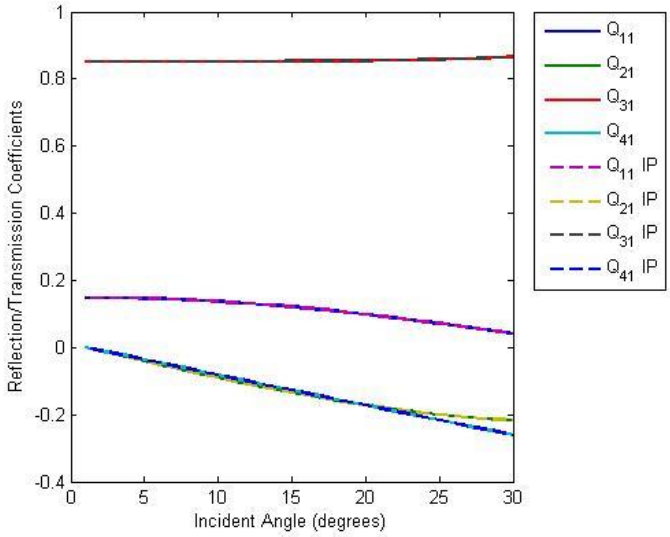

Figure 3.3-2: First column of scatter matrix Q (Equation 3.3-a) for incident P-wave in media 1. Q_{mn} is a component corresponding to the m-th row and n-th column of Q, and IP stands for incident P-wave.

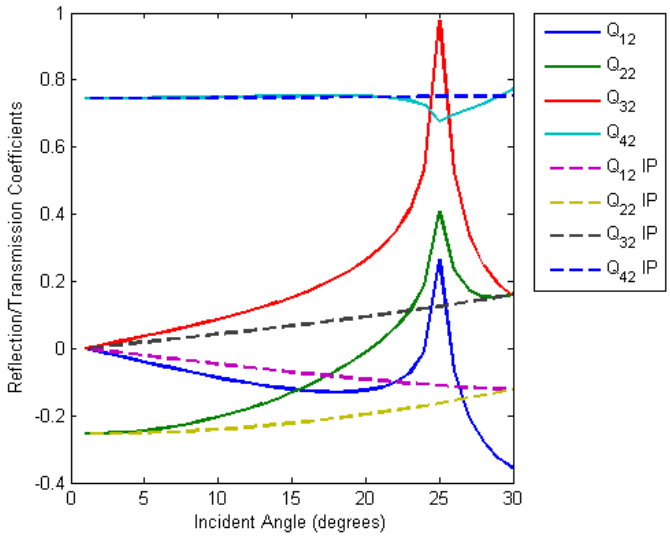

Figure 3.3-3: Comparison of second column of scatter matrix Q (Equation 3.3-a) between incident P-wave in media 1 and incident S-wave in media 1. Q_{mn} is a component corresponding to the m-th row and n-th column of Q, and IP stands for incident P-wave.

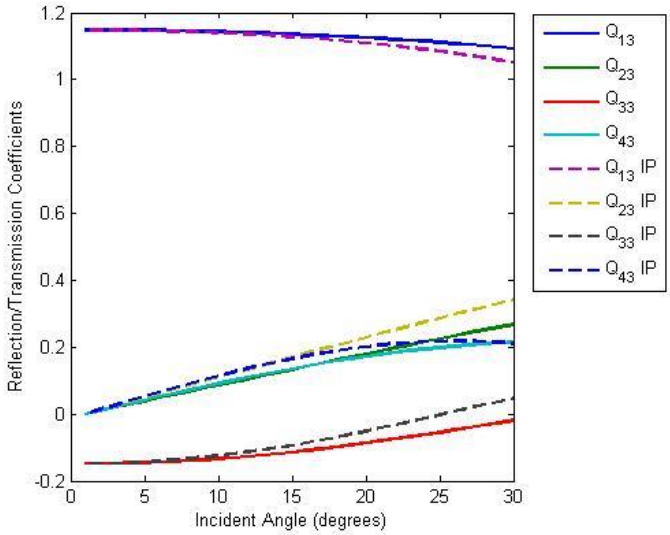

Figure 3.3-4: Comparison of third column of scatter matrix Q (Equation 3.3-a) between incident P-wave in media 1 and incident P-wave in media 2. Q_{mn} is a component corresponding to the m-th row and n-th column of Q, and IP stands for incident P-wave.

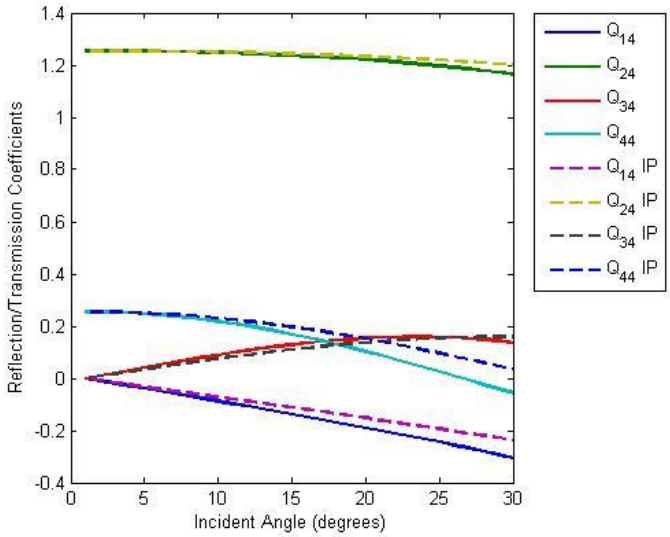

Figure 3.3-5: Comparison of fourth column of scatter matrix Q (Equation 3.3-a) between incident P-wave in media 1 and incident S-wave in media 1. Q_{mn} is a component corresponding to the m-th row and n-th column of Q and IP stands for incident P-wave.

3.4 WAVELET EXTRACTION

Making simplifying assumptions, a seismic trace can be simulated as a convolution of a wavelet with a reflection coefficient series. The Fourier Transform of the time domain Equation 3.4-a becomes Equation 3.4-b in the frequency domain that can be decomposed into an amplitude spectrum and a phase spectrum as shown in Equation 3.4-c. Convolution in time domain corresponds to multiplication in frequency domain.

$$\boldsymbol{s_i(t) = w(t) * r_i(t)} \qquad \textit{(3.4-a)}$$

where, $s_i(t)$ is the i-th seismic trace, $w(t)$ is a wavelet, $r_i(t)$ is the i-th reflection coefficients and $*$ is the convolution operator.

$$\boldsymbol{S_i(\omega) = W(\omega) \times R_i(\omega)} \qquad \textit{(3.4-b)}$$

$$\boldsymbol{|S_i(\omega)| \cdot exp\{j\left(\Phi_{S_i}(\omega)\right)\} = |W(\omega)| \cdot |R_i(\omega)| \cdot exp\{j\left(\Phi_w(\omega) + \Phi_{r_i}(\omega)\right)\}} \qquad \textit{(3.4-c)}$$

In these two equations, $|S_i(\omega)|$ is the amplitude spectrum of the i-th seismic trace, $\Phi_{S_i}(\omega)$ is the phase spectrum of the i-th seismic trace, $|W(\omega)|$ is the amplitude spectrum of a wavelet, $|R_i(\omega)|$ is the amplitude spectrum of the i-th reflectivity coefficient series, $\Phi_w(\omega)$ is the phase spectrum of a wavelet, and $\Phi_{r_i}(\omega)$ is the phase spectrum of the i-th reflectivity coefficient series.

Conversely, if both the amplitude spectrum and phase spectrum of a wavelet are known, the wavelet can be inverted into the time domain using the Inverse Fourier Transform. Wavelet extraction from seismic traces thus consists of amplitude spectrum estimation and phase spectrum estimation.

3.4.1 AMPLITUDE SPECTRA

The amplitude spectrum of a propagating wavelet can be computed from the autocorrelation of a trace by assuming that the reflection coefficients of a trace are a random series (Stone, 1984) or by using the arithmetic average of amplitude spectra of many traces (Angeleri, 1983). The autocorrelation of the i-th seismic trace is given by Equation 3.4.1-a. If $r_i(t)$ is random, $r_i(t) \otimes r_i(t)$ is a spike, and the amplitude spectrum of the wavelet can be computed from the square root of the autocorrelation of the trace.

$$\boldsymbol{s_i(t) \otimes s_i(t) = \{r_i(t) \otimes r_i(t)\} \times \{w(t) \otimes w(t)\}} \qquad \textit{(3.4.1-a)}$$

In this relationship, $s_i(t)$ is i-th seismic trace, $r_i(t)$ is the i-th reflection coefficient series, w(t) is the wavelet, and $\otimes$ is the correlation operator.

Also, from Equation 3.4-c in the preceding section, $|S_i(\omega)| = |W(\omega)| \cdot |R_i(\omega)|$ and the arithmetic average of amplitude spectrum of N traces is Equation 3.4-b. Because $|R_i(\omega)|$ is random, $\frac{1}{N}\sum_{i=1}^{N}|R_i(\omega)|$ should be the same value for any arbitrary collection of many traces, and the amplitude spectrum of the wavelet can be computed from an arithmetic average of a large number of traces.

$$\boldsymbol{\frac{1}{N}\sum_{i=1}^{N}|S_i(\omega)| = |W(\omega)| \cdot \{\frac{1}{N}\sum_{i=1}^{N}|R_i(\omega)|\}} \qquad \textit{(3.4.1-b)}$$

In this equation, $|W(\omega)|$ is the amplitude spectrum of a wavelet, $|R_i(\omega)|$ is the amplitude spectrum of the i-th reflectivity coefficient series, and $|S_i(\omega)|$ is the amplitude spectrum of the i-th seismic trace.

Figure 3.4.1-1 shows that amplitude spectra of a wavelet can be estimated by averaging several tens of traces. Here, 1000 synthetic seismic traces are generated by convolving a stationary wavelet with random reflection coefficient series. The amplitude spectrum of each trace was then inverted using the Inverse Fourier Transform.

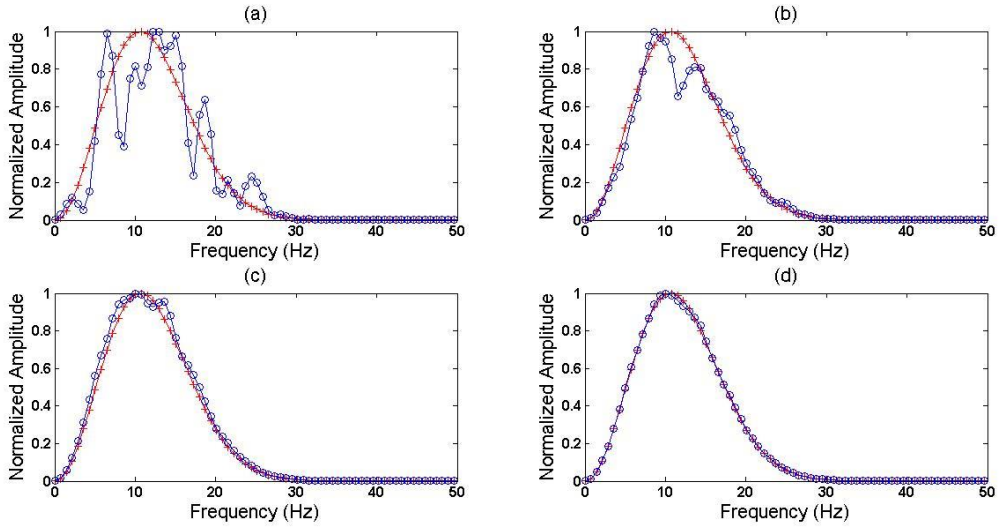

Figure 3.4.1-1: Red-cross curves are normalized amplitude spectra of assumed wavelet. Blue-circle curves are cross plots of normalized amplitude versus frequency estimated from the average of (a) one trace, (b) 10 traces, (c) 100 traces, and (d) 1000 traces.

3.4.2 PHASE SPECTRA

Comparing phase terms of Equation 3.4-c for N traces, the relationship between the phase spectrum of a wavelet and that of seismic traces is given in Equation 3.4.2-a. Assuming $\Phi_{r_i}(\omega)$ is random, $\frac{1}{N}\sum_{i=1}^{N}\Phi_{r_i}(\omega)$ converges to zero with increasing N. Although it seems that the phase spectrum of a wavelet can be estimated averaging phase spectra of sufficiently many traces, the wrapping characteristic of phase makes this estimation impossible without prior information.

$$\frac{1}{N}\sum_{i=1}^{N}\boldsymbol{\Phi}_{s_i}(\boldsymbol{\omega}) = \boldsymbol{\Phi}_{w}(\boldsymbol{\omega}) + \frac{1}{N}\sum_{i=1}^{N}\boldsymbol{\Phi}_{r_i}(\boldsymbol{\omega}) \qquad \textit{(3.4.2-a)}$$

Here, $\Phi_{r_i}(\omega)$ is the phase spectrum of the i-th seismic trace, $\Phi_w(\omega)$ is the phase spectrum of a wavelet, and $\Phi_{r_i}(\omega)$ is the phase spectrum of the i-th reflectivity coefficient series.

Figure 3.4.2-1 shows that solutions that satisfy Equation 3.4.2-a are not unique. To construct this figure, 1000 synthetic traces were generated from convolution of random reflection coefficient series and an assumed wavelet. Then, the phase spectrum of each trace was inverted using the Inverse Fourier Transform. Because of the wrapping of phase, $\Phi_{r_i}(\omega)$ varies by -2π, 0, or 2π with changing $\Phi_w(\omega)$. Generally, there are many $\Phi_w(\omega)$ values that satisfy the condition $\frac{1}{N}\sum_{i=1}^{N}\Phi_{r_i}(\omega) = 0$.

.

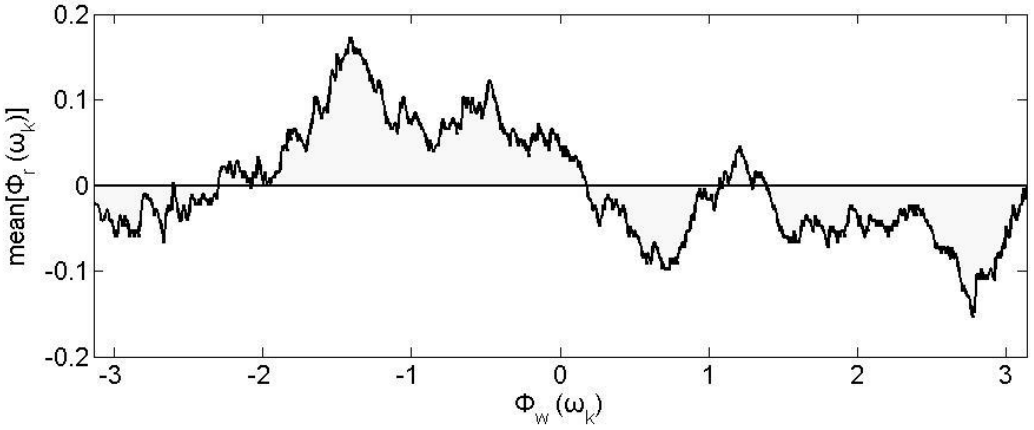

Figure 3.4.2-1: Cross plots of $\frac{1}{N}\sum_{i=1}^{N}\Phi_{r_i}(\omega)$ versus $\Phi_w(\omega)$ for an arbitrary frequency ω_k. There are many $\Phi_w(\omega)$ values, for this frequency, $\frac{1}{N}\sum_{i=1}^{N}\Phi_{r_i}(\omega)$ becomes zero.

Various methods have been proposed to avoid this non-uniqueness such as assuming a minimum phase wavelet, a zero phase wavelet or different distributions of phase. In some specific cases where such assumptions are valid, these methods might give good results; however, there is no generally acceptable method to extract a phase spectrum from seismic traces. For the purpose of wavelet extraction to correlate a seismic trace to a well, zero-phase wavelet or minimum-phase wavelet assumptions are widely used. The phase spectrum can be calculated from the Hilbert transform of the natural logarithm of the amplitude spectrum under minimum phase wavelet assumption (Robinson, 1967), and from Equation 3.4.2-b, the phase spectrum can be deduced from the amplitude spectrum (Dey, 1999).

$$\Phi_w(\omega) = -\frac{2}{\pi}\sum_{t=1}^{t=\infty} sin(\omega t)\int_0^{\pi} cos(\omega t)\, log_e(|W(\omega)|)\, d\omega \qquad (3.4.2\text{-}b)$$

In this equation, $\Phi_w(\omega)$ is the phase spectrum of a wavelet, and $|W(\omega)|$ is the amplitude spectrum of that wavelet.

3.5 THE CONVOLUTION MODEL

The convolution model is useful for imaging the earth when several assumptions are valid (Dey, 1999): (1) The earth consists of flat horizontally layers that have constant velocities. (2) The raypath of the wave is perpendicular to these horizontal layers. (3) The source wavelet does not change as it travels through the earth layering. In such conditions, the reflectivity of the earth, wavelet, and seismic trace are related by convolution (Equation 3.5-a).

$$\boldsymbol{s(t) = w(t) * r(t) + n(t)} \qquad \textit{(3.5-a)}$$

where, s(t) is the seismic trace, w(t) is the wavelet, r(t) is reflectivity, n(t) is noise and $*$ is the convolution operator.

In structurally complex areas, or if there are large lateral facies changes, the earth layers are not flat and horizontal, constant layer velocities do not exist, and the convolution model might be invalid. In my study area, the Fasken Ranch, all horizons are relatively flat and horizontal so that it is very difficult to find any characteristics to distinguish one layer from another. Also, there are no complex structures like faults. In this thesis, flat and horizontal layers with nearly constant velocities can be assumed as the base model for the study area.

Theoretically, from the Zoeppritz equations, there is no mode conversion when the incidence angle is zero. Thus, to deal with multicomponent seismic data and to correlate mode-converted data to a well, it is necessary to allow non-zero incident angle for synthetic seismogram calculations. A zero incident angle assumption is still valid

when reflection coefficients and the slowness of layers are calculated independently and combined later to make a reflectivity time series. From Figure 3.2-1 and Figure 3.2-2, P-P and SV-SV reflection geometry are symmetric for flat and horizontal reflectors. Seismic traces corresponding to this combined reflectivity time series form an NMO-corrected CMP gather. Table 3.5-1 shows how the convolution model is applied to reflection coefficients of multicomponent seismic data

Mode	Reflection coefficient	Slowness for depth to time conversion
P-P	ÞṔ term of Equation 3.3-a	$\Delta t_{PP} = \Delta t_p$
P-SV	ÞŚ term of Equation 3.3-a	$\Delta t_{PSV} = \frac{1}{2}(\Delta t_p + \Delta t_s)$
SV-P	ŠṔ term of Equation 3.3-a	$\Delta t_{SVP} = \frac{1}{2}(\Delta t_p + \Delta t_s)$
SV-SV	ŠŚ term of Equation 3.3-a	$\Delta t_{SS} = \Delta t_s$

Table 3.5-1: Properties used to calculate reflection coefficient time series for convolution models. Δt_{pp}, Δt_{psv}, Δt_{svp}, Δt_{ss} are slowness corresponding to P-P, P-SV, SV-P and SV-SV wave modes.

When a wavelet propagates through the Earth, wavelet properties such as frequency are likely to change. If we focus on small time intervals of interest, such wavelet changes can be minimized, and the convolution model is then valid for seismic-to-well correlation purposes.

3.6 CORRELATION METHODS

3.6.1 CROSS CORRELATION

Cross correlation can be used to measure the similarity of two waveforms, and a cross correlation coefficient is a common measurement of the quality of a seismic-to-well tie. The normalized cross correlation function $X_{AB}(\tau)$ is given as a function of the time shift τ (Equation 3.6.1-a). For seismic-to-well correlation purposes, a time shift τ that maximizes the cross correlation function is determined. Then an interpreter has to judge which horizons should be matched between synthetic and real seismograms. The advantage of cross correlation is that the procedure is clear, and matching errors can be found by interpreter's judgments. However, this technique does not allow time stretching and squeezing of the synthetic seismogram. Neither is the method appropriate for automated matching because it requires a considerable amount of interpreter judgment.

$$X_{ST}(\tau) = \frac{\sum_{k=1}^{n} S_k T_{k+\tau}}{\sum_{k=1}^{n} S_k \sum_{t=1}^{n} T_{k+\tau}} \qquad (3.6.1\text{-}a)$$

In this equation, $X_{ST}(\tau)$ is cross correlation function of S and T, S_k is a synthetic seismogram and $T_{k+\tau}$ is a time-shifted trace.

3.6.2 DYNAMIC TIME WARPING

Because the seismic wavelet is time variant and horizontal velocity does change in some earth layers, it is natural that there are mismatches between synthetic seismograms and processed seismic data. Dynamic Time Warping (DTW) is a waveform matching tool that is not limited to linear matching and allows waveforms to be stretched and squeezed (Berndt and Clifford, 1994). To find the best alignment between a synthetic seismogram and seismic traces, DTW algorithm can find an optimal path defined by Equation 3.6.2-a between synthetic and real data.

$$\boldsymbol{DTW(S,T) = min \sum_{k=1}^{p} \delta(\omega_k)} \qquad \textit{(3.6.2-a)}$$

in this expression, DTW(S,T) is the optimal path that minimizes the total warping cost of waveform S and T, $\sum_{k=1}^{p} \delta(\omega_k)$ is the total warping cost, and $\delta(\omega_k)$ is the distance of element $(i,j)_k$ expresses a the square distance

$$\boldsymbol{\gamma(i,j) = \delta(s_i,t_j) + min[\gamma(i-1,j),\gamma(i-1,j-1),\gamma(i,j-1)]} \qquad \textit{(3.6.2-b)}$$

where, $\gamma(i,j)$ the cumulative distance from (1,1) to (i,j), and $\delta(i,j)$ is the distance of element (i,j) which is defined by Equation 3.6.2-c.

$$\boldsymbol{\delta(s_i,t_j) = (s_i - t_j)^2} \qquad \textit{(3.6.2-c)}$$

where, s_i is the i-th amplitude of waveform S, and t_j is the j-th amplitude of waveform T.

The optimal time path DTW which minimizes the cumulative distance between a synthetic seismogram S=[s1,s2,s3,s4] and trace T=[t1,t2,t3] is illustrated in Figure 3.6.2-1, The warped versions of S and T are S_{warp}=[s1,s2,s3,s4] and T_{warp}=[t1,t2,t2,t3]. Here, trace T is stretched so that S and T can be matched with the minimum warping distance. If identical signal is compared with DTW algorithm, there is no time warping and the minimum distance path become diagonal as shown in Figure 3.6.2-2. An advantage of DTW for seismic-to-well correlation is that matching procedure can be more automated, and matching results can be visualized by checking if the matching result is approximates a diagonal line.

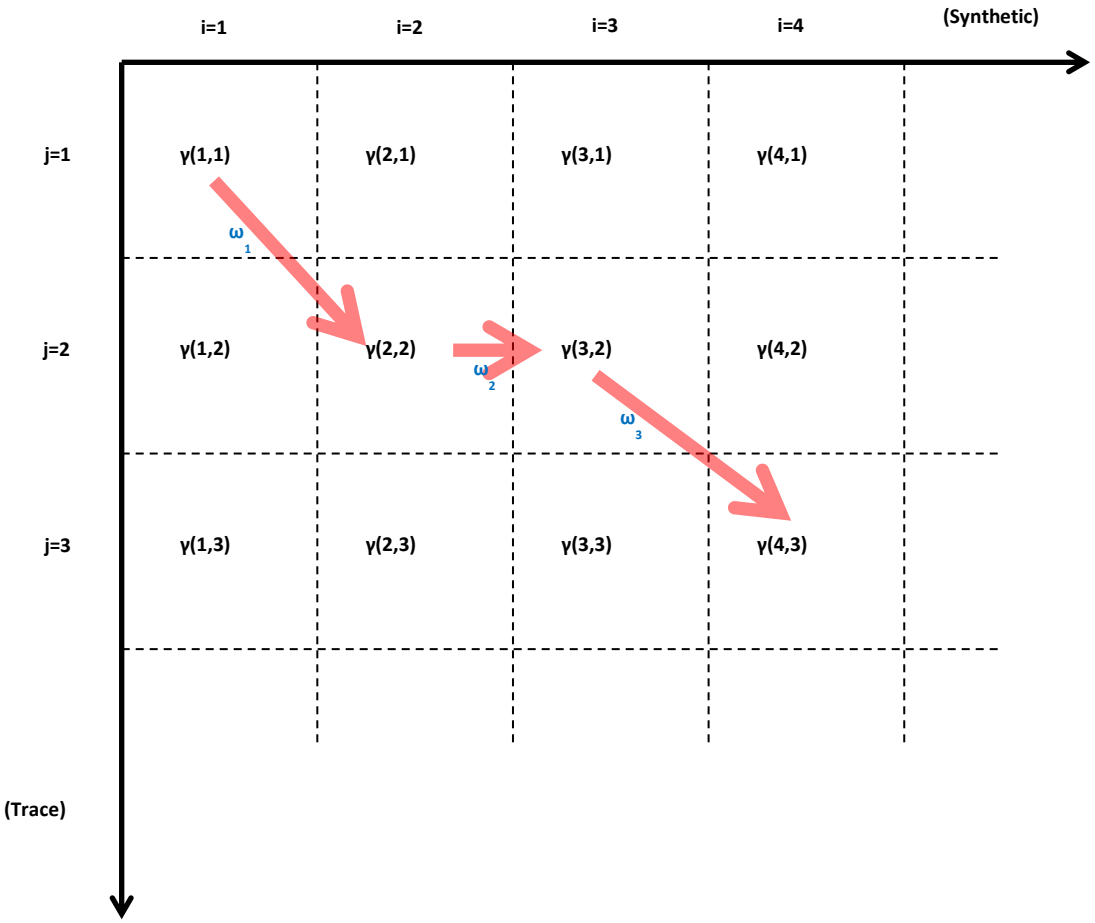

Figure 3.6.2-1: Warping path at the minimum distance between synthetic seismogram and trace. i is the index of the synthetic seismogram, j is the index of a seismic trace, and $\gamma(i,j)$ is the cumulative distance between these two earth responses.

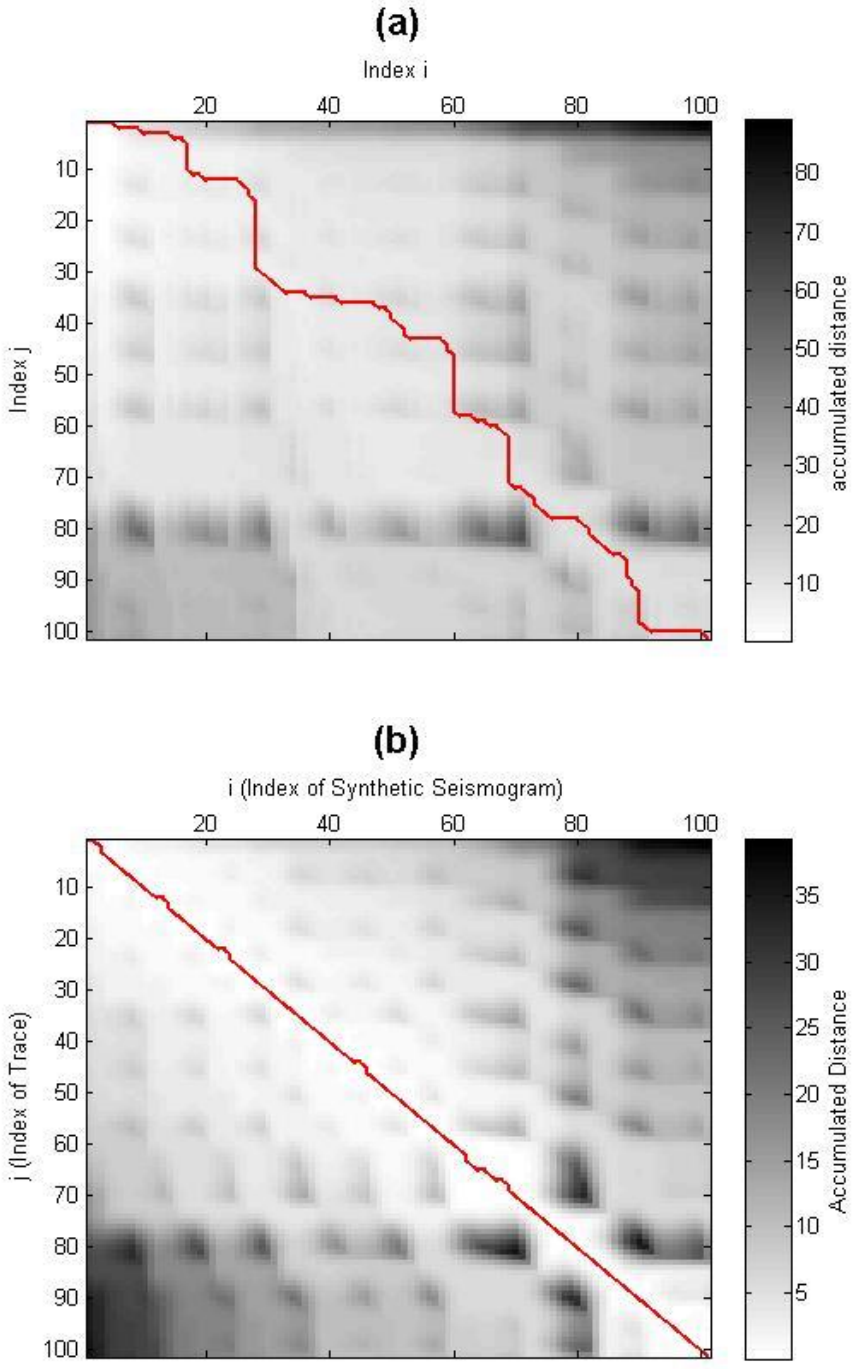

Figure 3.6.2-2: Dynamic time warping between a waveform and modified waveforms with (a) large random errors and (b) small random errors.

Chapter 4: Seismic-to-Well Correlation

4.1 WORK FLOW

Figure 4.1-1 shows the procedure for the seismic-to-well correlation. Well data (Vp, Vs, and density) and seismic traces in a specific time window corresponding to an interval of interest are read. Then, after averaging amplitude spectra of the traces, the amplitude spectrum of the wavelet is estimated statistically. However the phase spectrum of the wavelet cannot be determined directly because the solution is not unique and is assumed rather than calculated. Zero-phase wavelets and minimum-phase wavelets are the most common assumptions for wavelet extraction. A synthetic seismogram generated using the assumed phase spectrum is compared with real seismic data until the cross correlation between them is maximized. One other issue for the seismic-to-well correlation is to decide the incident angle to use to make the synthetic seismogram. Usually a zero incident angle is assumed for P-P synthetic seismogram generation. This assumption is reasonable in the sense that normal incident reflection coefficients for P-P data are usually large compare to larger incident angle cases. However, reflection coefficients of P-SV and SV-P cases are almost zero at near-zero incident angle.

An advantage of the DTW algorithm is that an automated correlation can be done to match two waveforms in a global sense and in detail. When a synthetic trace and real traces are matched so that they have maximum cross correlation, there are still mismatches at a small scale, and these mismatches need to be adjusted manually by an interpreter. Also, a DTW approach allows similarity between synthetic and real data to be seen graphically.

When a time-to-depth relationship is defined using seismic-to-well correlation, we can then investigate the general trend of the time-to-depth relationship and assume

roughly that the relationship is continuous to deeper depths where we do not have well data. This assumption had to be used in my interpretation.

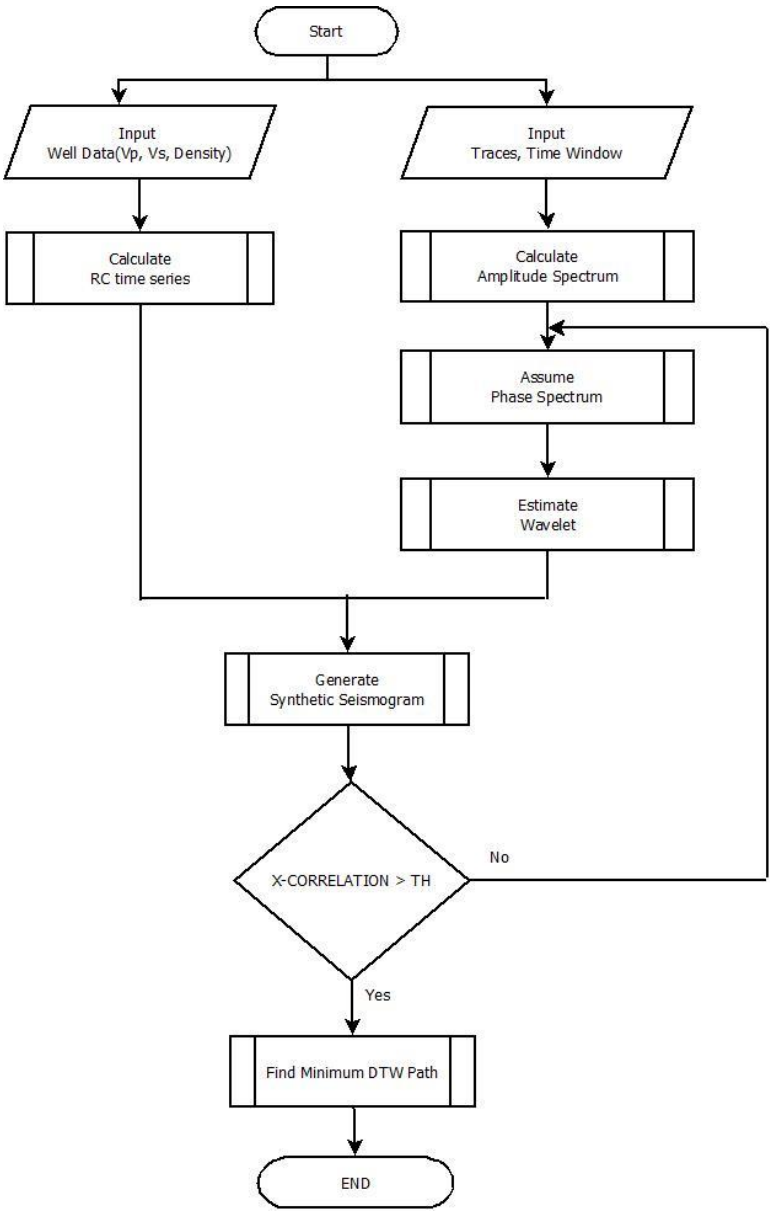

Figure 4.1-1: Flowchart for seismic-to-well correlation. TH is threshold for cross correlation.

4.2 EFFECT OF INCIDENT ANGLES

Figure 4.2-1 through Figure 4.2-3 show P-P, P-SV and SV-P synthetic seismograms for various incident angles. Reflection coefficient time series are calculated assuming 0 degree, 5 degrees, 15 degrees, and 25 degrees incident angles. Then, virtual slownesses of P-P, P-SV, and SV-P images are calculated by recursive inversion so that commercial software can create synthetic seismograms with various incident angles for P-P, P-SV, and SV-P cases just as that software does for zero incident angle P-P reflectivity. Also, for time-depth relationship calculation, the slowness of the P wave is used for P-P calculation, and the mean value of P wave slowness and S wave slowness are used for P-SV and SV-P calculation.

For P-P synthetic seismograms, the effect of incident angle change is negligible for well-to-seismic correlation purposes (Figure 4.2-1). For P-SV and SV-P calculation (Figure 4.2-2 and Figure 4.2-3), the amplitude of a synthetic seismogram increases with increasing incident angle. However, after considering relative amplitude change within each synthetic seismogram, the choice of incident angle does not affect P-SV and SV-P well-to-seismic correlation results much. Any small incident angle could be assumed when creating P-SV and SV-P seismograms unless the assumed incident angle causes unstable calculations. For the P-P case, large incident angles may change the algebraic sign of reflection coefficients and cause a large change in the synthetic seismogram. For P-SV and SV-P cases, extremely small incident angles may make the calculation of reflection coefficients unstable because there is no mode conversion at zero incident angle. In the following sections, a zero incident angle is assumed for the P-P case, and a 5-degree incident angle is assumed for P-SV and SV-P cases when correlating seismic

data and well data. Comparing Figure 4.2-2 and Figure 4.2-3, Similarity of P-SV and SV-P synthetic seismograms can be observed. This similarity will be also explained.

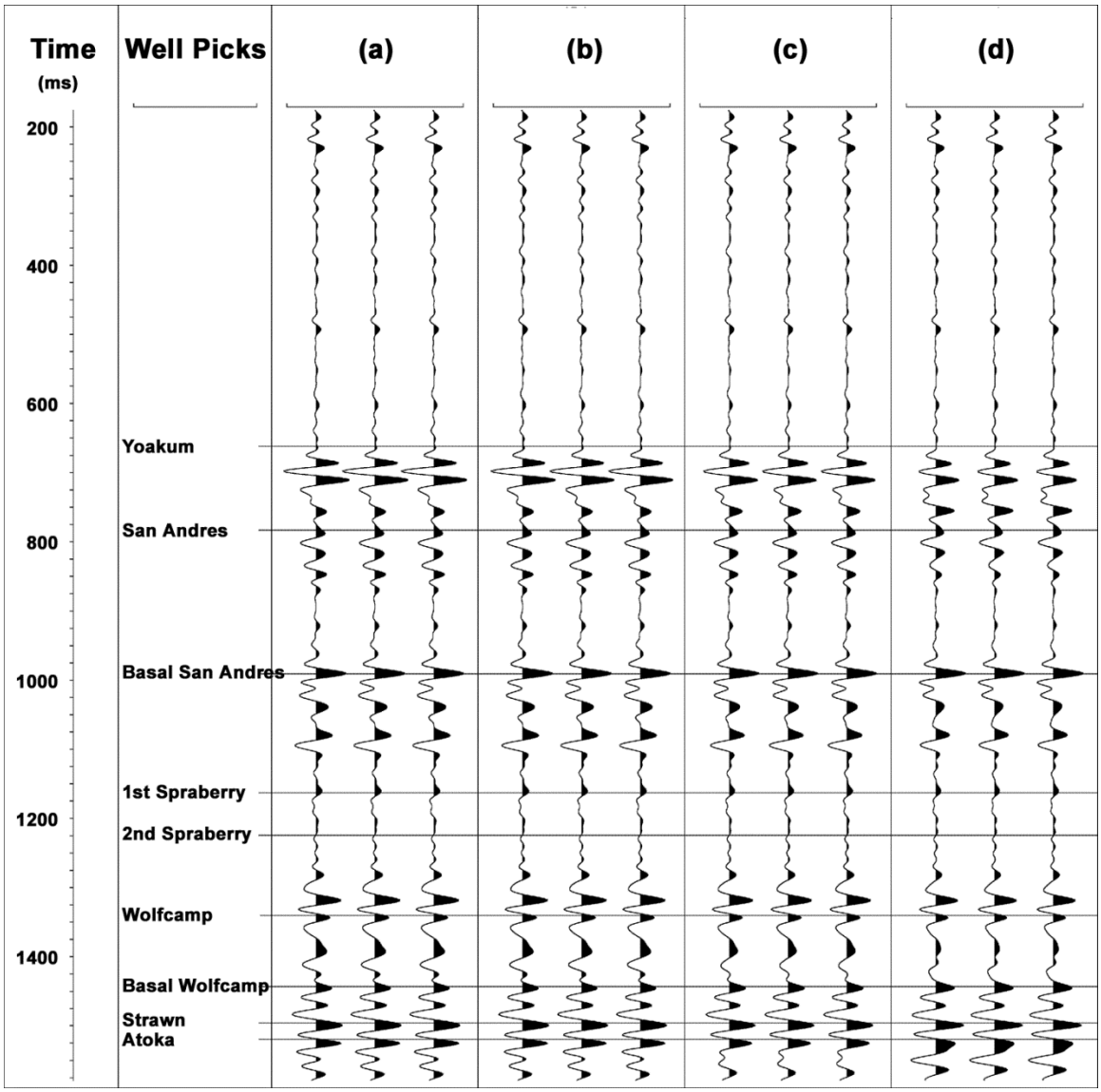

Figure 4.2-1: Effect of incident angles on well to P-P seismic correlation results. Incident angles are (a) 0 degree, (b) 5 degrees, (c) 15 degrees and (d) 25 degrees. P-P synthetic seismograms are created using various incident angles assuming zero-phase wavelet. Formation tops are identified in the left column.

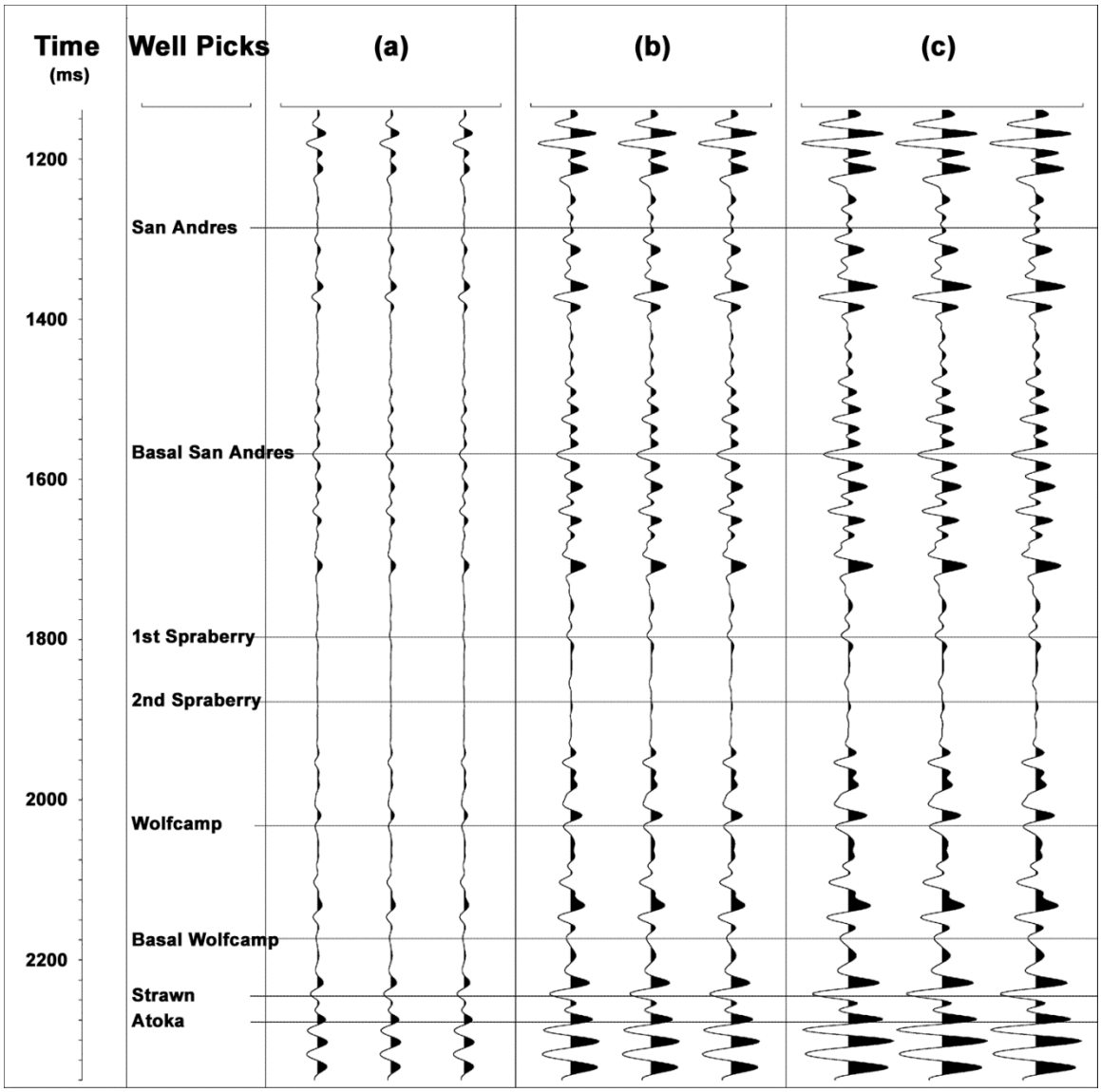

Figure 4.2-2: Effect of incident angles on well to P-SV seismic correlation results. Incident angles are (a) 5 degree, (b) 15 degrees and (c) 25 degrees. P-SV synthetic seismograms are created using various incident angles assuming zero-phase wavelet. Formation tops are identified in the left column.

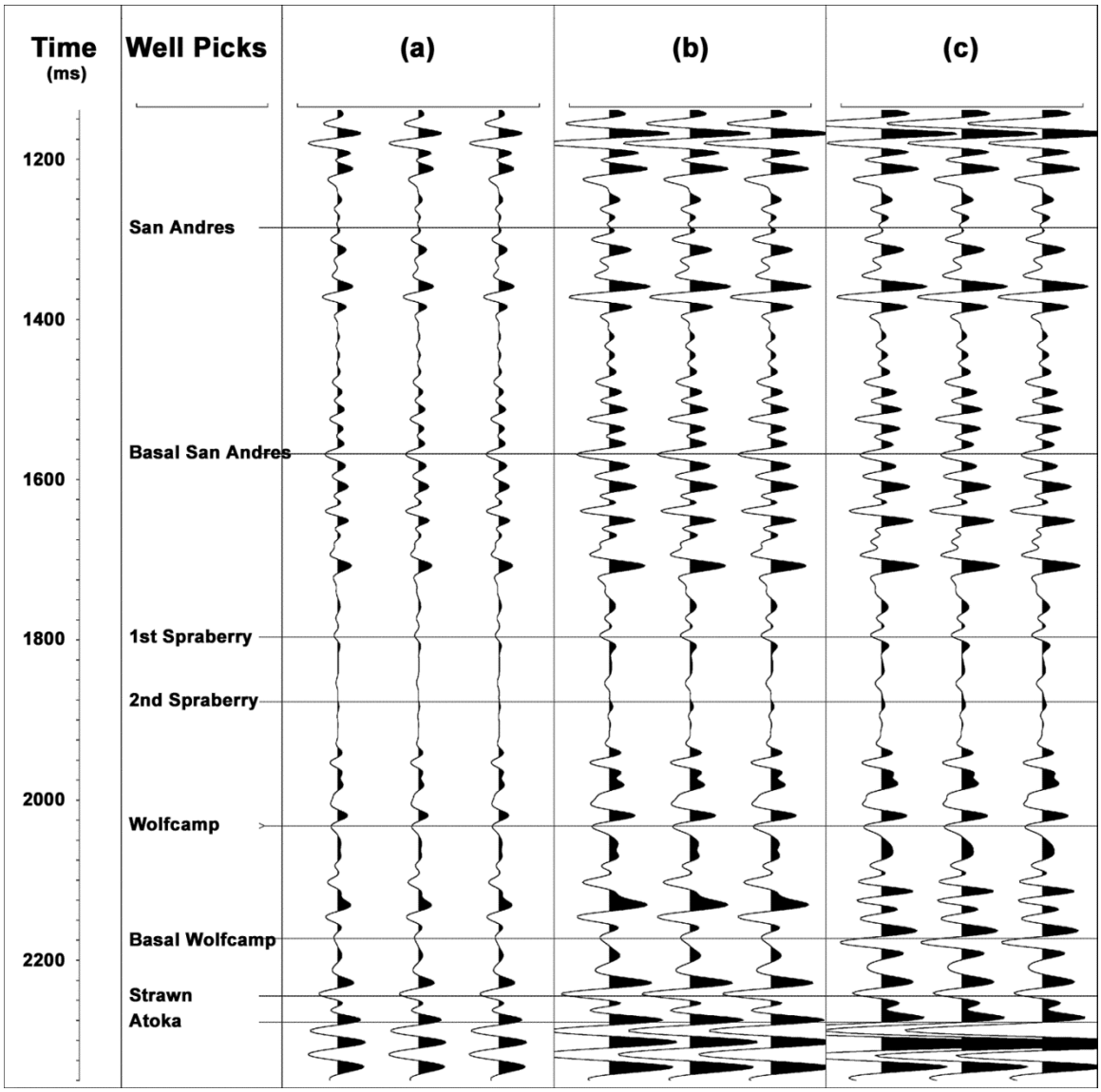

Figure 4.2-3: Effect of the incident angles on well to SV-P seismic correlation results. Incident angles are (a) 5 degree, (b) 15 degrees and (c) 25 degrees. SV-P synthetic seismograms are created using various incident angles assuming zero-phase wavelet. Formation tops are identified in the left column.

The reason why the incident-angle is not a main factor in affecting the wiggle shape of synthetic seismograms is shown in Figure 4.2-4 to Figure 4.2-7. Reflectivity curves are drawn for 200 randomly selected interfaces in calibration well FEE AL 910. Because the reflectivity curves of the P-P and SV-SV modes are mostly flat, the slopes of reflectivity curves are almost zero as shown in Figure 4.2-4 and Figure 4.2-5. Thus, P-P and SV-SV synthetic seismograms are not affected in this geology by incident-angle. For SV-P and P-SV synthetic seismograms, even though there is amplitude change with increasing incident angle, the wave shapes remain similar. To show the reason for this tendency, one sample curve is picked from the 200 curves. If the ratio between this sample curve and each of the other curves is constant for all incident angles, synthetic seismograms will have same shape even though their relative amplitudes change. Figure 4.2-6 and Figure 4.2-7 show that each curve does have almost a constant value when the reflectivity of each curve is divided by the reflectivity of the sample curve and that the slope of this ratio curve is small for relatively small incident angles.

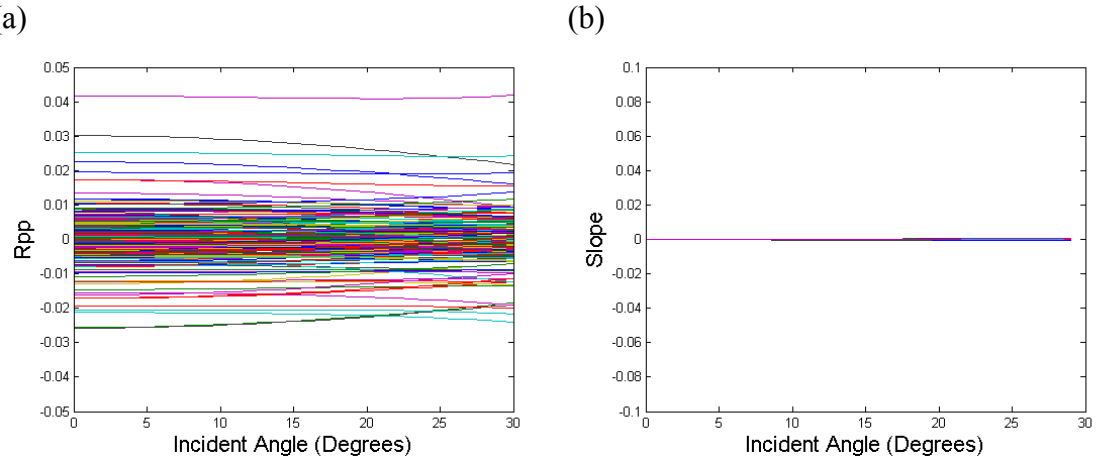

Figure 4.2-4: (a) P-P reflectivity curves for 200 randomly selected interfaces from FEE AL 910 well, (b) slope versus incident-angle plot of reflectivity curves.

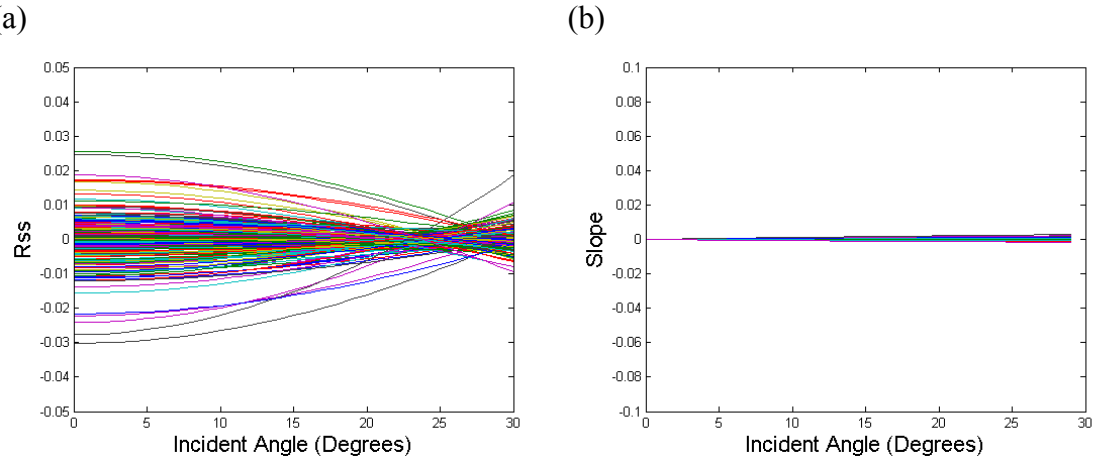

Figure 4.2-5: (a) SV-SV reflectivity curves for 200 randomly selected interfaces from FEE AL 910 well, (b) slope versus incident-angle plot of reflectivity curves.

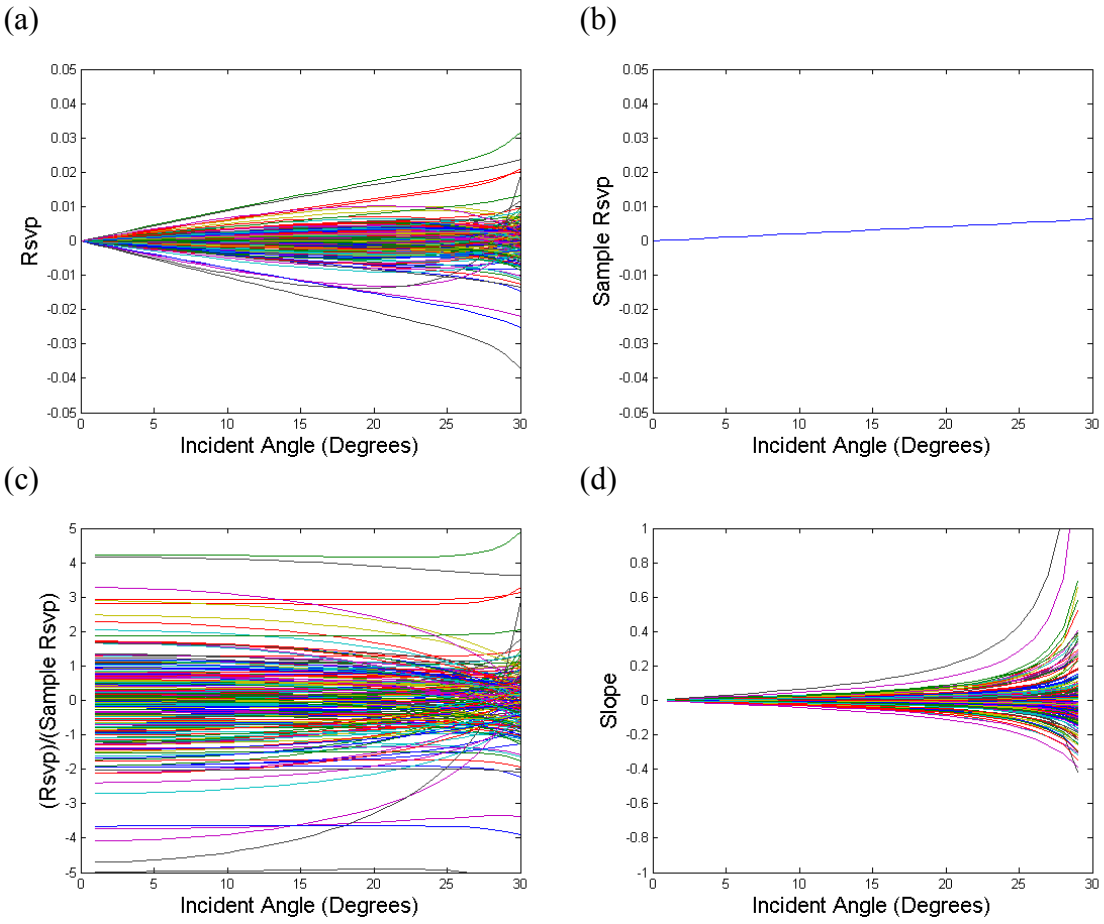

Figure 4.2-6: (a) SV-P reflectivity curves for 200 randomly selected interfaces from FEE AL 910 well, (b) sample curve picked from 200 randomly selected interfaces, (c) relative reflectivity curves of 200 randomly selected interfaces to sample reflectivity, and (d) slope of relative reflectivity versus incident angle plot of reflectivity curves.

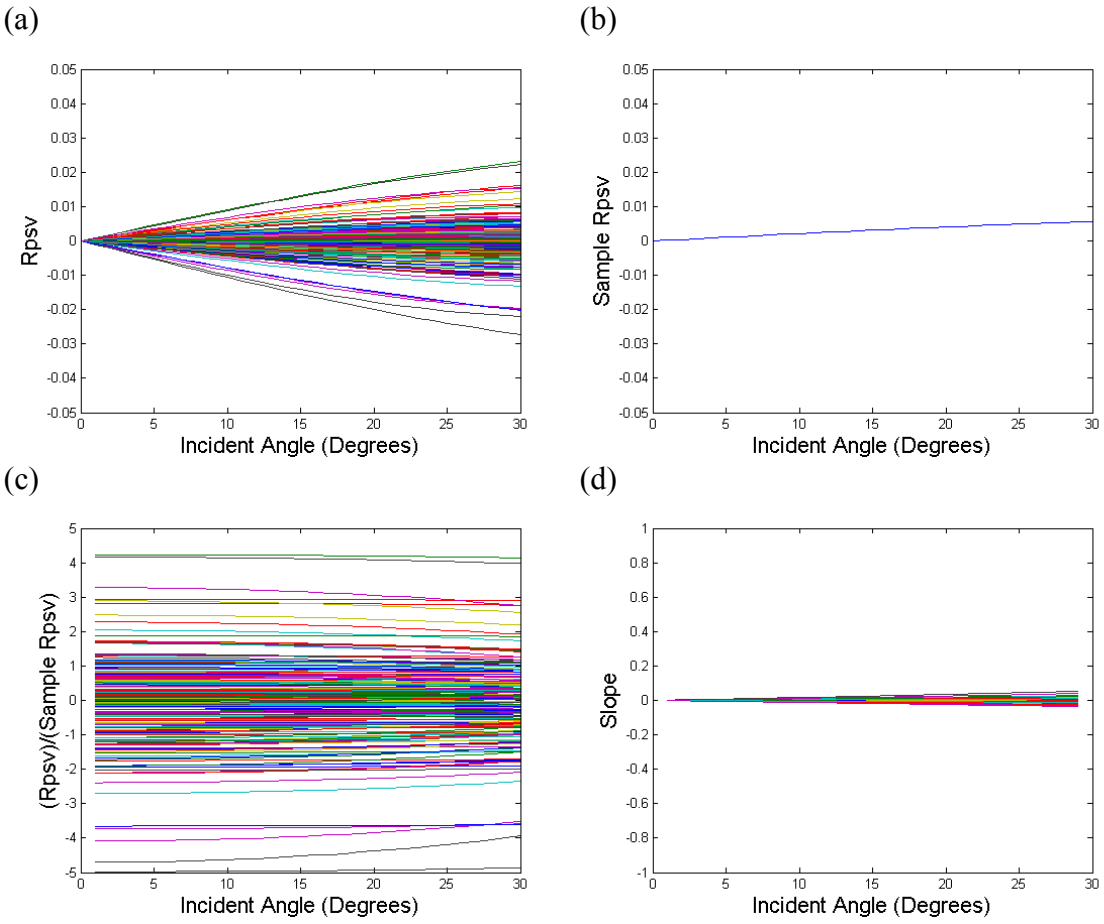

Figure 4.2-7: (a) P-SV reflectivity curves for 200 randomly selected interfaces from FEE AL 910 well, (b) sample curve picked from 200 randomly selected interfaces, (c) relative reflectivity curves of 200 randomly selected interfaces to sample reflectivity, and (d) slope of relative reflectivity versus incident angle plot of reflectivity curves.

4.3 Effect of Phase Spectrum Assumption

As shown in Figure 4.3-1, P-P synthetic seismograms were created assuming zero incident angle. Synthetic seismograms in Figure 4.3-1 are for (a) zero-phase wavelet and (b) a minimum-phase wavelet. Due to the phase difference between these wavelets, there are time lags and shape changes in the synthetic traces. In this specific example, the synthetic trace assuming zero-phase wavelet is more similar to the real data than the result assuming a minimum-phase wavelet. Probably the reason is that the energy source used to acquire the Fasken Ranch seismic data was vertical vibrators. As mentioned before, an exact phase spectrum cannot be extracted statistically from seismic traces, and a wavelet phase needs to be assumed to create synthetic seismogram. When determining the seismic-to-well correlation, synthetic seismograms need to be created using various phase spectra and compared with real traces to find the optimal matching combination.

In Figure 4.3-1, synthetic seismograms and real seismic traces are matched so that the real seismic traces have maximum cross correlation with synthetic seismogram assuming a zero-phase wavelet. If a synthetic seismogram made by a minimum-phase wavelet is used for seismic-to-well correlation instead of the zero-phase wavelet, the matching result will change by approximately the time lag of the wavelet peak caused by the phase change. In this sense, the accuracy of seismic-to-well correlation depends mainly on whether the wavelet phase assumption is reliable or not.

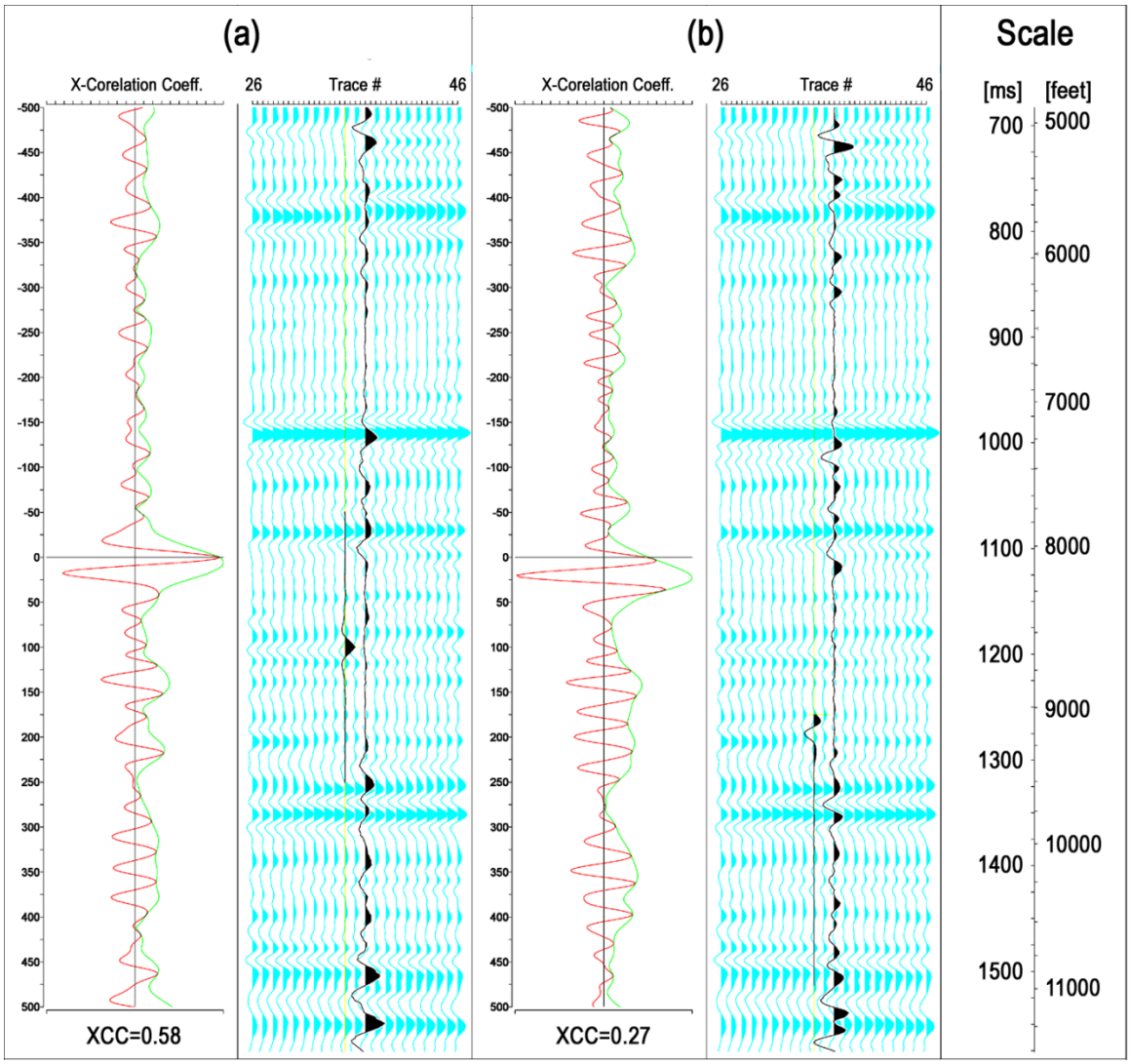

Figure 4.3-1: Comparison between P-P synthetic seismograms created assuming (a) zero-phase wavelet, and (b) minimum-phase wavelet. Cross correlation coefficient curve (red), wavelet (black) and synthetic trace (black) and real traces (sky blue) are shown for each case. The amplitude spectrum is extracted statistically and phase spectra are assumed to create P-P synthetic seismograms.

4.4 TIME-TO-DEPTH RELATIONSHIP

Seismic-to-well correlation results are shown in Figure 4.4-1 to Figure 4.4-3. Zero degree incident-angle is used for the P-P synthetic seismogram creation, and 5-degree incident angles are assumed for P-SV and SV-P synthetic seismograms. As shown previously, for the Fasken Ranch seismic data, the choice of incident angle does not affect the seismic-to-well correlation result much for converted-mode data. Comparing these matching results, the correlation coefficient of the P-P data is good (0.58) and that of SV-P data is relatively good (0.32). The seismic-to-well correlation of P-SV data was done so that it had a local maximum correlation coefficient that had a time-depth relationship similar to the SV-P data rather than using its global maximum correlation coefficient. This approach was done because the correlation coefficient between the P-SV synthetic and real data is too small (0.09) within a reasonable range of time lags. Considering the poor correlation result of P-SV data, it seems that the quality of the real P-SV data is not good. Assuming that the P-SV data are processed properly, a possible explanation for bad quality P-SV data is that the 3C geophone were not buried but placed on the surface of the ground using only spikes, which could lead to poor coupling. It is important to note that the quality of SV-P data at Fasken Ranch was much better than the quality of P-SV data. Using laboratory and field measurements, Krohn (1984) pointed out that data quality from vertical geophone can be increased using longer spikes or burying the geophone; however, good quality data from horizontal geophones can be achieved only when it is buried in ground.

Comparing Figure 4.4-2 and Figure 4.4-3, reflection coefficients of P-SV and SV-P data are very similar, even though synthetic seismograms of these modes are not.

Synthetic seismogram variations are due to the use of different wavelets that were extracted from P-SV and SV-P data, respectively.

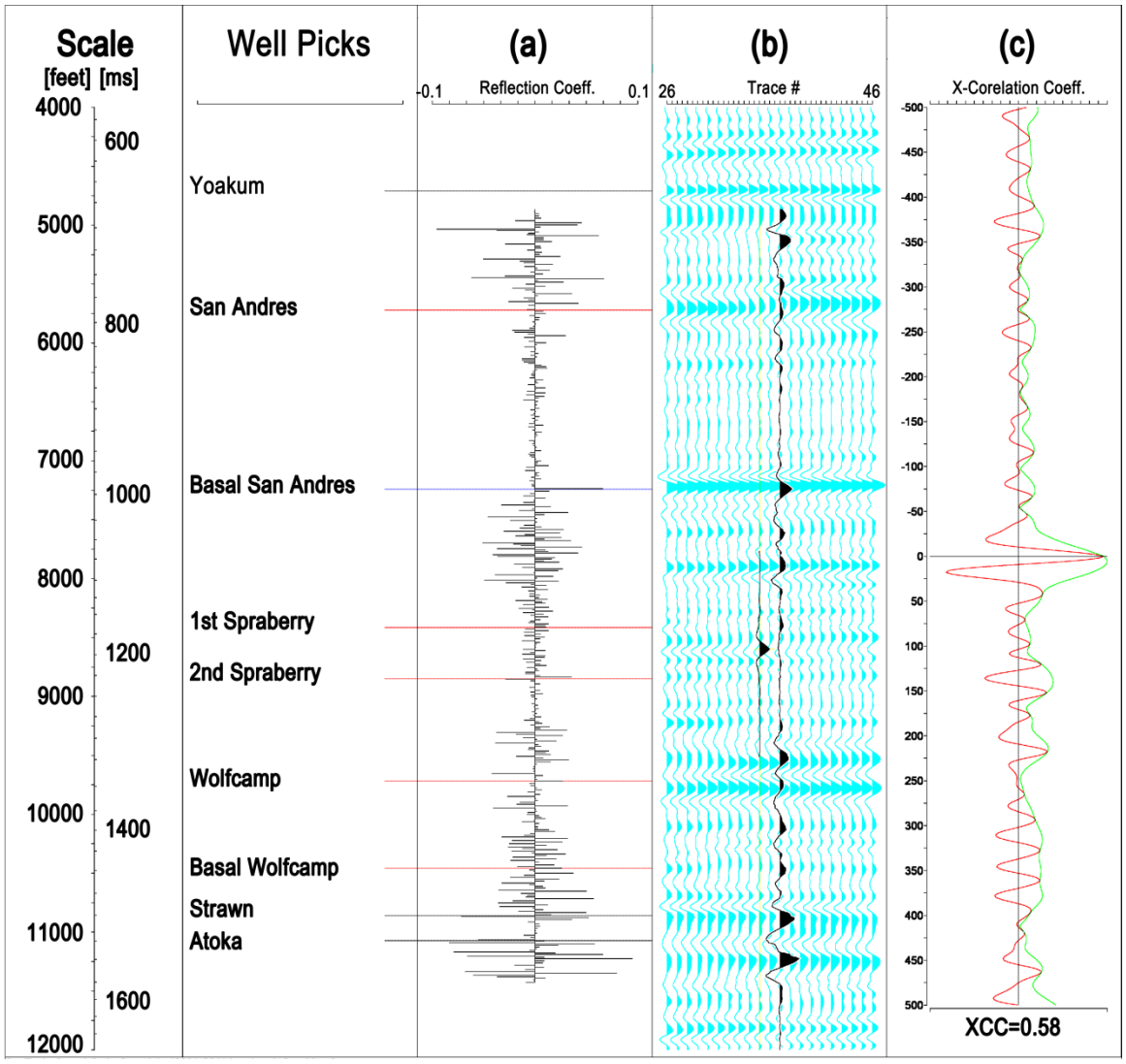

Figure 4.4-1: Seismic-to-well correlation result of P-P image. Correlation coefficient at zero lag time is 0.58. Formation tops are identified in the left column with (a) Reflection coefficient time series, (b) Synthetic seismogram (black) and real seismogram (sky blue), and (c) cross correlation analysis.

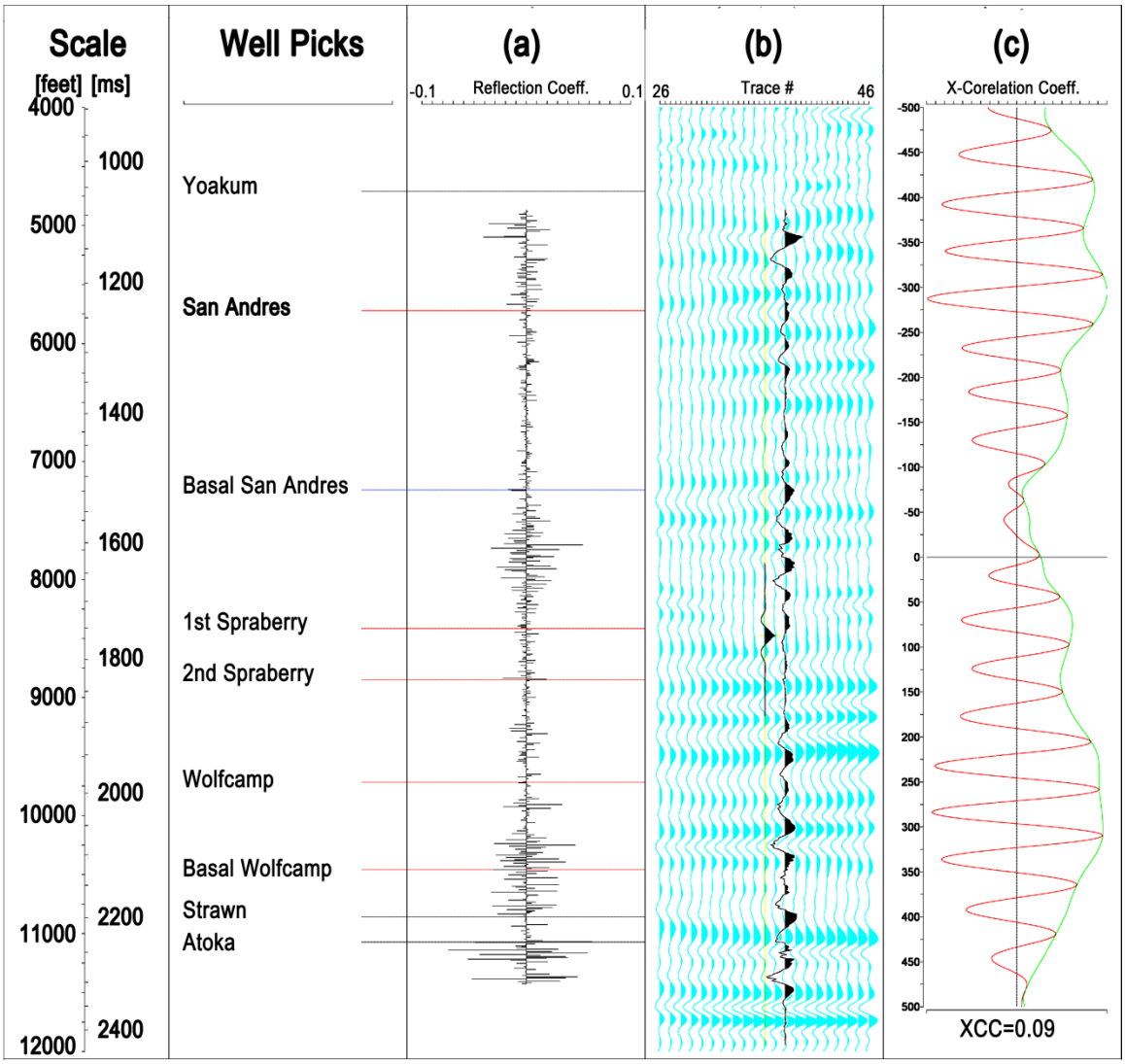

Figure 4.4-2: Seismic-to-well correlation result of P-SV image. Correlation coefficient at zero lag time is 0.09. Formation tops are identified in the left column with (a) Reflection coefficient time series, (b) Synthetic seismogram (black) and real seismogram (sky blue), and (c) cross correlation analysis.

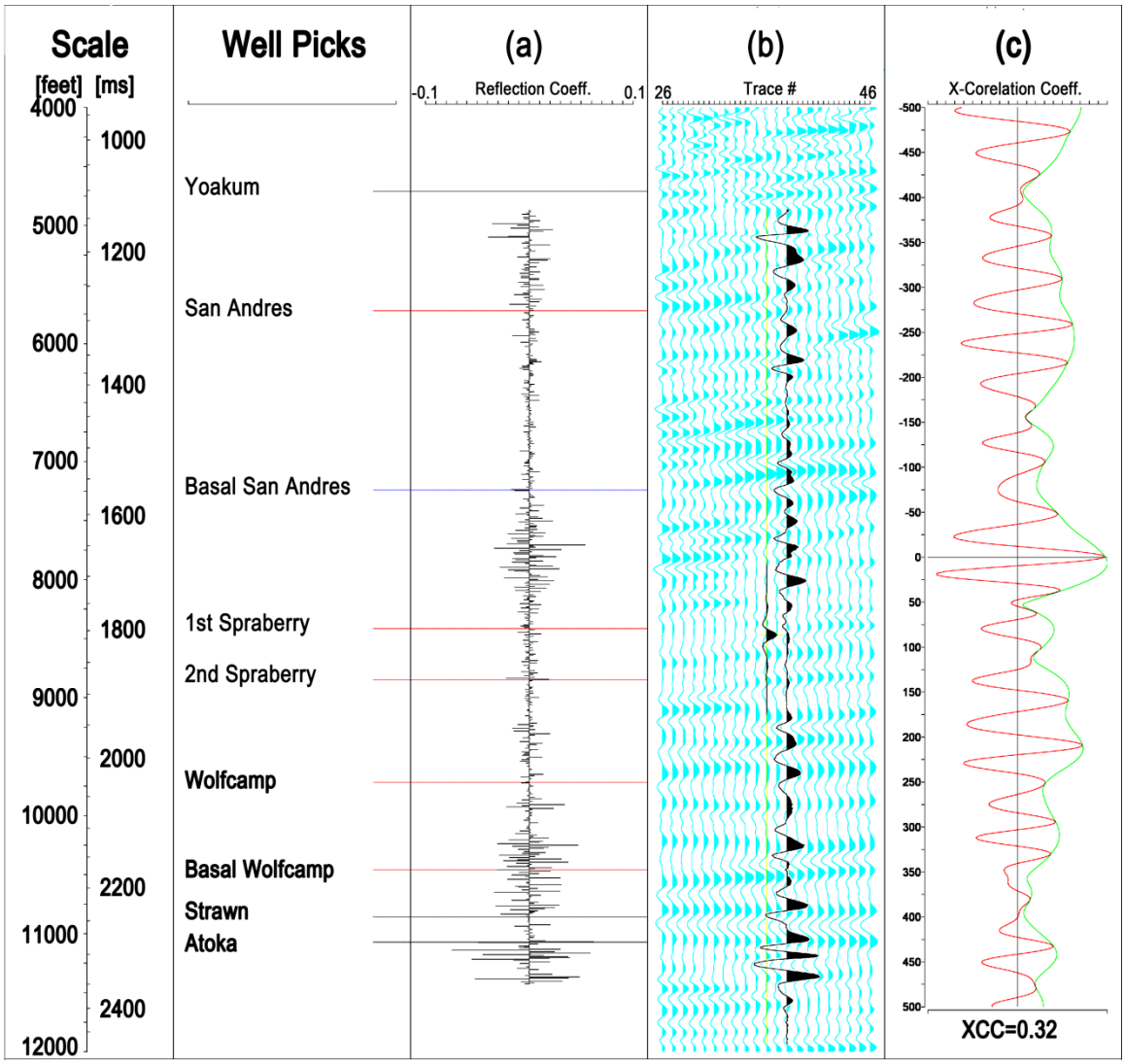

Figure 4.4-3: Seismic-to-well correlation result of SV-P image. Correlation coefficient at zero lag time is 0.32. Formation tops are identified in the left column with (a) Reflection coefficient time series, (b) Synthetic seismogram (black) and real seismogram (sky blue), and (c) cross correlation analysis.

For homogenous isotropic media, P-SV and SV-P seismic traces are similar theoretically; however, as shown in Figure 4.4-4, P-SV and SV-P data are significantly different at Fasken Ranch. P-SV data are lower frequency and more laterally continuous than SV-P data, and the P-SV data have lower resolution than the SV-P data. Laterally continuous reflections as shown by the P-SV data do not conform to a heterogeneous stack of turbidite units that are known to form the Wolfberry section (Hamlin and Baumgardner, 2012). In contrast, SV-P data displayed chaotic reflection patterns that would be expected for turbidite deposits.

Power spectra for wavelets extracted from P-SV image and SV-P image are shown in Figure 4.4-5. The extracted P-SV wavelet loses high-frequency components and has a narrower frequency range comparing to the SV-P wavelet. Together with the data quality issue, these differences indicate SV-P data are better for detecting lateral changes in lithology at this study location.

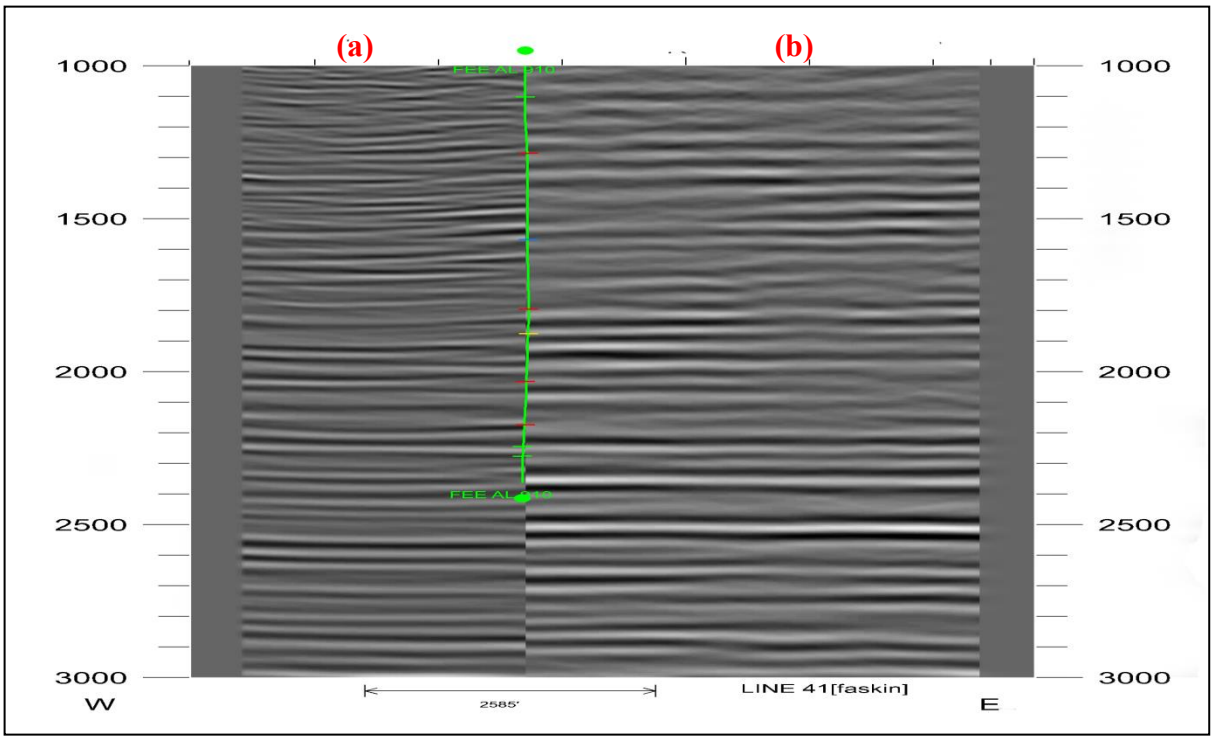

Figure 4.4-4: Comparison of (a) SV-P image and (b) P-SV image at calibration well. Positive amplitude is displayed with black and negative amplitude is displayed with white.

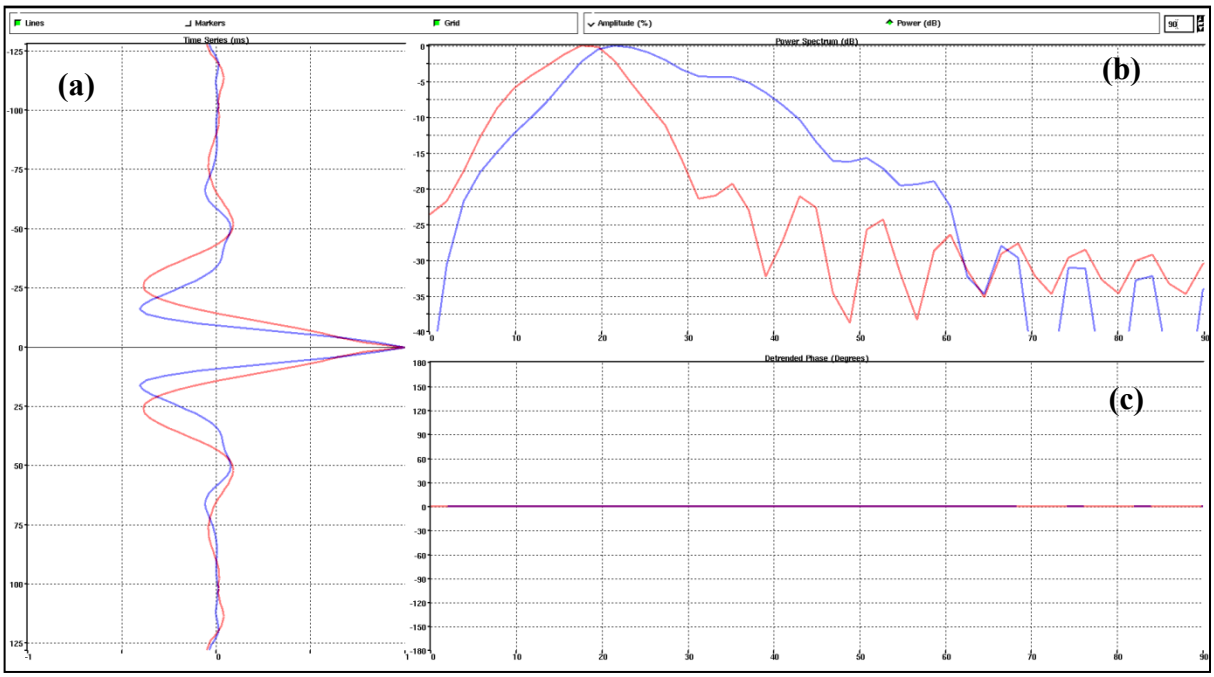

Figure 4.4-5: (a) Wavelet time series, (b) power spectra of P-SV (red) and SV-P (blue), and (c) phase spectra of wavelets extracted from P-SV and SV-P images. Same time interval (1200 ~ 2300 ms) is used to extract each wavelet, and zero-phase wavelets are assumed.

4.5 EXTRAPOLATION OF TIME-TO-DEPTH RELATIONSHIP

If a time-to-depth relationship is generally linear after matching to real data, we may assume that this linear time-to-depth relationship is valid across the study area and can be used for deeper layers where no log data have been acquired. This assumption had to be applied for me to interpret the deep pre-Wolfberry geology at Fasken Ranch.

Figure 4.5-1 shows seismic-to-well correlation results of (a) P-P, (b) P-SV and (c) SV-P images. Synthetic traces and real traces are matched so that they have maximum cross correlation, and local mismatches are adjusted with dynamic time warping as shown in Figure 4.5-2. Figure 4.5-3 shows accumulated distances of (a) P-P, (b) P-SV and (c) SV-P traces generated during DTW. In Figure 4.5-3, data points that have earlier index numbers do not match well. It seems that these mismatches are caused by bad well data quality around 5,000 ft. DTW is used to measure the similarity of two waveforms, to match these two waveforms, and to assess the linear nature of the time-to-depth relationship. Before using DTW, two waveforms need to be roughly matching using maximum cross correlation method. The time-to-depth relationship after DTW shows detailed matching results. Matching by maximum correlation is applicable only for general/global matching, but for detailed/local matching an interpreter still needs to match each peak and trough of two traces manually. In contrast, when using DTW, two traces are stretched and squeezed so that they have minimum accumulation distance and are matched in detail.

In Figure 4.5-1, the time-to-depth relationship before DTW is almost linear because it is calculated using average slowness of P and S wave. Matching results of P-P and SV-P image after DTW are almost linear with minor mismatches; however, the match of P-SV data after DTW is not good enough because there is an unreasonable

departure from a linear trend. Then, to match deeper intervals without well data, a general linear time-to-depth relationship is assumed for P-P and SV-P data, and the time-to-depth relationship of P-SV data is replaced with that of SV-P data because of the theoretical similarity of P-SV and SV-P images.

(a)

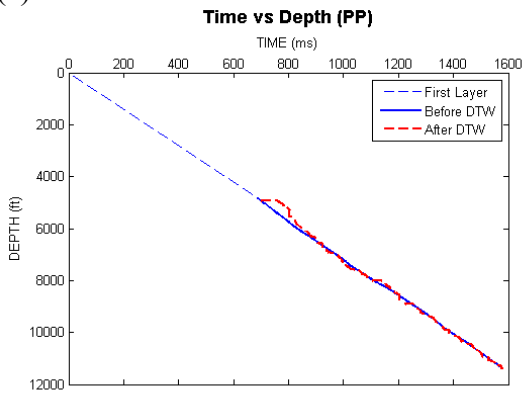

(b)

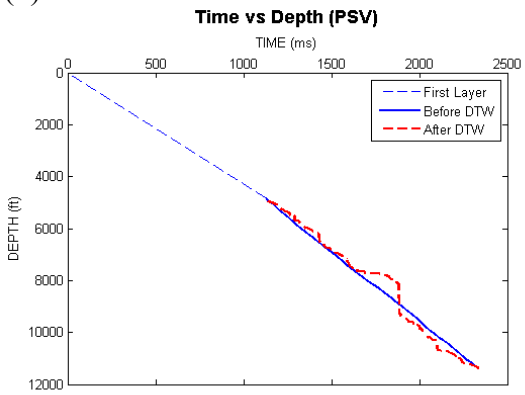

(c)

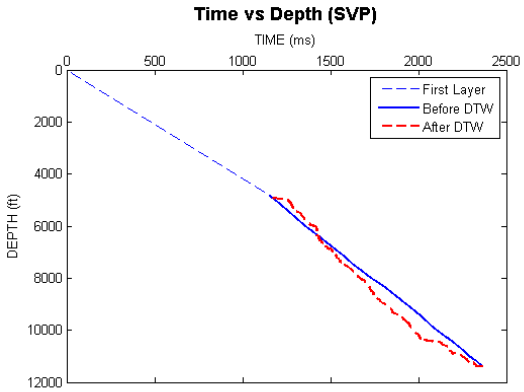

Figure 4.5-1: Time-to-depth relationship of (a) P-P, (b) P-SV and (c) SV-P images. Dashed blue lines stand for first layer which are assumed to have constant velocity without well data. Blue solid lines are the matching results from correlation study. Dashed red curves are detailed matching result using dynamic time warping.

(a)

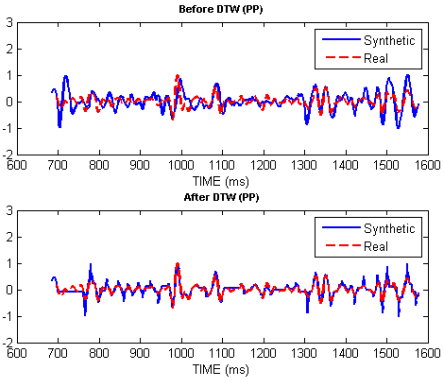

(b)

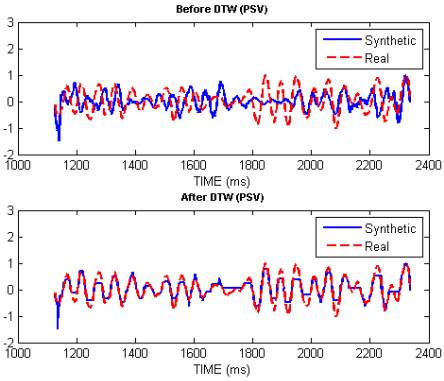

(c)

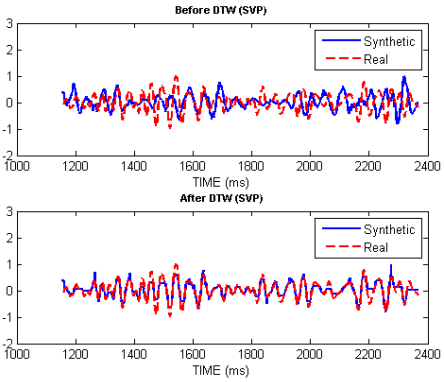

Figure 4.5-2: Dynamic time warping matches between synthetic and real traces of (a) P-P, (b) P-SV, and (c) SV-P images. Red dashed curves are real traces and blue solid curves are synthetic traces.

(a)

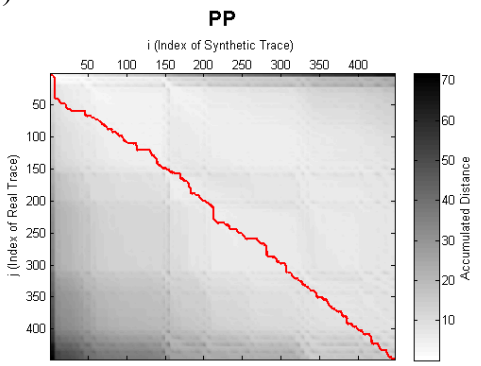

(b)

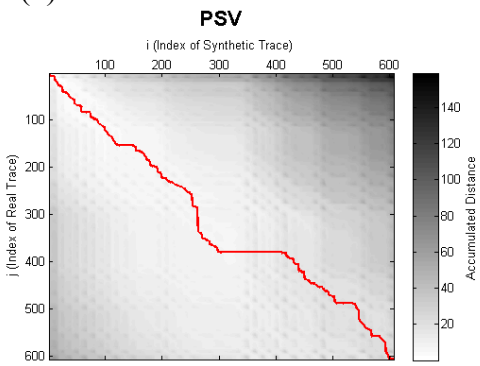

(c)

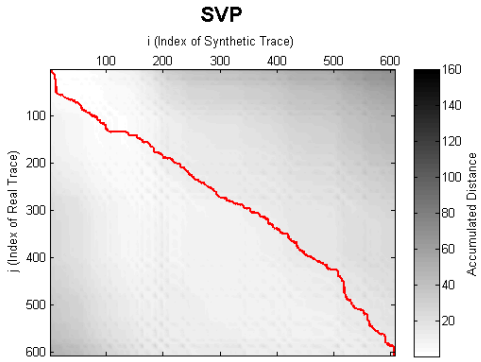

Figure 4.5-3: Warping path of the minimum distance between synthetic traces and (a) P-P, (b) P-SV, and (c) SV-P real traces

4.6 STRATAL SLICING

Stratal slicing is a horizon picking technique that allows any seismic attribute to be extracted on a surface corresponding to a fixed geologic time (Zeng, 2010). Figure 4.6-1 shows the concept of stratal slicing. If picked horizons in a seismic section follow chronostratigraphic correlation patterns rather than time-transgressive lithostratigraphic units as Vail et al. (1977) assumed, stratal slices can be created by interpolating arbitrary number of slices between these picked horizons. Each stratal slice between these two horizons would represent a surface corresponding to a certain geologic time. There are arguments about the validity of Vail et al. (1977)'s assumptions; however, even if the assumptions are not valid, stratal slice is still a useful tool for multicomponent seismic image comparisons because each multicomponent seismic image is transformed to a new relative geologic time section. When surfaces are picked in multicomponent seismic images so that they correspond to the same geologic event, interpolated stratal slices in one image are roughly equivalent to those in other images in terms of geologic time. Also, difficulty in image comparison caused by velocity differences between P-waves and S-waves can be reduced using stratal slices and geologic-time section. In this thesis, it is assumed that a seismic reflection event follows a chronostratigraphic surface and that a stratalslicing technique can used for multicomponent seismic image comparisons. Examples in which this technique is used for interpretation purposes can be seen Hardage et al. (2011, 2015).

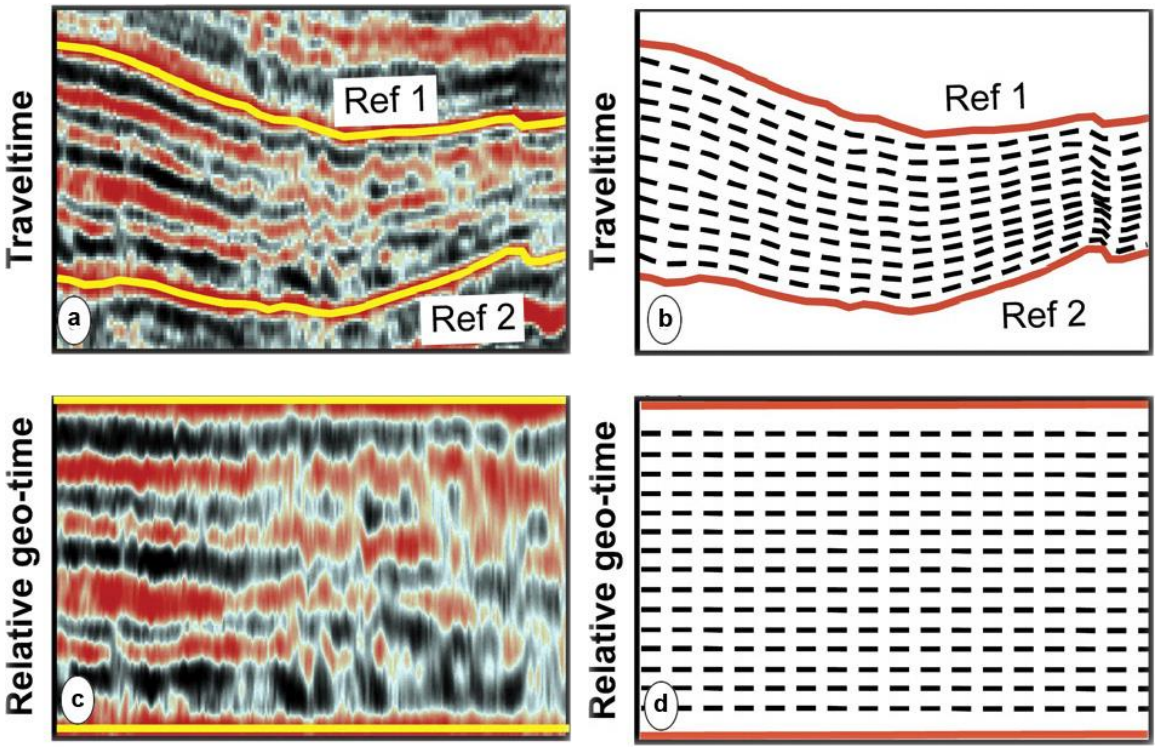

Figure 4.6-1: Concept of stratal slicing. (a) Picked chronographic surfaces (Ref1 and Ref2) in a traveltime section, (b) interpolated stratal slices in traveltime section, (c) flattened chronographic surfaces in relative a geologic time section, and (d) interpolated stratal slices in that geologic-time section (modified from Zeng, 2010)

4.7 SEISMIC ATTRIBUTES: RMS AMPLITUDE AND SEMBLANCE

Chopra and Marfurt (2007) defined seismic attributes as "A seismic attribute is any measurement of seismic data that helps us visually enhance or quantify features of interpretation interest." Seismic attributes are more helpful for detecting regional patterns that are understood by interpreters rather than directly estimating rock properties.

In this thesis, to compare multicomponent seismic images, RMS amplitude (Equation 4.7-a) and semblance defined by the Manhattan distance (Equation 4.7-b) are used. RMS amplitude is calculated as the square root of the average of squares of the amplitudes between two horizons. Rock properties may not directly be related with RMS amplitude, and it seems more reasonable to view RMS amplitude anomalies as indicating geologic events such as turbidite flows. Semblance is useful for detecting lateral trace changes caused by faulting, lithology change, or stratigraphic changes. Low Manhattan values indicate a very uniform geology or low dissimilarity, and high values indicate high dissimilarity.

$$\boldsymbol{RMS\ Amplitude} = \sqrt{\frac{1}{N}\sum_{i=1}^{N} a_i^{\,2}} \qquad \textit{(4.7-a)}$$

In this equation, N is the number of samples with in the interval and a_i is the amplitude of ith sample

$$M_d = S \frac{\sum_{k=N-n/2}^{k=N+n/2} |G_k - H_{k+d}|}{\sum_{k=N-n/2}^{k=N+n/2} (|G_k| + |H_{k+d}|)} \qquad (4.7\text{-}b)$$

In this expression, M_d is the Manhattan distance, n is the number of samples in the wavelet, d is the integer sample shift, N is the center sample of the reference trace, S is a scale factor, G is the amplitude of the reference trace, and H is the amplitude of the target trace.

Chapter 5: Results and Discussion

5.1 Depth Registration Result

By calculating cross correlation coefficients between synthetic and real seismograms, time-to-depth relationships of P-P, SV-P, and P-SV images were determined. For synthetic seismogram generation, zero incident angle and a zero-phase wavelet are assumed for the P-P mode, and 5 degrees of incident-angle and a zero-phase wavelet are assumed for SV-P and P-SV modes. Because cross correlation coefficients of the P-SV mode are small, the time-to-depth relationship for P-SV data is replaced with that of SV-P data, based on theoretical similarity between P-SV and SV-P modes. Well picks from the FEE AL 910 calibration well, which are expressed in the depth domain, are matched with the traveltime of each image mode so that the cross correlation between synthetic seismograms and real trace can be maximized. By assuming the same time-to-depth trend, the position of the deeper Ellenburger Formation is estimated. Horizons are picked so that they pass through known formation tops and are then iteratively adjusted so that the Vp/Vs velocity ratio is within reasonable ranges. A deep horizon (ZZ) is roughly positioned based on the Vp/Vs velocity ratio and the shape of seismogram. Velocity ratio maps for picked intervals are shown on Figure 5.1-1 through Figure 5.1-4. Two constraints for horizon picking are: (1) horizons are picked so that they follow seismic patterns such as peaks and troughs, (2) the Vp/Vs velocity ratio between adjacent horizons should be reasonable. In case these two conditions cannot be satisfied together, the velocity ratio requirement is given the greater weight because the chaotic seismic

response for carbonate makes it difficult to interpret a consistent peak or trough. Finally, 4000 stratal slices are generated across the interval defined through interpretation.

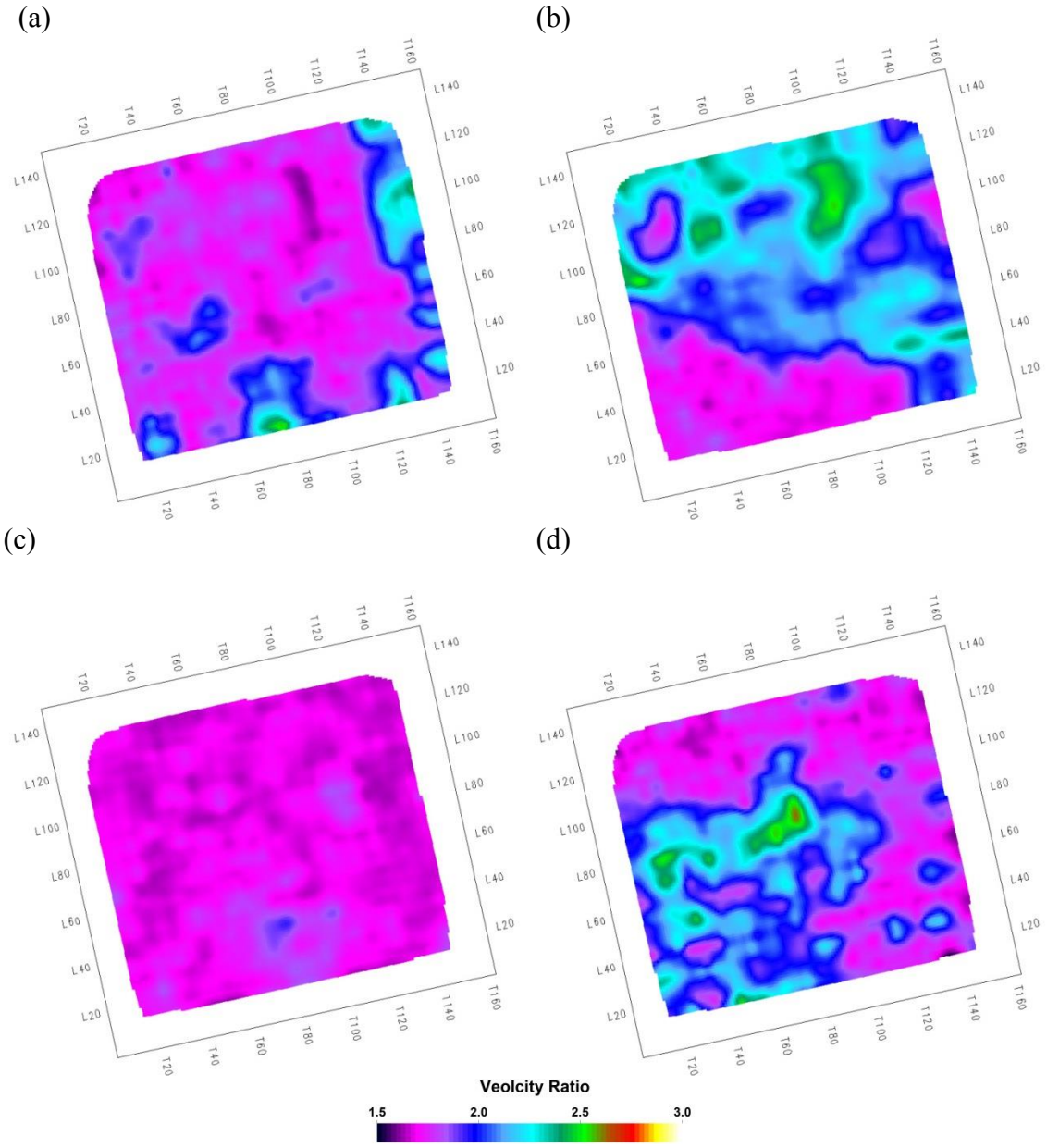

Figure 5.1-1: Velocity ratio maps from P-P image and SV-P image between (a) the 1st Spraberry and the 2nd Spraberry, (b) the 2nd Spraberry and the Wolfcamp, (c) the Wolfcamp and Basal Wolfcamp, (d) the Basal Wolfcamp and the Strawn.

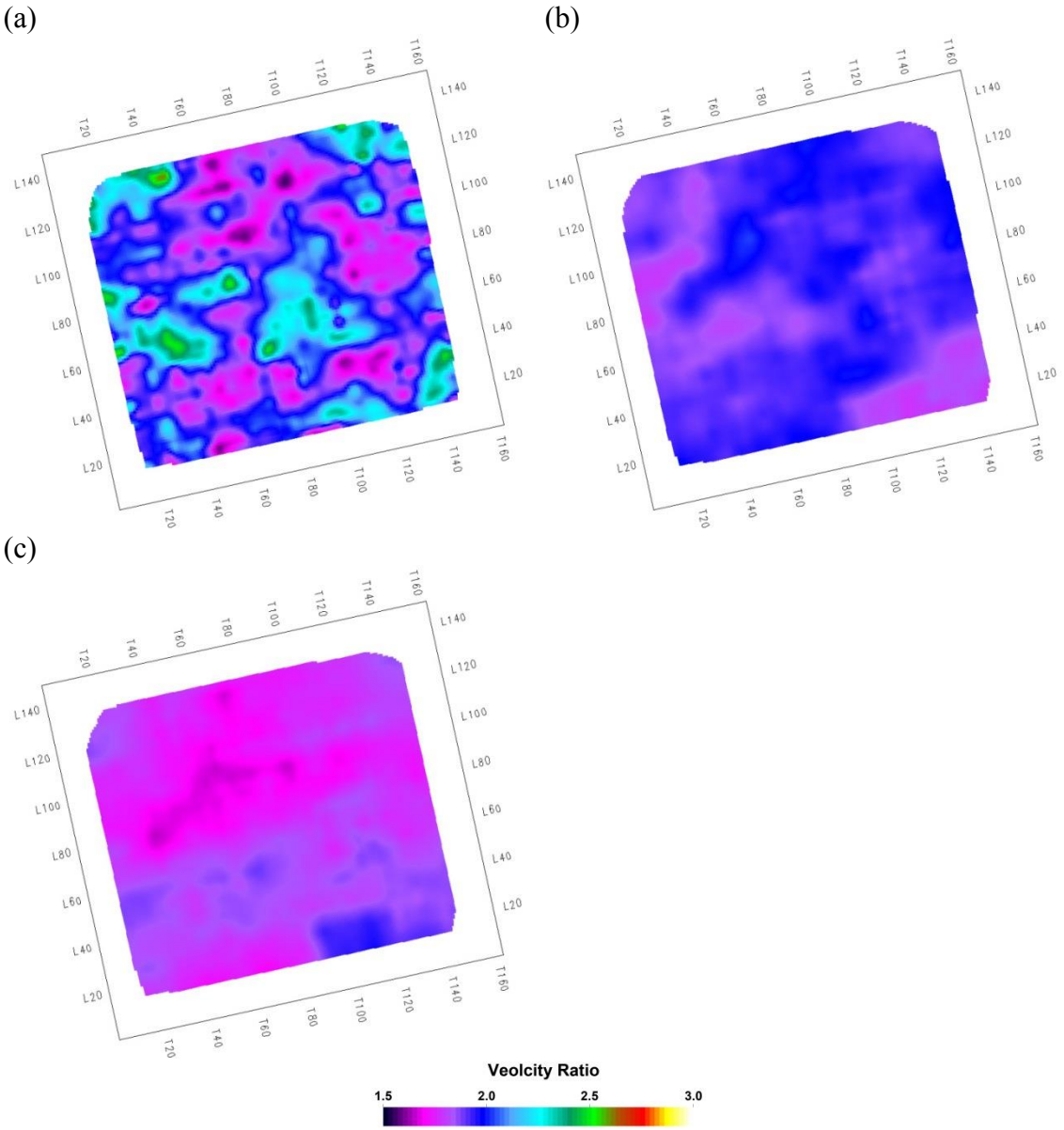

Figure 5.1-2: Velocity ratio maps from P-P image and SV-P image between (a) the Strawn and the Atoka, (b) the Atoka and the Ellenburger, (c) the Ellenburger and the picked horizon ZZ.

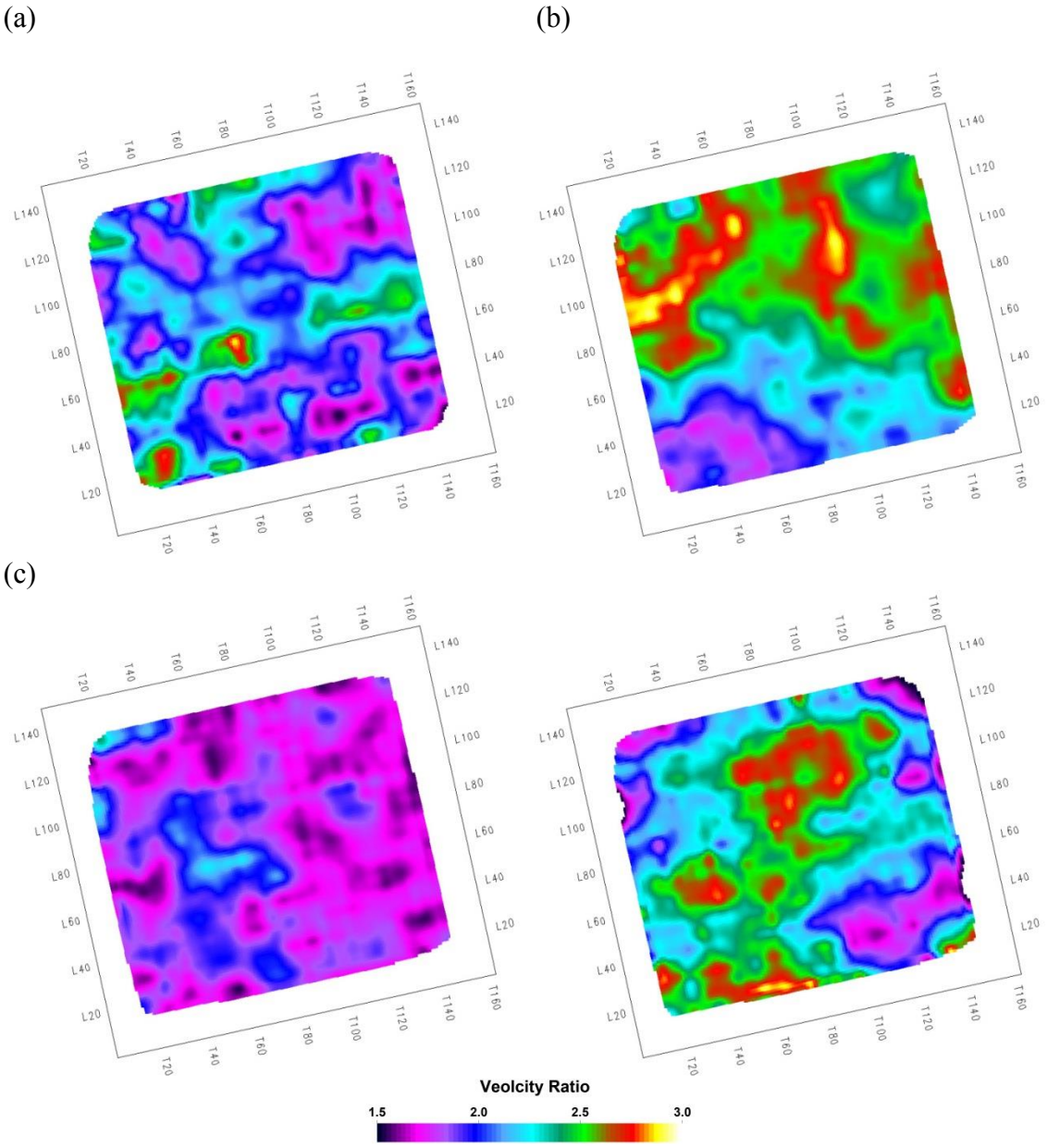

Figure 5.1-3: Velocity ratio maps from P-P image and P-SV image between (a) the 1st Spraberry and the 2nd Spraberry, (b) the 2nd Spraberry and the Wolfcamp, (c) the Wolfcamp and Basal Wolfcamp, (d) the Basal Wolfcamp and the Strawn.

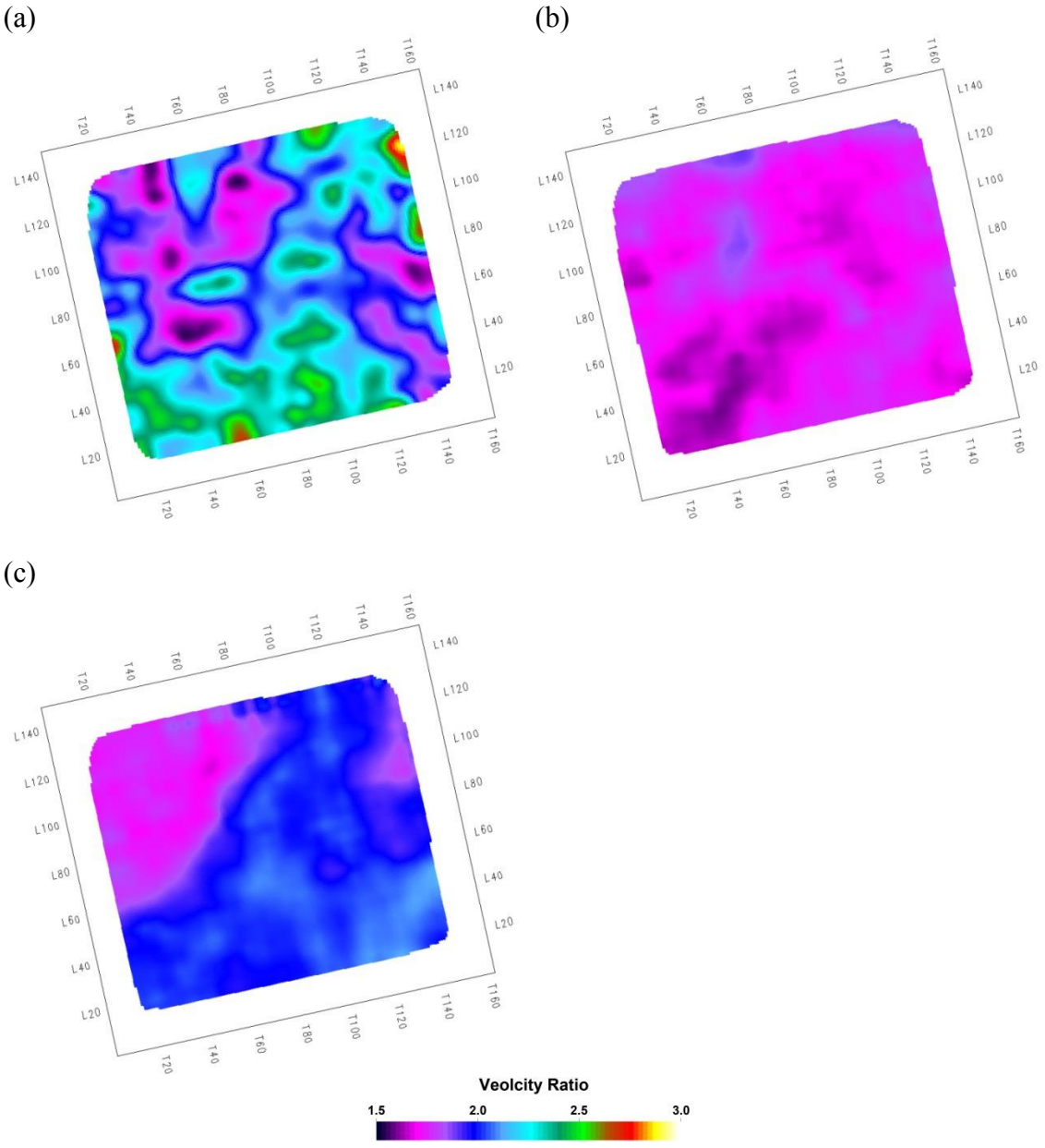

Figure 5.1-4: Velocity ratio maps from P-P image and P-SV image between (a) the Strawn and the Atoka, (b) the Atoka and the Ellenburger, (c) the Ellenburger and the picked horizon ZZ.

Figure 5.1-5 through Figure 5.1-7 show geologic time section views of each image. From the 1st Spraberry to the Atoka, matching accuracy is relatively high because these horizons are determined with synthetic seismograms made from well data. Matching accuracy between the Atoka and the Ellenburger is medium because the time-to-depth relationship has to be extrapolated from shallow geology to deep geology. The match of the deep Ellenburger and the pre-Ellenburger horizon (ZZ) is relatively low because they are matched based only on interpreted wave patterns and Vp/Vs velocity ratio behavior. Two seismic events, A and B, are labeled on Figure 5.1-5 to Figure 5.1-7. Seismic event A can be seen on all three P-P, SV-P, and P-SV images but seismic event B can be seen on only two P-P and SV-P images. Because seismic event A is just below the Ellenburger, it seems that the upper half portion of each image is matched relatively well. Regardless of the theoretical similarity between SV-P and P-SV images, seismic event B cannot be seen on the P-SV image. It seems that this discrepancy is caused by the poor quality of P-SV data. DeAngelo et al. (2003) pointed out that P-wave and C-wave data can be matched by finding characteristic features (called nail points) in both images. Vice versa, finding characteristic features in matched images can be evidence of good data quality and matching accuracy. Basically, my observation of multicomponent seismic images is that the P-P image and the SV-P/P-SV image may or may not be similar in terms of reflection wave shape and very few seismic events can be matched from reflection wave shape patterns. To make further discussion about multicomponent seismic image comparisons, 10 features labeled C1~C6 and D1~D4 are shown in each image.

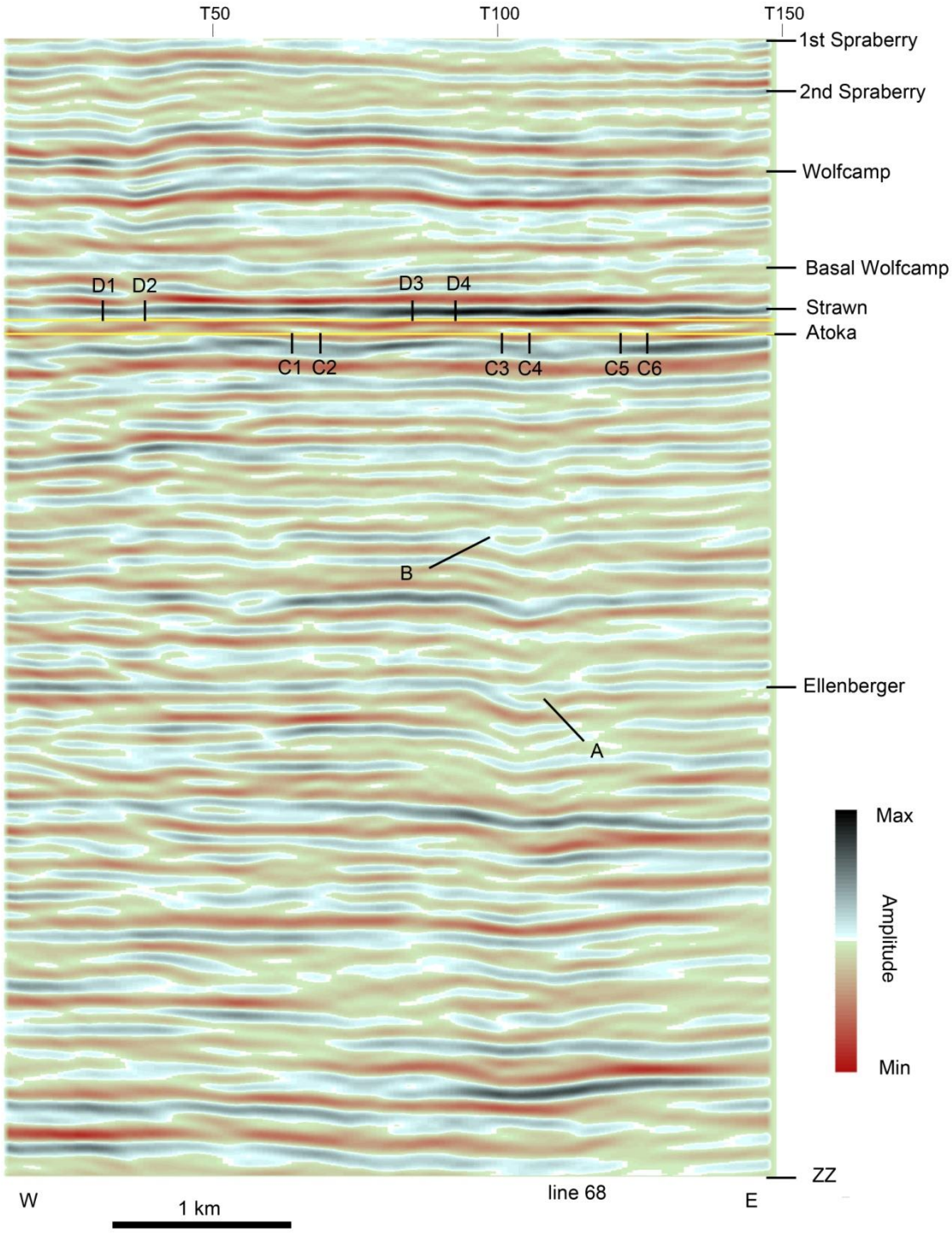

Figure 5.1-5: P-P crossline profile 68 in geologic time section view. Geologic times corresponding to formation tops are shown on the right side. ZZ is the deepest matching horizon.

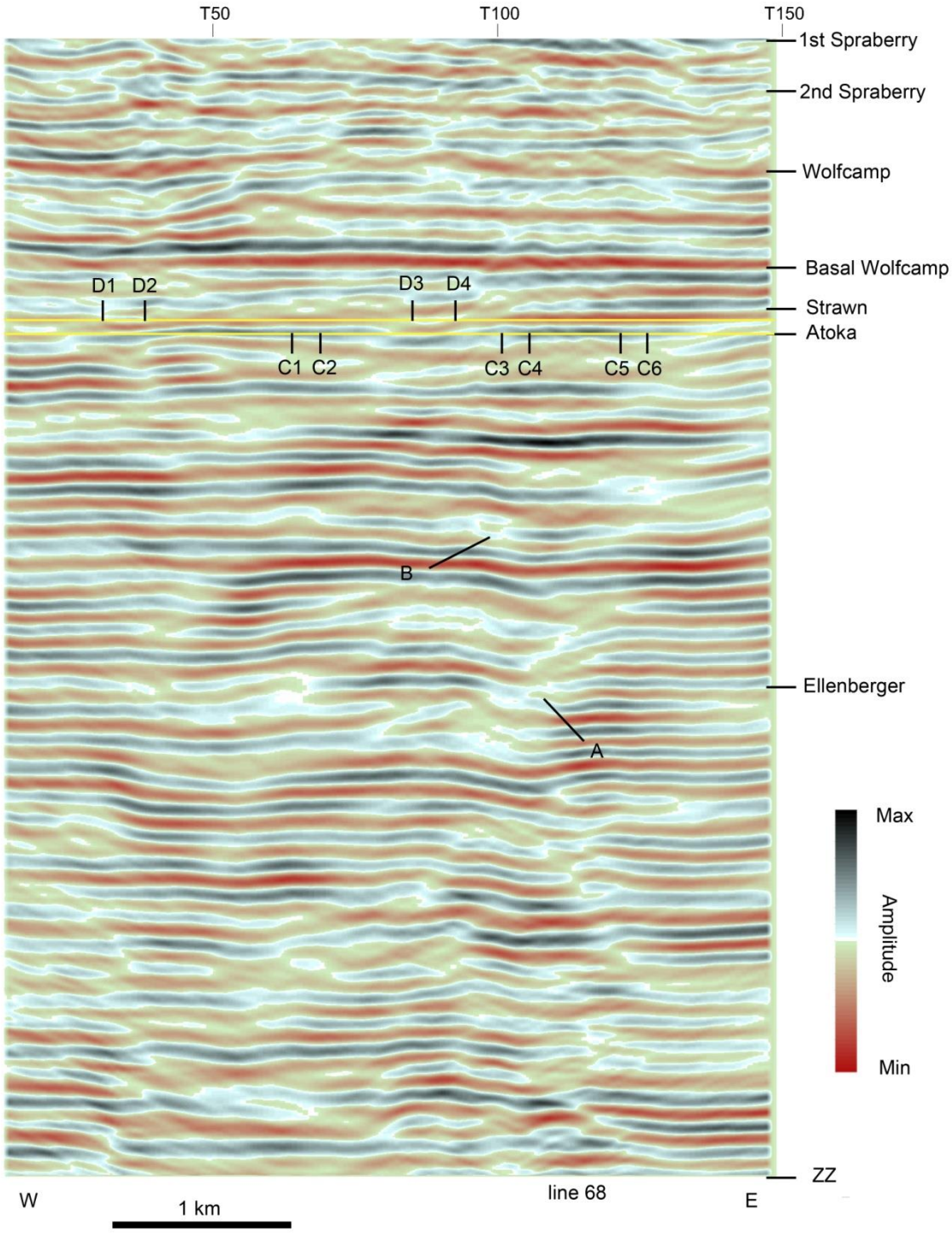

Figure 5.1-6: SV-P crossline profile 68 in geologic time section view. Geologic times corresponding to formation tops are shown on the right side. ZZ is the deepest matching horizon.

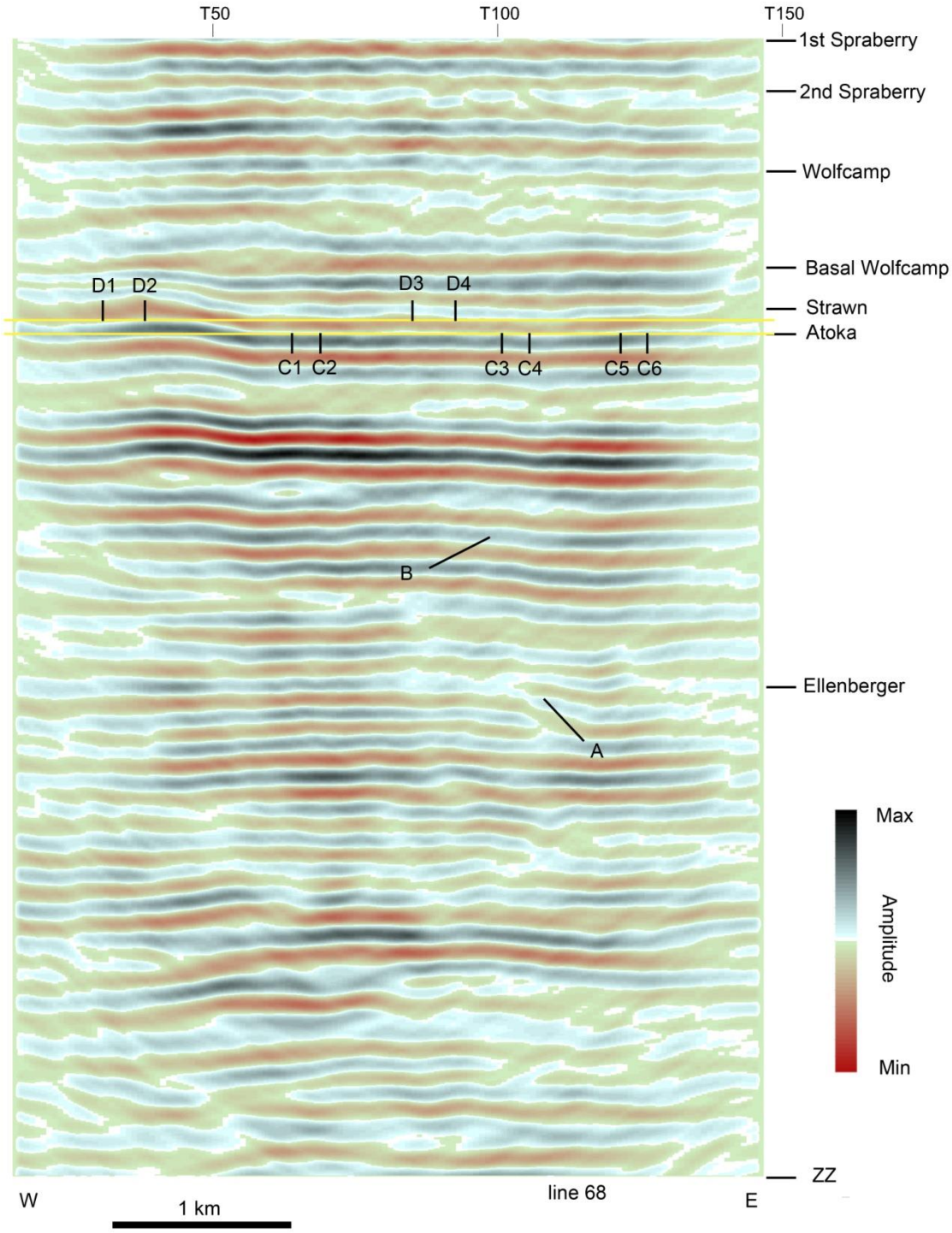

Figure 5.1-7: P-SV crossline profile 68 in geologic time section view. Geologic times corresponding to formation tops are shown on the right side. ZZ is the deepest matching horizon.

5.2 IMAGE COMPARISONS

RMS amplitude maps spanning the interval between the Strawn and the Atoka, and semblance map views for geologic time slices passing through C1-C6 and D1-D4 of Figure 5.1-5 to Figure 5.1-7 are shown in Figure 5.2-1 through Figure 5.2-6. Comparing Figure 5.1-5, Figure 5.1-6, and Figure 5.1-7, characteristic features defined by C1-C2, C3-C4, and C5-C6 can be distinguished only on the P-P image (Figure 5.1-5). On the SV-P image (Figure 5.1-6) and the P-SV image (Figure 5.1-7), there is no amplitude or semblance anomaly. From corresponding RMS amplitude and semblance map views (Figure 5.2-1), these characteristic features seem to be parts of turbidite lobes. Similarly, turbidite lobe-like features passing through D1-D2 and D3-D4 can be seen on the SV-P image (Figure 5.1-6) but not on the P-P image (Figure 5.1-5). RMS amplitude and semblance map view of the SV-P image (Figure 5.2-4) shows strong anomalies.

From the theoretical similarity of SV-P and P-SV images, more matching seismic events are expected between SV-P image and P-SV images than between P-P image and SV-P images; however, the poor data quality of the P-SV image may make this comparison difficult. On the geologic time surfaces passing through C1-C6, and on the stratal slices passing through D1-D4, the P-SV image shows only continuous amplitudes and in the semblance map, the P-SV image shows totally different patterns from the SV-P image. On the RMS amplitude map, there is no correlation between SV-P and P-SV images.

Comparing Figure 5.1-5, Figure 5.1-6, and Figure 5.1-7, even though there are apparent nail points (A and B) in the P-P, SV-P, and P-SV images, most of imaged areas show different image patterns and geologic events shown on one image are not seen on

the other image. Thus, it can be said that a SV-P or P-SV image can give as much information as a P-P image and that information from SV-P and P-SV images display additional information not included in the corresponding P-P image.

(a)

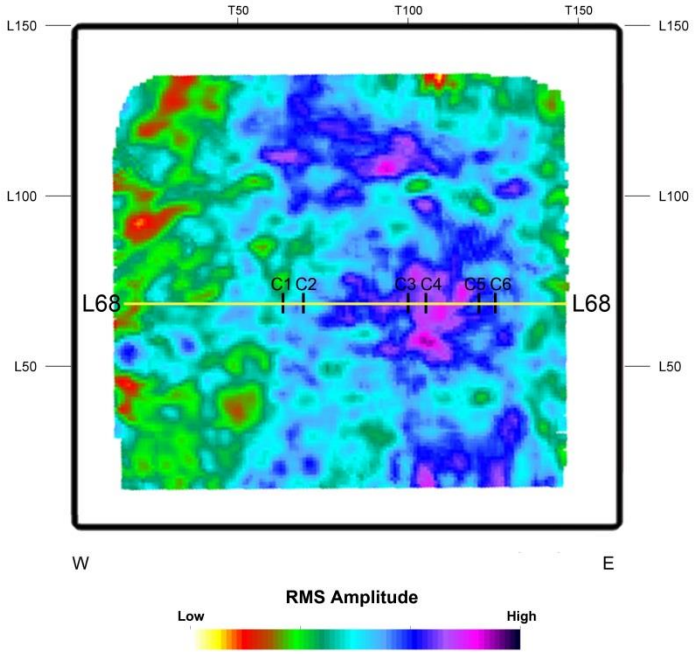

(b)

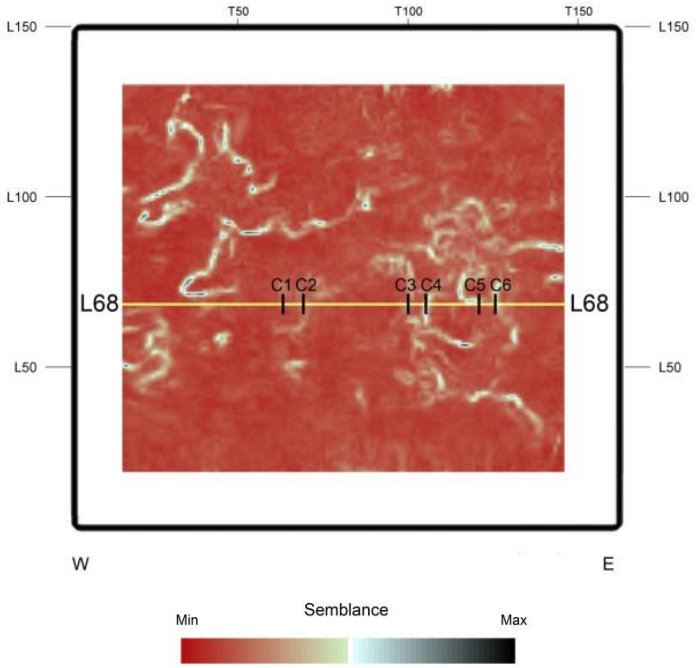

Figure 5.2-1: (a) RMS amplitude map view of P-P image for the interval between the Strawn and the Atoka, (b) Semblance map view of a P-P stratal slice passing through features C1-C6.

(a)

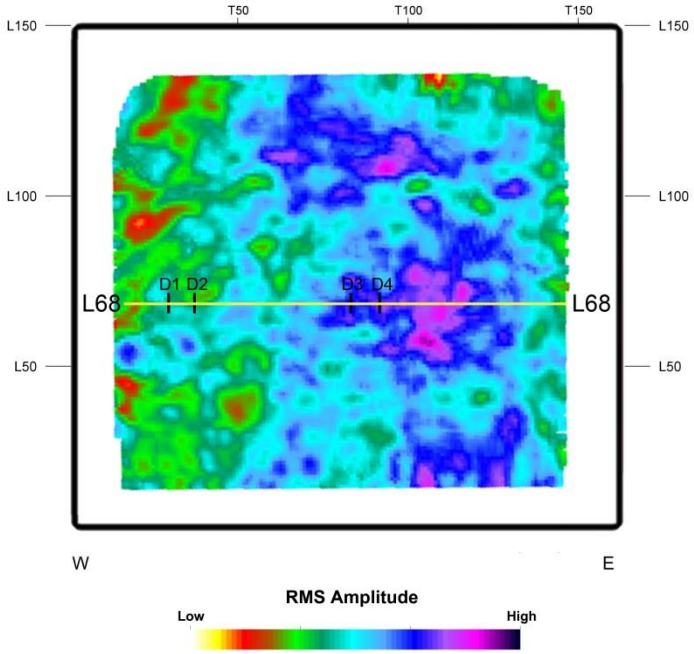

(b)

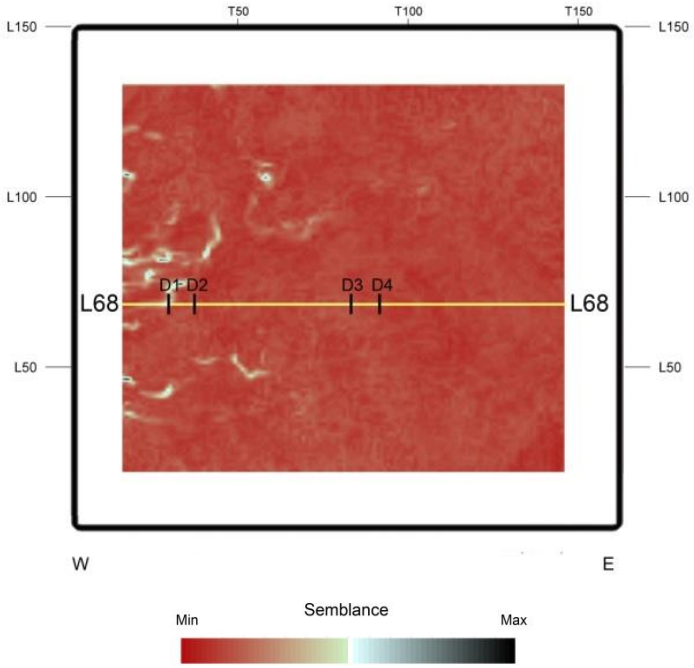

Figure 5.2-2: (a) RMS amplitude map view of P-P image for the interval between the Strawn and the Atoka, (a) Semblance map view of a P-P stratal slice passing through features D1-D4.

(a)

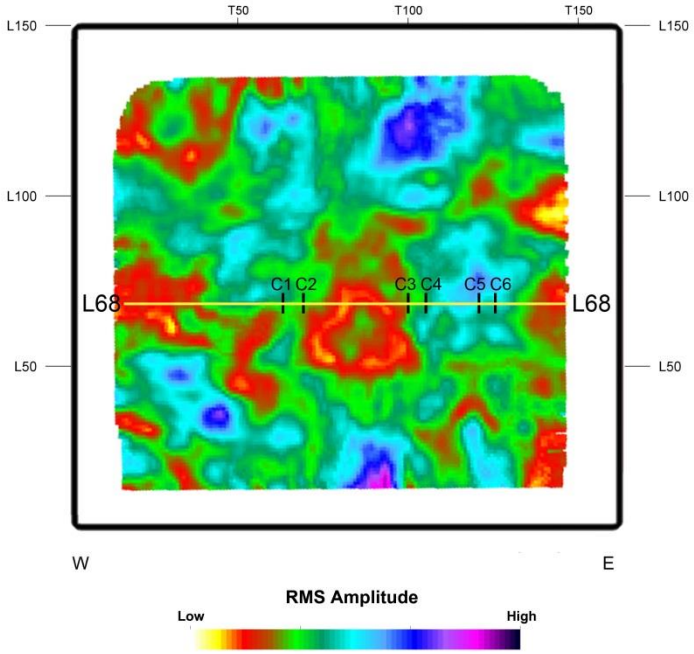

(b)

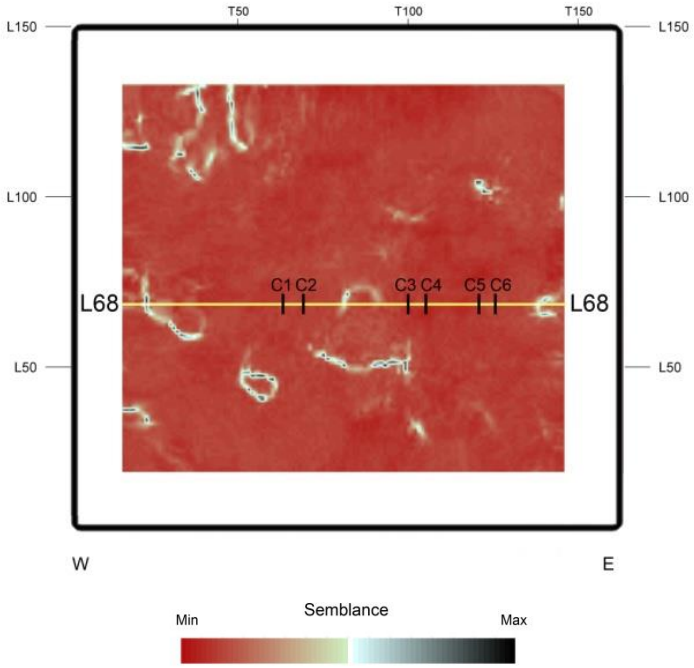

Figure 5.2-3: (a) RMS amplitude map view of SV-P image for the interval between the Strawn and the Atoka, (b) Semblance map view of a SV-P stratal slice passing through features C1-C6.

(a)

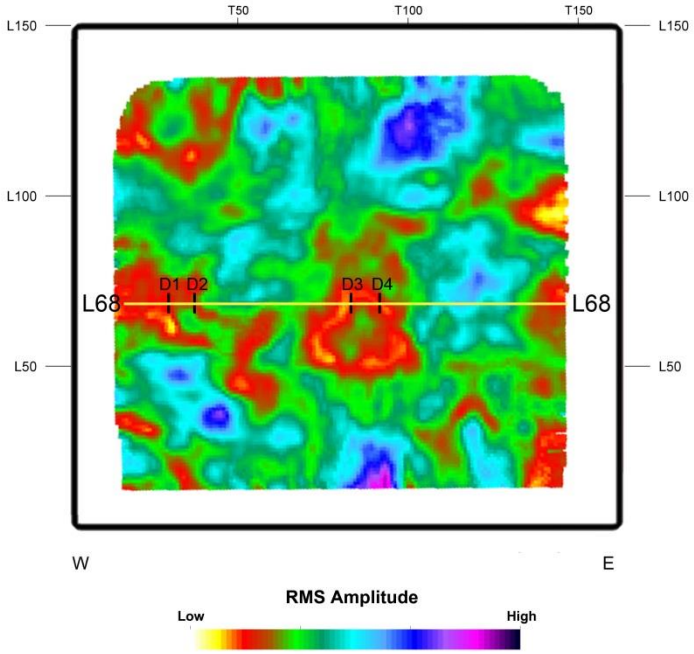

(b)

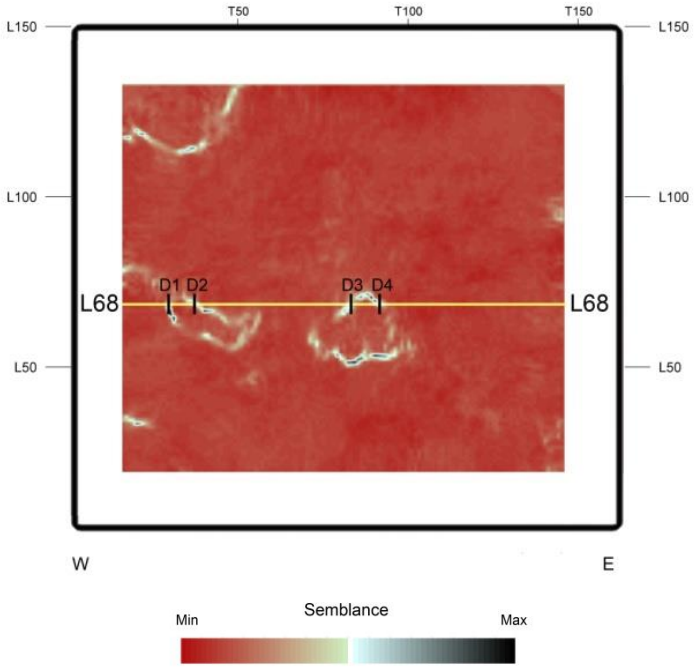

Figure 5.2-4: (a) RMS amplitude map view of SV-P image for the interval between the Strawn and the Atoka, (b) Semblance map view of a SV-P stratal slice passing through features D1-D4.

(a)

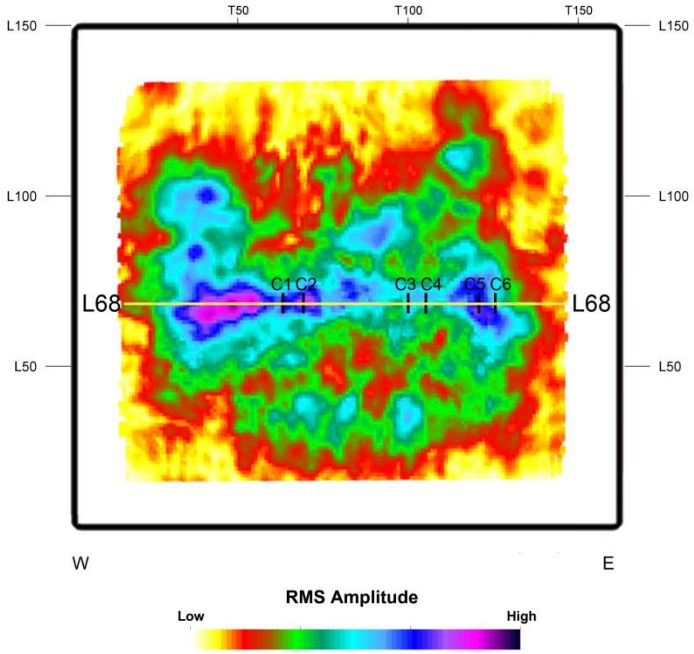

(b)

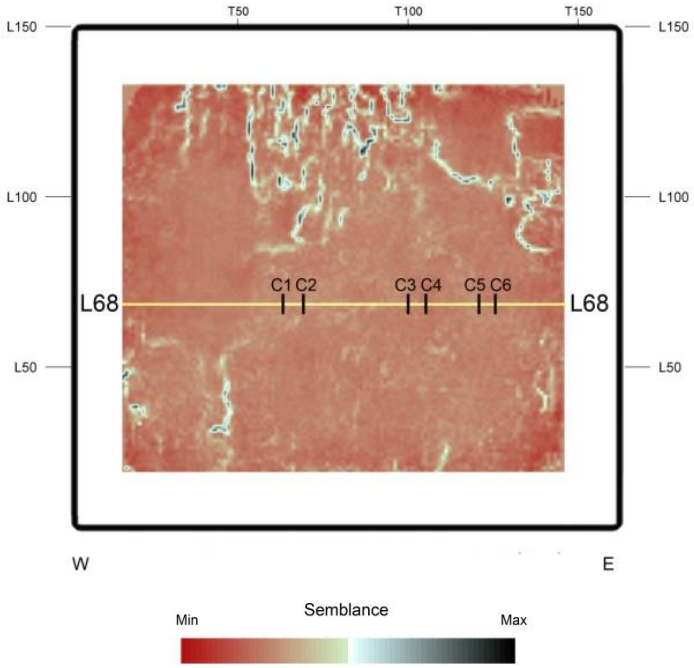

Figure 5.2-5: (a) RMS amplitude map view of P-SV image for the interval between the Strawn and the Atoka, (b) Semblance map view of a P-SV stratal slice passing through features C1-C6.

(a)

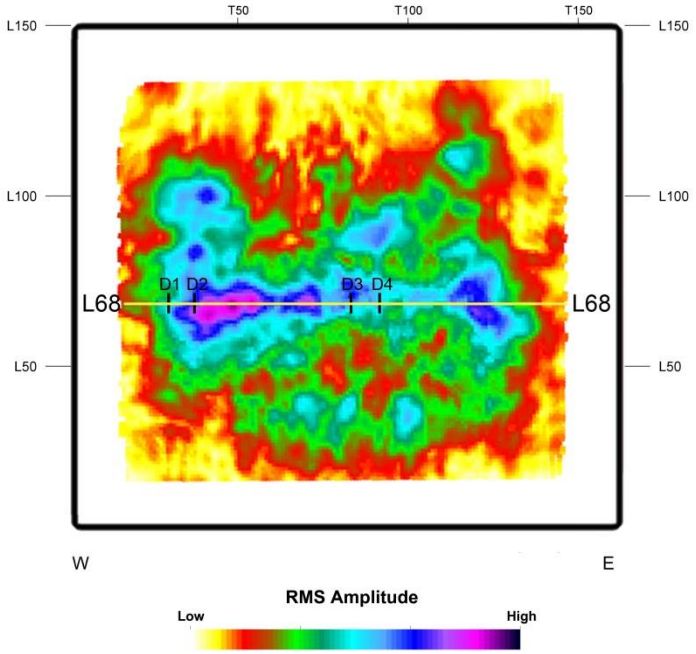

(b)

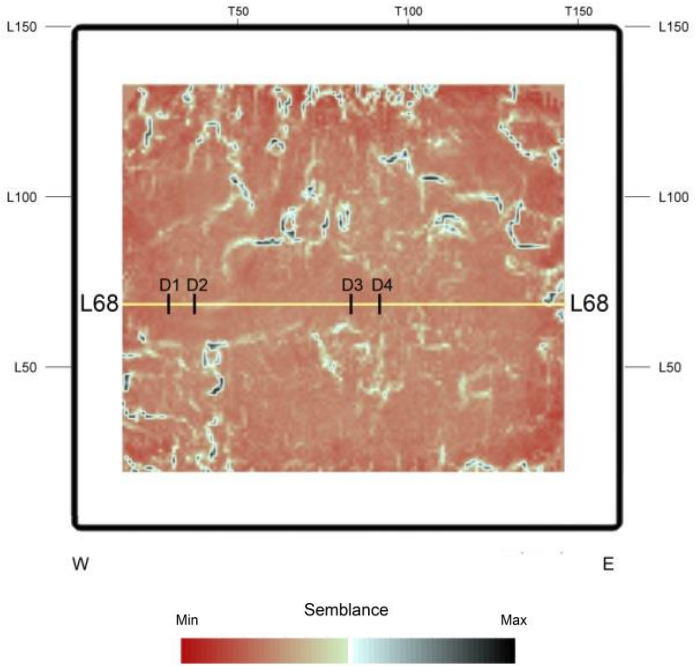

Figure 5.2-6: (a) RMS amplitude map view of P-SV image for the interval between the Strawn and the Atoka, (b) Semblance map view of P-SV stratal slice passing through features D1-D4.

5.3 THEORETICAL CONSIDERATIONS

Figure 5.3-1 and Figure 5.3-2 show relationships between reflectivity of P-P, SV-P, P-SV, and SV-SV modes. Assuming the reflection geometry of Figure 3.2-1 for the P-P mode, Figure 3.2-2 for the SV-SV mode, and Figure 3.2-5 for SV-P and P-SV modes, reflection coefficients for FEE AL 910 well data of 0 to 30 degrees of incident-angle are calculated with 1 degree increments using the Zoeppritz equation (Equation 3.3-a) and summations of them are cross-plotted to mimic seismic data stacking. Figure 5.3-1 shows scattered, but mostly negative, correlations between P-P reflectivity and SV-P/P-SV reflectivity. It can be said that P-P and SV-P/P-SV images have mostly opposite polarity because their reflection coefficients have negative correlation. Also, there are many data points where P-P reflectivity is almost zero but SV-P/P-SV reflectivity is not. Vice versa, SV-P/P-SV reflectivity can be zero but P-P reflectivity is not zero. In this sense, when seismic reflectivities of interfaces are superimposed, mostly P-P and SV-P/P-SV images do not have similar patterns. Also, some seismic events in a P-P image may not be seen on SV-P or P-SV images. In the same way, SV-P or P-SV images can show seismic events that are hidden in a P-P image.

Figure 5.3-2 shows the relationship between P-SV and SV-P reflectivity, and between P-P and SV-SV reflectivity. P-P reflectivity and SV-SV reflectivity also have mostly negative but scattered correlation; however, P-SV reflectivity and SV-P reflectivity have very strong positive correlation. In this sense, even though there are differences such as raypath and wave mode, SV-P and P-SV images should be very similar. As far as image matching is concerned, based on the shape patterns of reflections, P-P images should not match SV-P, P-SV, or SV-SV images but SV-P images should match P-SV images.

(a)

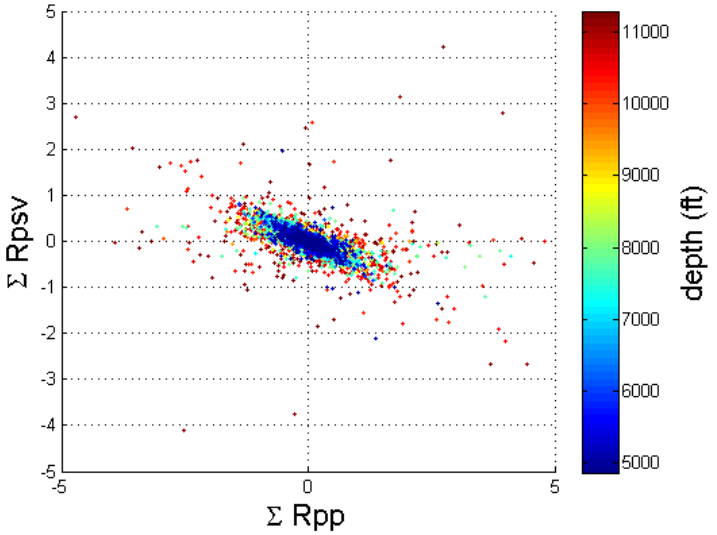

(b)

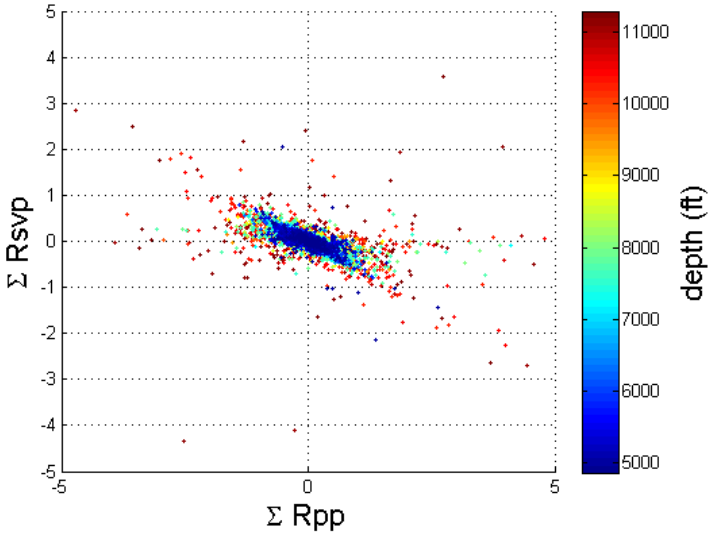

Figure 5.3-1: Cross-plot of (a) P-P reflectivity and P-SV reflectivity, and (b) P-P reflectivity and SV-P reflectivity. Values are summation of reflection coefficients calculated from 0 to 30 degrees incident angle.

(a)

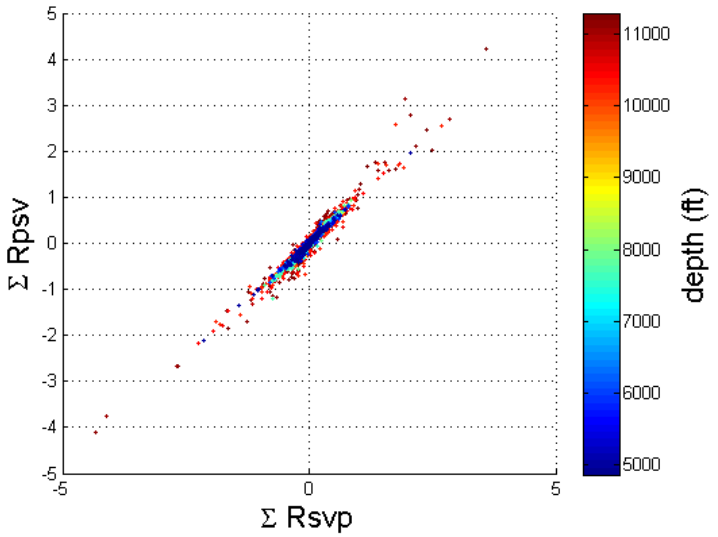

(b)

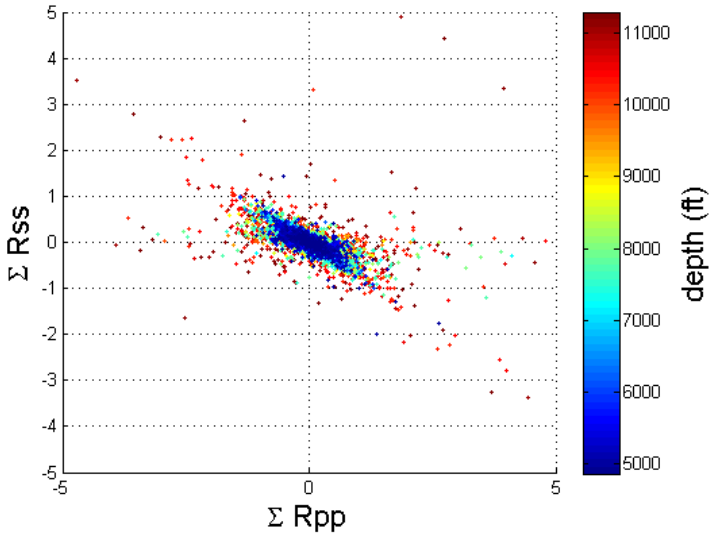

Figure 5.3-2: Cross-plot of (a) SV-P reflectivity and P-SV reflectivity, and (b) P-P reflectivity and SV-SV reflectivity. Values are summation of reflection coefficients calculated from 0 to 30 degrees incident angle.

Chapter 6: Conclusions and Possible Future Work

6.1 MULTICOMPONENT SEISMIC-TO-WELL CORRELATION

Conclusion 1: The seismic-to-well correlation method using synthetic seismograms created from well log data is valid not only for P-P image depth registration but also SV-P image depth registration. Even though the P-SV image does not match well data results and there are no SV-SV data available for my study, this method can be applied to all modes of multicomponent seismic image considering the theoretical similarities between SV-P and P-SV modes, and between P-P and SV-SV modes. Practically, SV-P depth registration can be done with a P-SV depth registration module of commercial software, and SV-SV depth registration with a P-P depth registration module by replacing P-wave velocities with S-wave velocities.

Conclusion 2: When a synthetic seismogram is created for depth registration purposes, the incident-angle does not affect the depth registration result much. Synthetic seismogram studies using the logs from the FEE Al 910 well show that synthetic seismograms do not change much with varying incident-angle. This observation applies not only for the P-P mode but also for all other modes. However, to generalize, synthetic modelling for other wells should be done if sonic and density logs are available.

Conclusion 3: When a synthetic seismogram is created for depth registration purposes, I observed only small difference in depth registration results between a zero-phase wavelet assumption and a minimum-phase wavelet assumption.

Conclusion 4: The DTW technique is useful for matching synthetic and real data when the quality of seismic data is good. Despite many advantages of DTW technique, it can generate unexpected matching results, and strict supervision is required for bad quality data.

6.2 MULTICOMPONENT SEISMIC IMAGE COMPARISONS

Conclusion 1: According to regional lithology, a P-P image and SV-P/P-SV images may or may not show same geologic event because of their different responses to lithology. One geologic event may be seen both in P-P and SV-P/P-SV images. On the other hand, a reflection may be seen only in a P-P image or in SV-P/P-SV images. Thus, P-P images and SV-P/P-SV images are equally valuable.

Conclusion 2: SV-P image and PS-V images are expected to be similar because of their theoretical similarity in terms of reflectivity; however, P-P image does not have similar reflection patterns to SV-P, P-SV, and SV-SV images. Accordingly, P-P and other mode images are less expected to match based on the similarity of their reflection patterns than SV-P and P-SV images.

6.3 POSSIBLE FUTURE WORK

It seems that depth registration results can be improved using pre-stack seismic data because information about which range of incident-angle data is stacked can be used to make more reliable synthetic seismograms.

It is a big challenge to estimate the phase spectrum of real wavelets. Once wavelet phase is properly defined, phase spectrum information seems to increase depth registration accuracy dramatically.

When data have proper quality, it is expected that SV-P and P-SV images will be very similar and that they can be matched by comparing both images directly. Comparing matching results from seismic-to-well correlation methods and direct-image comparisons for good quality data acquired using buried geophones could be a good expansion of this study.

References

Aki, K., and P. G. Richards, 1990, Quantitative seismology – theory and methods: W. H. Freeman and Co.

Aki, K., and P. G. Richards, 2002, Quantitative seismology, 2nd ed.: University Science Books.

Angeleri, G., 1983, A statistical approach to the extraction of the seismic propagating wavelet: Geophysical Prospecting, **31**, 726-747.

Ball, M. M., 1995, Permian Basin Province (044), National Assessment of United States Oil and Gas Resources, U. S. Geological Survey, Circular 1118.

Berndt, D. J., and J. Clifford, 1994, Using dynamic time warping to find patterns in time series: KDD Workshop, 359–370.

Chopra, S., and K. J. Marfurt, 2007, Seismic attributes for prospect identification and reservoir characterization: Geophysical Developments No. 11, Society of Exploration Geophysicists, Tulsa, OK.

DeAngelo, M., M. Backus, B. A. Hardage, P. Murray, and S. Knapp, 2003, Depth registration of P-wave and C-wave seismic data for shallow marine sediment characterization, Gulf of Mexico: The Leading Edge, **22**, 96-105.

Dey, A. K., 1999, An analysis of seismic wavelet estimation: M.S. thesis, University of Calgary.

Domenico, S. N., 1984, Rock lithology and porosity determination from shear and compressional wave velocity: Geophysics, **49**, 1188-1195.

Fomel, S., M. Backus, M. DeAngelo, P. Murray, and B. Hardage, 2003, Multicomponent seismic data registration for subsurface characterization in the shallow Gulf of Mexico: OTC, Expanded Abstracts, 15117.

Fomel, S., M. Backus, K. Fouad, B. Hardage, and G. Winters, 2005, A multistep approach to multicomponent seismic image registration with application to a west Texas carbonate reservoir study: 75th Annual International Meeting, SEG, Expanded Abstracts, 1018–1021.

Hamlin, S., and R. Baumgardner, 2012, Wolfberry (Wolfcampian-Leonardian) deep-water depositional systems in the Midland Basin – stratigraphy, lithofacies, reservoirs, and source rocks: Report of Investigation No. 227, Bureau of Economic Geology.

Hardage, B. A., M. V. DeAngelo, P.E. Murray, and D. Sava, 2011, Multicomponent seismic technology: Geophysical Reference Series No. 18, Society of Exploration Geophysicists, Tulsa, OK.

Hardage, B. A., D. Sava, and D. Wagner, 2014, SV-P: An ignored seismic mode that has great value for interpreters, Interpretation, **2**, SE17–SE27.

Hardage, B. A., M. V. DeAngelo, and D. Sava, 2015, Case history: SV-P imaging of wolfberry unconventional reservoirs: A report to the sponsors of the exploration geophysics laboratory, Bureau of Economic Geology.

Loucks, R. G., 2006, Review of the Lower Ordovician Ellenburger Group of the Permian Basin, West Texas: The University of Texas at Austin, Bureau of Economic Geology.

Kerans, C., 1990, Depositional systems and karst geology of the Ellenburger Group (Lower Ordovician), subsurface West Texas: The University of Texas at Austin, Report of Investigations No. 193, Bureau of Economic Geology.

Krohn, C. E., 1984, Geophone ground coupling: Geophysics,**49**, 722–731.

Pardus, Y. C., Conner J., Schuler N. R., and Tatham R. H., 1990, Vp/Vs and lithology in carbonate rocks: a case study in the Scipio Trend in Southern Michigan: 60th Annual International Meeting, Society of Exploration Geophysicists, Expanded abstracts, 169-172.

Robinson, E. A., 1967, Predictive deconvolution of time series with application to seismic exploration: Geophysics, **32**, 418-484.

Rüger, A., 2002, Reflection coefficients and azimuthal AVO analysis in anisotropic media: Geophysical Monograph Series No. 10, Society of Exploration Geophysicists, Tulsa, OK.

Stone, D. G., 1984, Wavelet estimation: Proc. IEEE, **72,** no. 10, 1394-1402.

Tatham, R. H, M. D. McCormack, E. B. Neitzel, and D. F. Winterstein, 1991, Chapter 7: Multicomponent interpretation, Case Histories, in Multicomponent seismology in petroleum exploration: Society of Exploration Geophysicists, 187–244.

Vail, P. R., R. G. Todd, and J. B. Sangree, 1977, Seismic stratigraphy and global changes of sea level, Part 5: Chronostratigraphic significance of seismic reflections, in C. E. Payton ed. Seismic Stratigraphy: AAPG Memoir 26, 99–116.

Zeng, H., 2010, Stratal slicing: Benefits and challenges: The Leading Edge, **29**, 1040-1047.

Vita

JUNG KYU KIM received a B.S. (Bachelor of Science) degree in Civil, Urban and Geosystem Engineering from Seoul National University in South Korea and has worked as a civil engineer in a LNG receiving terminal construction field and as an economist for the exploration project. He started his graduate study in Dr. Bob Hardage's research group at The University of Texas at Austin on August 2013 and received an M.S. degree in Geological Sciences (Exploration Geophysics) in May 2015. He is now working in Korea Gas Corporation, 120 Cheomdan-ro, Dong-gu, Daegu, South Korea (Republic of Korea), 701-300. His email address is jungkyu.kim@utexas.edu.

This thesis was typed by JUNG KYU KIM.